

THESIS FOR THE DEGREE OF DOCTOR OF PHILOSOPHY IN THERMO AND  
FLUID DYNAMICS

Numerical Methods for Aeroacoustic Analysis of  
Turbomachines

DANIEL LINDBLAD

Department of Mechanics and Maritime Sciences  
Division of Fluid Dynamics  
CHALMERS UNIVERSITY OF TECHNOLOGY  
Göteborg, Sweden 2020

Numerical Methods for Aeroacoustic Analysis of Turbomachines  
DANIEL LINDBLAD  
ISBN 978-91-7905-336-9

© DANIEL LINDBLAD, 2020

Doktorsavhandlingar vid Chalmers tekniska högskola  
Ny serie nr. 4803  
ISSN 0346-718X  
Department of Mechanics and Maritime Sciences  
Division of Fluid Dynamics  
Chalmers University of Technology  
SE-412 96 Göteborg  
Sweden  
Telephone: +46 (0)31-772 1000

Chalmers Reproservice  
Göteborg, Sweden 2020

Numerical Methods for Aeroacoustic Analysis of Turbomachines

DANIEL LINDBLAD

Department of Mechanics and Maritime Sciences

Division of Fluid Dynamics

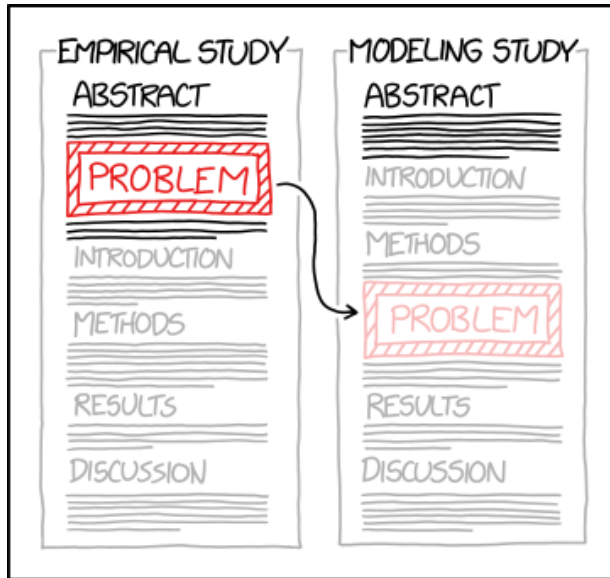
Chalmers University of Technology

## ABSTRACT

Numerical simulations are important tools for developing new aircraft that can meet future needs. When numerical simulations are used to compute aircraft noise, a two-step procedure is often employed. In the first step, the noise sources are determined using, e.g., computational fluid dynamics. In the second step, noise propagation between the sources and the observers is then computed, often by solving an acoustic analogy. In this thesis, a range of numerical methods that are useful when turbomachinery tonal noise is computed based on such a two-step procedure are considered. For the first step, the time-domain Harmonic Balance method proposed by Hall et al. is used. To improve the accuracy of this method, the impact of time sampling on aliasing is investigated for both the single frequency and the multiple frequency problem. A new oversampling strategy for the multiple frequency problem is also developed for this purpose. Another challenge associated with the Harmonic Balance method is numerical instabilities. This problem is investigated using a von Neumann stability analysis. Based on knowledge gained from this analysis, a novel preconditioner that stabilizes an explicit Harmonic Balance solver is then developed. To minimize reflections of waves against boundaries of the computational domain, a generic formulation of the exact, nonlocal, nonreflecting boundary condition introduced by Giles is also derived and implemented to work with the Harmonic Balance method. For the second step, the convective Ffowcs Williams - Hawkings equation for permeable surfaces proposed by Najafi-Yazidi et al. is used. A detailed derivation of this equation is first presented. The solution to this equation for the case when the surface is stationary relative to the observer is then derived. Finally, a tool for computing duct modes based on a normal mode analysis of the linearized Euler equations is presented. In summary, the work reported in this thesis provides a detailed analysis of the aforementioned methods, that should be valuable for people who are interested in adopting them. It also provides some improvements, which can help to further improve the results obtained with these methods.

Keywords: Harmonic Balance, Aliasing, Time Sampling, Stability Analysis, Nonreflecting Boundary Conditions, Duct Modes, Acoustic Analogy, Ffowcs Williams - Hawkings, Turbomachinery, Tonal Noise





A MATHEMATICAL MODEL IS A POWERFUL  
TOOL FOR TAKING HARD PROBLEMS AND  
MOVING THEM TO THE METHODS SECTION.

- Randall Munroe, XKCD Comic 2323



## ACKNOWLEDGEMENTS

I have faced both technical and emotional challenges during my journey towards a Ph.D. These challenges would have been much harder to overcome without all the amazing people that I have had the privilege to work with over the years.

I would like to start by thanking my supervisor Niklas Andersson, for giving me the chance to pursue a Ph.D., for helping me out when things got tough, and for being such a great friend. Next, I would like to thank all my colleagues at the department of Mechanics and Maritime Sciences, for making work such a fun place to be. Special thanks to Gonzalo Montero Villar and Elias Siggeirsson, for all the interesting discussions we have had and for making the conference trips so much fun, to Alexandre Capitaio Patrao, for sharing your deep knowledge on propellers with me, and to Guglielmo Minelli, for all the competence and fun you brought into our office.

I would like to thank Nathan Wukie at the Airforce Research Laboratory, for all the interesting discussions on nonreflecting boundary conditions we have had. I would also like to thank the people at the German Aerospace Center (DLR) in Cologne for making me feel right at home in your group and for inviting me to celebrate the Carnival with you. Special thanks Christian Frey, Graham Ashcroft, and Laura Junge, for the inspiring and fruitful collaboration we had.

I would finally like to thank my family for the love and support that you have given me over the years, and Darya, for all the joy you have brought into my life.

This work was financially supported by the European Commission within the Horizon 2020 Programme (2014-2020) through the ULTIMATE<sup>1</sup> Project, Grant Agreement No. 633436, and by the Swedish Energy Agency through the HIGH2<sup>2</sup> Project, Grant Agreement No. 2017-00116. I would like to express my gratitude to all partners within the ULTIMATE and the HIGH2 projects who have contributed to the work reported in this thesis. The Swedish National Infrastructure for Computing (SNIC) is also gratefully acknowledged for providing computer resources at the National Supercomputing Center (NSC) and Chalmers Centre for Computational Science and Engineering (C<sup>3</sup>SE).

---

<sup>1</sup>Ultra Low emission Technology Innovations for Mid-century Aircraft Turbine Engines

<sup>2</sup>Heat load distribution In hot parts of industrial Gas turbines burning HYDROGEN rich fuel





# NOMENCLATURE

## Greek Letters

$\gamma$	Ratio of specific heats	
$\delta_{ij}$	Kronecker delta	
$\delta(x)$	Dirac delta function	
$\varepsilon$	Damping parameter used to regularize nonreflecting boundary condition	$\text{s}^{-1}$
$\theta$	Circumferential coordinate	rad
$\kappa$	Condition number of $E_{\Lambda}^{-1}(\mathbf{t})$	
$\lambda$	Eigenvalue to $\bar{A}$	$\text{m s}^{-1}$
$\Lambda$	Matrix containing eigenvalues to $\bar{A}$ along its diagonal	$\text{m s}^{-1}$
$\Lambda$	Set of frequencies included in the Fourier series expansion	$\text{rad s}^{-1}$
$\Lambda_R$	Set of frequencies present in the signal $R(\mathbf{q}^*)$	$\text{rad s}^{-1}$
$\Lambda''$	Union of the two sets $\Lambda$ and $\Lambda_R$	$\text{rad s}^{-1}$
$\rho$	Density	$\text{kg m}^{-3}$
$\sigma$	Courant–Friedrichs–Lewy number	
$\sigma$	Under relaxation factor	
$\sigma_{ij}$	Viscous stress tensor	$\text{kg m}^{-1} \text{s}^{-2}$
$\tau$	Pseudo-time	s
$\Delta\tau$	Pseudo-time step	s
$\tau_{\text{ret}}$	Retarded time/emission time	s
$\phi$	Normalized spatial wavenumber	rad
$\phi(\mathbf{x})$	Test function	
$\omega_n$	Angular frequency	$\text{rad s}^{-1}$
$\Omega$	Rotational speed of blade row	$\text{rad s}^{-1}$
$\Omega_{\Lambda}$	Matrix containing the frequencies in $\Lambda$ , multiplied by $i$ , along its diagonal	$\text{rad s}^{-1}$

## Roman Letters

$A$	Axial flux Jacobian	
$B$	Radial flux Jacobian	
$C$	Circumferential flux Jacobian	
$c$	Speed of sound	$\text{m s}^{-1}$
$\mathbf{D}$	Time spectral derivative matrix	$\text{s}^{-1}$
$E_{\Lambda}^{-1}(\mathbf{t})$	Inverse discrete Fourier transform matrix for frequencies in $\Lambda$ and time instances in $\mathbf{t}$	

$E_\Lambda(\mathbf{t})$	Discrete Fourier transform matrix for frequencies in $\Lambda$ and time instances in $\mathbf{t}$	
$F_j$	Vector containing total flux of conserved variables	
$G(\mathbf{x}, t)$	Green's function to convective wave operator	$\text{s}^2 \text{m}^{-3}$
$H(x)$	Heaviside step function	
$k_j$	Wavenumber	$\text{rad m}^{-1}$
$\tilde{L}_i$	Source term in generalized momentum equation	$\text{kg m}^{-2} \text{s}^{-2}$
$L_i$	Source term in the convective Ffowcs Williams - Hawkings equation	$\text{kg m}^{-2} \text{s}^{-2}$
$M$	Mach number	
$M$	Number of time instances in $\mathbf{t}$	
$n_i$	Cartesian component of surface normal vector	
$p$	Static pressure	$\text{kg m}^{-1} \text{s}^{-2}$
$p_{ij}$	Compressive stress tensor	$\text{kg m}^{-1} \text{s}^{-2}$
$Q$	Source term in generalized continuity equation	$\text{kg m}^{-3} \text{s}^{-1}$
$q$	Vector containing conserved or primitive variables	
$\mathbf{q}$	Vector containing cell-averaged conserved variables	
$\hat{\mathbf{q}}_\Lambda$	Vector containing Fourier transform of $\mathbf{q}$ for frequencies in $\Lambda$	
$\mathbf{q}^*$	Vector containing values of $\mathbf{q}$ for all time instances in $\mathbf{t}$	
$r$	Radial coordinate	$\text{m}$
$R$	Vector containing discrete approximation of total flux of conserved variables	
$\hat{\mathbf{R}}_\Lambda$	Vector containing Fourier transform of $R$ for frequencies in $\Lambda$	
$T$	Time period	$\text{s}$
$t$	Time	$\text{s}$
$\mathbf{t}$	Vector containing time instances used for discrete Fourier transform	$\text{s}$
$T_{ij}$	Lighthill tensor	$\text{kg m}^{-1} \text{s}^{-2}$
$T^{-1}$	Matrix containing left eigenvectors to $(\omega \bar{A}^{-1} - k_z \bar{A}^{-1} \bar{C})$	
$t_j$	$j^{\text{th}}$ element in $\mathbf{t}$	$\text{s}$
$T$	Matrix containing right eigenvectors to $(\omega \bar{A}^{-1} - k_z \bar{A}^{-1} \bar{C})$	
$u_i$	Cartesian velocity component	$\text{m s}^{-1}$
$v_i$	Cartesian velocity component	$\text{m s}^{-1}$
$v_g$	Group velocity	$\text{m s}^{-1}$
$W^{-1}$	Matrix containing left eigenvectors to $\bar{A}$	
$W$	Matrix containing right eigenvectors to $\bar{A}$	

$\mathbf{x}$	Vector containing Cartesian components of position	m
$x_j$	$j^{\text{th}}$ element in $\mathbf{x}$	m
$x$	Axial coordinate	m
$\Delta x$	Size of cell	m

### Superscripts and Subscripts

$\square'$	Perturbation of quantity
$\square^{\text{nrbc}}$	Value of quantity that satisfies nonreflecting boundary condition
$\square^T$	Transpose
$\square_0$	Value of quantity in far field
$\square_c$	Value of quantity in current blade row
$\square_o$	Value of quantity in opposite blade row
$\square_e$	Value of quantity on east cell face
$\square_o$	Value of quantity at outer duct wall
$\square_w$	Value of quantity on west cell face
$\overline{\square}$	Time + azimuthal average of quantity



# THESIS

This thesis consists of an extended summary and the following appended papers:

- Paper A** D. Lindblad and N. Andersson. “Validating the Harmonic Balance Method for Turbomachinery Tonal Noise Predictions”. 55th AIAA Aerospace Sciences Meeting (Grapevine, TX, Jan. 9–13, 2017). AIAA Paper 2017-1171. DOI: 10.2514/6.2017-1171
- Paper B** D. Lindblad, G. Montero Villar, N. Andersson, A. Capitao Patrao, S.-k. Courty-Audren, and G. Napias. “Aeroacoustic Analysis of a Counter Rotating Open Rotor based on the Harmonic Balance Method”. 2018 AIAA Aerospace Sciences Meeting (Kissimmee, FL, Jan. 8–12, 2018). AIAA Paper 2018-1004. DOI: 10.2514/6.2018-1004
- Paper C** D. Lindblad, N. A. Wukie, G. Montero Villar, and N. Andersson. “A Nonreflecting Formulation for Turbomachinery Boundaries and Blade Row Interfaces”. 2019 AIAA Aerospace Sciences Meeting (San Diego, CA, Jan. 7–11, 2019). AIAA Paper 2019-1804. DOI: 10.2514/6.2019-1804
- Paper D** N. A. Wukie, D. Lindblad, and N. Andersson. “noisyduck: an open-source Python tool for computing eigenmode decompositions of duct flows”. 25<sup>th</sup> AIAA/CEAS Aeroacoustics Conference (Delft, The Netherlands, May 20–23, 2019). AIAA Paper 2019-2418. DOI: 10.2514/6.2019-2418
- Paper E** D. Lindblad and N. Andersson. Convergence Acceleration of the Harmonic Balance Method using a Time-Level Preconditioner. *AIAA Journal* (in press)
- Paper F** D. Lindblad, C. Frey, L. Junge, G. Ashcroft, and N. Andersson. Minimizing Aliasing in Multiple Frequency Harmonic Balance Computations. *Journal of Scientific Computing* (submitted)

Other publications related to this thesis:

- Paper I** D. Lindblad, G. Montero Villar, N. Andersson, and N. A. Wukie. “Implementation of a Quasi-Three-Dimensional Nonreflecting Blade Row Interface for Steady and Unsteady Analysis of Axial Turbomachines”. 2018 AIAA Aviation and Aeronautics Forum and Exposition (Atlanta, GA, June 25–29, 2018). AIAA Paper 2018-4187. DOI: 10.2514/6.2018-4187
- Paper II** G. Montero Villar, D. Lindblad, and N. Andersson. “Multi-Objective Optimization of an Counter Rotating Open Rotor using Evolutionary Algorithms”. 2018 AIAA Aviation and Aeronautics Forum and Exposition (Atlanta, GA, June 25–29, 2018). AIAA Paper 2018-2929. DOI: 10.2514/6.2018-2929

- Paper III** A. Capitaó Patrao, D. Lindblad, A. Lundbladh, and T. Grönstedt. “Aero-dynamic and aeroacoustic comparison of optimized high-speed propeller blades”. 2018 AIAA Joint Propulsion Conference (Cincinnati, OH, July 9–11, 2018). AIAA Paper 2018-4658. DOI: 10.2514/6.2018-4658
- Paper IV** N. A. Wukie, P. D. Orkwis, D. Lindblad, and N. Andersson. “Nonreflecting boundary conditions for the Euler equations in a discontinuous Galerkin discretization”. 2019 AIAA Aerospace Sciences Meeting (San Diego, CA, Jan. 7–11, 2019). AIAA Paper 2019-2172. DOI: 10.2514/6.2019-2172
- Paper V** G. Montero Villar, D. Lindblad, and N. Andersson. “Effect of Airfoil Parametrization on the Optimization of Counter Rotating Open Rotors”. 2019 AIAA Aerospace Sciences Meeting (San Diego, CA, Jan. 7–11, 2019). AIAA Paper 2019-0698. DOI: 10.2514/6.2019-0698
- Paper VI** D. Lindblad and N. Andersson. “Convergence Acceleration of the Harmonic Balance Method using a Time-Level Preconditioner”. 2020 AIAA Aerospace Sciences Meeting (Orlando, FL, Jan. 6–10, 2020). AIAA Paper 2020-0563. DOI: 10.2514/6.2020-0563

# CONTENTS

<b>Abstract</b>	<b>i</b>
<b>Acknowledgements</b>	<b>v</b>
<b>Nomenclature</b>	<b>vii</b>
<b>Thesis</b>	<b>xi</b>
<b>Contents</b>	<b>xiii</b>

## I   Extended Summary 1

### 1   Introduction 1

1.1   Source Prediction . . . . .	3
1.2   Noise Propagation . . . . .	7
1.3   Purpose and Limitations . . . . .	8

### 2   Modeling Unsteady Turbomachinery Flows: The Harmonic Balance Method 9

2.1   Error Sources . . . . .	12
2.1.1   Harmonic Truncation Error . . . . .	12
2.1.2   Alias Error . . . . .	12
2.2   Selection of Time Sampling . . . . .	13
2.2.1   Oversampling . . . . .	14
2.3   Stability Analysis . . . . .	15
2.4   Time Level Preconditioner . . . . .	23

### 3   Boundary Conditions and Duct Modes 26

3.1   Phase Shifted Periodic Boundary Condition . . . . .	28
3.2   Exact, Nonlocal, Nonreflecting Boundary Condition for a Single Fourier Mode . . . . .	31
3.2.1   Modal Decomposition . . . . .	31
3.2.2   Nonreflecting Condition . . . . .	35
3.2.3   Implementation Strategy . . . . .	37
3.3   Duct Modes . . . . .	43
3.3.1   Linearized Euler Equations . . . . .	43
3.3.2   Normal Mode Analysis . . . . .	44
3.3.3   Spatial Discretization . . . . .	44
3.3.4   Numerical Solution Strategy . . . . .	46
3.3.5   Classification of Modes . . . . .	46

<b>4</b>	<b>Generation and Propagation of Sound: The Acoustic Analogy</b>	<b>48</b>
4.1	Derivation of the Convective Ffowcs Williams - Hawkins Equation . . . .	51
4.2	Solution of the Convective Ffowcs Williams - Hawkins Equation . . . .	55
4.3	Implementation of Convective Ffowcs Williams - Hawkins Equation . . .	58
<b>5</b>	<b>Summary of Papers</b>	<b>61</b>
5.1	Paper A . . . . .	61
5.2	Paper B . . . . .	63
5.3	Paper C . . . . .	65
5.4	Paper D . . . . .	67
5.5	Paper E . . . . .	69
5.6	Paper F . . . . .	70
<b>6</b>	<b>Concluding Remarks</b>	<b>72</b>
	<b>References</b>	<b>76</b>
	<b>Appendices</b>	<b>84</b>
<b>A</b>	<b>Euler Equations in Cylindrical Coordinates</b>	<b>84</b>
A.1	Linearized Euler Equations for Quasi-Three Dimensional Flows . . . . .	87
A.2	Linearized Euler Equations for Planar Waves . . . . .	87
<b>B</b>	<b>Validation of Exact, Nonlocal, Nonreflecting Boundary Condition</b>	<b>89</b>
B.1	Two-Dimensional Wave Propagation . . . . .	89
B.2	Cascade-Gust Interaction Problem . . . . .	94
<b>C</b>	<b>Validation of noisyduck</b>	<b>101</b>
C.1	Uniform Axial Flow . . . . .	101
C.1.1	Analytical Solution . . . . .	101
C.1.2	Validation . . . . .	103
C.2	Free Vortex Swirl . . . . .	104
C.2.1	Constant Density . . . . .	104
C.2.2	Constant Entropy . . . . .	105
C.2.3	Validation . . . . .	106
<b>II</b>	<b>Appended Papers A–F</b>	<b>109</b>



# Part I

## Extended Summary

### 1 Introduction

Modern transportation systems have become an integral part of many people's lives, and continuously evolve to serve more and more of us in new and ingenious ways. Today, people from all around the world can meet, explore each other's cultures, and exchange goods within time frames that probably were not even dreamt about by our ancestors. This change in connectivity has partly been enabled by the air transportation sector, which has developed over the past half-century into a safe, efficient, and global transportation system. In the future, air travel is expected to continue growing at a rate of approximately 4 – 5% per year <sup>1</sup>. In response to this growth, the European Union has formulated its vision for a sustainable aviation future, called "Flightpath 2050" [20]. Among many things, this document states that the CO<sub>2</sub> emissions and perceived noise levels from aircraft in 2050 should be 75% and 65% lower than year 2000 levels, respectively. To meet these targets, the Advisory Council for Aviation Research and Innovation in Europe (ACARE) has developed the Strategic Research and Innovation Agenda (SRIA) [1]. The strategy in SRIA for meeting the noise targets of Flightpath 2050 is very much in line with the "Balanced Approach" for aircraft noise management set forward by ICAO [82]. ICAO is the United Nations organ that, among many things, develops guidelines for aircraft noise certification. In the Balanced Approach, reduction of noise at source (aircraft) is emphasized as an important strategy for minimizing the perceived noise levels of aircraft. Reducing the noise levels at source should, according to the SRIA targets, be achieved by both developing new, revolutionary noise reduction technologies, as well as improving (evolving) existing ones [1].

Computer-based numerical simulations are important for successfully developing new and improved noise reduction technologies. To be useful, numerical simulations need to be both accurate and computationally efficient. Although a lot of progress has been made with regard to these two metrics in the past decades, numerical simulations still do not always provide perfect predictions within acceptable time frames. This does in turn lead to sub-optimal designs, in which, e.g., engine efficiency has to be traded for lower noise levels. With improved predictive capabilities, this trade-off can be minimized, leading to quieter and more fuel-efficient engines.

This thesis aims at contributing to the SRIA targets by developing and analyzing a set of numerical methods that are relevant for predicting turbomachinery tonal noise. Tonal noise represents a part of the noise spectrum generated by the fan, the compressors, and the turbines in an aircraft engine. It is characterized by the fact that it occurs at discrete frequencies, which are integer multiples of the blade passing frequencies of the rotating blades rows. The other part of the noise spectrum generated by the turbomachinery components in the engine is commonly denoted broadband noise, since it occurs across a

---

<sup>1</sup>Increase in revenue passenger kilometers globally. Prediction made for years 2019-2038 [2]

wider frequency spectrum.

Hubbard [47] nicely illustrates how the theory of Ffowcs Williams and Hawkings [24] can be used to explain the origin of tonal and broadband noise. Tonal noise is generated by monopole, dipole, and quadrupole noise sources. Monopole sources occur due to the volume displacement of air that a turbomachinery blade gives rise to each time it passes a certain region in space. Since this process must repeat itself each time a blade passes by, the associated noise, known as thickness noise, will occur at integer multiples of the blade passing frequency of the associated blade row. The non-uniform pressure on the blade surface that is generated as a result of aerodynamic loading further gives rise to dipole sources. If the loading of the blade is steady, these sources give rise to noise with the same frequencies as the thickness noise. Aerodynamic interaction between adjacent blade rows can also give rise to unsteady blade loading. In this case, the dipole sources will generate noise that occurs at integer linear combinations of the blade passing frequencies of the interacting blade rows. Dipole noise generated by steady and unsteady loading of the blades is commonly denoted loading noise. Finally, if shock waves are attached to the blades, quadrupole noise will be generated. If the shock is stationary relative to the blade, this noise will occur at the same frequencies as the thickness and the steady loading noise. On the other hand, if the shock oscillates as a result of aerodynamic interaction, it will generate noise at the same frequencies as the unsteady loading noise.

As noted previously, broadband noise contains a wide range of frequencies. This is because broadband noise is caused, directly or indirectly, by turbulence. The direct generation of noise by turbulence is not the most important contributor to turbomachinery broadband noise. Instead, it is the indirect effect that turbulence has on the blade pressure distribution that is the main contributor to turbomachinery broadband noise [47]. Furthermore, this noise is primarily generated close to the leading and trailing edge, as a result of turbulence impinging on the blade, or a turbulent boundary layer reaching the trailing edge.

Although the theory developed by Ffowcs Williams and Hawkings [24] describes how the unsteady flow and the movement of the blades generate noise, it does not provide any information about how the flow behaves in itself. Noise predictions based on [24] are therefore commonly performed in a two-step procedure: In the first step, the unsteady flow in the vicinity of the blades is determined by some suitable method, such as computational fluid dynamics (CFD). After this, the noise levels can be determined based on the theory of Ffowcs Williams and Hawkings [24]. In this case, the two steps are often referred to as the source prediction, and the noise propagation step, respectively. The latter name stems from the fact that the theory of Ffowcs Williams and Hawkings [24] allows one to determine the noise at any point in space, as a summation (integral) over all noise sources. As such, it can be thought of as a way to describe how noise propagates between the source and the observer.

Figure 1.1 illustrates one way in which the aforementioned procedure can be used to predict fan noise from a turbofan engine. The green part that surrounds the fan and the outlet guide vanes (OGVs) in this figure denotes the region in which the sources are determined by, e.g., CFD. This region is in turn connected to a red region, in which the flow disturbances generated by the fan/OGV will propagate until they reach the inlet/outlet of the engine (blue lines in the figure). Propagation of flow disturbances in

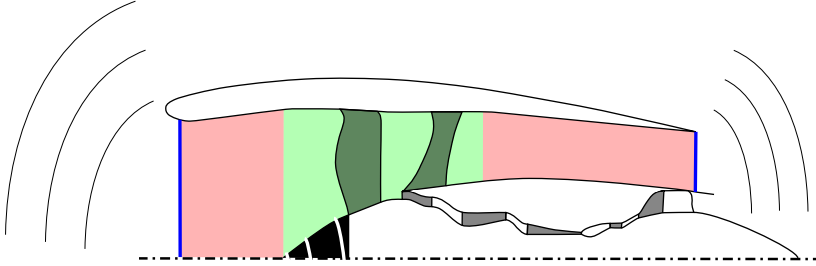


Figure 1.1: *Illustration of noise prediction approach adopted in the present thesis.*

this region can also be computed by CFD. Due to the high computational cost of CFD, however, dedicated tools based on e.g. the linearized Euler equations are sometimes used for this purpose instead. Finally, the region outside the blue lines in Fig. 1.1 denotes the region in which noise is propagated based on the theory of Ffowcs Williams and Hawkings [24].

The noise prediction process illustrated in Fig. 1.1 by no means represents the only way that fan noise can be estimated. Instead, Fig. 1.1 was selected mainly to illustrate how the different numerical methods considered in the present thesis can be combined to predict fan noise. In what follows, each of the methods that have been considered in this thesis will be briefly described and connected to Fig. 1.1. In addition to this, some related work will be covered. A detailed description of each method will be provided in the upcoming chapters.

## 1.1 Source Prediction

In the present thesis, the unsteady flow field inside the turbomachine is modeled by the unsteady, Favre averaged, Navier-Stokes equations. These equations describe how large scale flow structures evolve in space and time. This makes the equations suitable for modeling tonal noise, but not broadband noise, since most of the turbulent spectra is removed by the Favre averaging procedure. Since turbulent fluctuations have been removed from the solution, it will also be deterministic in nature. In particular, the solution will, due to the relative rotation between adjacent blade rows, typically be periodic in time.

The periodic nature of turbomachinery flows can be taken advantage of by directly seeking periodic solutions in the form of a Fourier series in time, with spatially varying coefficients. Unfortunately, the nonlinear nature of the Favre averaged Navier-Stokes equations implies that all terms in this Fourier series are coupled. This does in turn lead to a large set of coupled equations, which become complicated to solve. To avoid this problem, early approaches based on the Fourier series ansatz solved a linearized set of equations instead [37]. This assumption is valid as long as the amplitude of the flow perturbations is small compared to the mean flow. When this assumption is valid, the linearized approach is both accurate and computationally efficient [30].

Coupled, multistage simulations of turbomachines based on the linearized equations can however become quite complicated [18]. This is because the flow often gets reflected against the blade rows, leading to a feedback loop in which a disturbance caused by one blade row reflects against, e.g., a downstream blade row and then propagates upstream to influence the flow in the original blade row. To model this coupling, several linearized simulations are needed [30]. This does in turn require a correct modal decomposition of the flow at the blade row interfaces, to ensure that upstream and downstream propagating modes are correctly transferred between the blade rows [18]. In addition to this, highly accurate nonreflecting boundary conditions are required to ensure that the modes are not artificially reflected at the inlet/outlet of the domain.

Another approach for performing coupled simulations based on linearized equations was proposed by Hall et al. [39]. In this approach, all linearized simulations are performed in parallel, and the coupling of the blade rows is enforced in each iteration. The benefit of this approach is that it gives a tighter coupling of the different blade rows. In addition to this, it should also be less reliant on the accuracy of the nonreflecting boundary condition.

In cases when the linearized assumption is not valid, the use of nonlinear methods becomes necessary. The most intuitive one is to directly integrate the nonlinear, unsteady, Favre averaged Navier-Stokes equations in time, using a sliding-grid approach for coupling the blade rows [87, 4]. This approach is attractive since it does not make any assumptions on the temporal behavior of the flow, and since it accounts for nonlinear coupling between different frequency components in the solution. Its general nature does however come at a high computational cost. The first reason for this is that the solution often must be integrated over a long time interval before the final, periodic solution is obtained. Time-accurate simulations may also require that all blades in each row are included in the simulation. This is in contrast to linearized, frequency domain approaches, that enable the use of phase-shifted periodic boundary conditions. Phase-shifted periodic boundary conditions can also be incorporated into time-accurate simulations with the so-called Chorochronic approach [41, 32, 90, 8, 81].

In this thesis, a third alternative for simulating the unsteady flow around turbomachinery blades, known as the time-domain Harmonic Balance method [38], has been used. Similar to the linearized approach described earlier, the Harmonic Balance method expresses the solution as a Fourier series in time, with spatially varying coefficients. By sampling the solution at a set of time instances, a high order finite difference operator that approximates the time derivative can then be constructed based on the discrete Fourier transform, and its inverse. The Harmonic Balance method can also be formulated in the frequency-domain [72]. In this case, the sampling of the solution is used to approximate the Fourier coefficients of the nonlinear equations using the discrete Fourier transform.

The Harmonic Balance method generally turns out to be more computationally efficient than the time integration approach, since it directly seeks a periodic solution, and since it works effortlessly with phase-shifted periodic boundary conditions [29, 96, 45, 10, 6, 15, 73]. The fact that the Harmonic Balance method relies on the discrete Fourier transform also introduces new challenges. To begin with, the standard discrete Fourier transform assumes that the underlying signal is periodic in time. For many applications, this assumption is not valid. Fortunately, there are several variations of the discrete Fourier transform that address this problem. In the present work, the almost periodic

Fourier transform (APFT) has been adopted. The APFT was originally introduced in the electronics community by Kundert et al. [56, 57], and later adapted within the CFD community in e.g. [36, 80, 46, 50]. As indicated above, the APFT is applicable when the solution contains an arbitrary set of frequencies.

Another challenge associated with the discrete Fourier transform is aliasing. Aliasing occurs when the signal contains frequency components other than those accounted for by the discrete Fourier transform. This problem can be minimized by employing oversampling. For problems that contain frequencies that are multiples of a single fundamental frequency, the number of time samples that give an alias-free Fourier transform can be obtained from the Whittaker-Kotel'nikov-Shannon sampling theorem [104, 52, 93], provided that the bandwidth of the signal is known. The bandwidth can be determined for single-frequency problems if the governing equations only contain polynomials of known degree [83, 59, 29]. For multiple frequency problems, the time sampling is harder to determine. The present work addresses this problem by introducing a new operator, called the *alias operator*, that describes how an unresolved frequency alias onto the resolved ones. This alias operator is then used to develop time sampling strategies that minimize aliasing for both single frequency computations based on the standard discrete Fourier transform, as well as multiple frequency computations based on the APFT [68].

When the Harmonic Balance method is applied to the spatially discretized Favre averaged Navier Stokes equations, a set of coupled, nonlinear equations is obtained. These equations are commonly solved using local time stepping. Local time stepping implies that an additional (pseudo-) time derivative is added to the equations, after which they are integrated in (pseudo-) time until steady-state is reached. Local time stepping can be performed using either an explicit or implicit approach. In the explicit approach, the equations are expressed as a function of known quantities, whereas in the implicit approach, they are expressed in terms of both known and unknown quantities (such as the solution at the next time step). The explicit approach is both easier to implement, and requires a lower computational cost per time step, compared to the implicit approach. The implicit approach can on the other hand be made unconditionally stable, meaning that it can tolerate arbitrary large time steps [42]. For this reason, the best approach (explicit or implicit) can vary between different applications. In [31], a linear stability analysis was performed to investigate under what conditions explicit pseudo-time integration using the Runge-Kutta method is stable. There, it was shown that numerical stability is governed by two parameters, the well-known Courant–Friedrichs–Lewy (CFL) number, and a parameter called the grid reduced frequency. Based on this analysis, a restriction of the pseudo-time step based on local values of the CFL number and the grid reduced frequency was proposed [31]. Similar restrictions had also been proposed earlier by e.g. [103, 48, 71]. In this work, a linear stability analysis has also been performed [62, 63]. In addition to confirming known stability properties of the Harmonic Balance method, the stability analysis presented in this work clearly shows how the eigenvalue spectra of the spatial discretization is altered by the temporal discretization. In [62, 63], some proposed stabilization approaches for the Harmonic Balance method have also been investigated. These include the pseudo-time step restriction proposed by Weide et al. [103], the point-implicit Runge-Kutta method proposed in [72, 6], and the stabilization matrix proposed by Thomas et al. [100]. In addition to this, a novel time-level preconditioner for the time

domain Harmonic Balance method is proposed in the present work. This preconditioner ensures that the pseudo-time-step is as large as possible, without violating the stability conditions of the chosen pseudo-time integration scheme.

Boundary conditions are another important aspect of computational fluid dynamics. In general, boundary conditions need to impose the right operating condition for the turbomachine, while at the same time ensuring that the results are insensitive to the position of the inlet/outlet boundaries. Over the past decades, several different techniques have been developed to satisfy these requirements, each one having its strengths and weaknesses. Generally speaking, these techniques fall into two categories. In the first category, the aim is to dampen all waves before they reach the inlet/outlet boundaries, leading to negligible amplitudes of the reflected waves. Notable techniques in this category are grid stretching, sponge layers [49], and perfectly matched layers [44]. The use of grid stretching and sponge layers have been exploited in this thesis since they are generic and easy to implement. The accuracy of these approaches does however critically depend on the size of the domain in which they are applied, with larger sizes (and low damping), giving the most accurate results. This necessitates the use of a large computational domain, which is computationally expensive. For this reason, the second category, known as nonreflecting boundary conditions, becomes attractive. The purpose of a nonreflecting boundary condition is to ensure that waves can impinge on the boundary, without being reflected. Among the most popular nonreflecting boundary conditions for turbomachinery applications we find the one dimensional nonreflecting boundary condition based on characteristic variables [16], the exact and approximate, two dimensional nonreflecting boundary conditions developed by Giles [34, 33] and Hall et al. [37], and the three dimensional nonreflecting boundary conditions developed by Hall et al. [40] and Moinier et al. [75]. Here, the dimension of the boundary condition indicates the underlying assumption used to construct the boundary condition. For example, the boundary condition developed by Giles [34, 33] and Hall et al. [37] assumes that the flow close to the boundary obeys the two dimensional, linearized Euler equations.

In the present work, the exact, nonlocal, nonreflecting boundary condition developed by Giles [34, 33] and Hall et al. [37] have been considered. In particular, a great effort was put towards obtaining a generic formulation of this boundary condition that would be possible to use for both steady-state simulations, as well as unsteady simulations using the Harmonic Balance method. After implementing this formulation, it was found that numerical stability could not be ensured. This problem has also been reported by other authors [29, 51] using a similar type of solver as the one employed in the present work. In [51], it was also reported that the reformulation of the boundary condition originally suggested by [33] improved the numerical stability considerably. Inspired by this finding, the present work has also implemented the reformulation suggested by [33]. In chapter 3, both the original formulation, and the reformulation proposed in [33], will be provided. In addition to this, the stability and accuracy of both implementations will be investigated in Appendix B.

## 1.2 Noise Propagation

Pioneering work on noise propagation in ducts was conducted by Tyler and Sofrin [101]. In their work, the authors considered how noise generated by a single fan stage (rotor+stator) propagated upstream through an inlet duct with a constant cross-section. To begin with, it was shown that the tonal noise must be generated at discrete frequencies, equal to the blade passing frequency of the rotor. Each of these frequencies must in turn be associated with a set of spinning modes, whose nodal diameters are given by the well-known Tyler-Sofrin rule [101]. When the mean flow through which the noise propagates is uniform and contains no swirl component, which is a good approximation for the inlet duct, Tyler and Sofrin [101] also showed that each of these spinning modes could be written as a sum of Bessel functions. In the context of noise propagation in ducts, these Bessel functions are often called duct modes.

Each Bessel function, or duct mode, can be shown to be associated with a certain axial wavenumber. This makes it possible to calculate how noise propagates along the duct by first decomposing it into spinning modes, then further into duct modes. Unfortunately, this is only possible to do analytically for very simple mean flows, such as the axially uniform one considered by Tyler and Sofrin [101]. For more realistic situations, such as when the mean flow contains radial variations in both axial and tangential velocity, numerical methods must instead be adopted.

A popular method for numerically computing duct modes is the normal mode analysis, see e.g. [54, 79, 70, 40, 74, 51]. Other methods include solving an initial boundary value problem [99], or using a Green's function approach [84]. Although many codes have been developed to compute duct modes based on the normal mode analysis approach, there appeared to exist no publicly available ones. After reviewing the literature, it also became apparent that different research groups made different assumptions in their respective implementation, which naturally makes it hard to compare results back-to-back. For this reason, it was decided to create an open-source tool for computing duct modes. In addition to making the code open-source, a large effort was also put into documenting both the underlying theory and how to use the code. The result of this effort is **noisyduck**, an open-source tool for computing duct modes using a normal mode analysis [105]. The numerical method employed in **noisyduck** will be detailed in section 3.3. Further validation of the code will also be provided in Appendix C.

Most methods in use today for relating noise sources in the near field, to the noise at an observer in the far-field, are based on the famous Ffowcs Williams - Hawkings equation [24]. The Ffowcs Williams - Hawkings equation is in turn an extension of the Lighthill equation [60, 61] to account for the presence of moving surfaces. In the original paper by Ffowcs Williams and Hawkings [24], these surfaces were taken to be solid surfaces. The theory developed in [24] is however equally applicable to any surface that encloses all solid boundaries [26]. In the latter case, the surface is often denoted permeable, to emphasize that the fluid is allowed to cross it.

The Ffowcs Williams - Hawkings equation can be formally solved with a Green's function. In particular, the same Green's function can be used for both the permeable and solid surface formulation of the Ffowcs Williams - Hawkings equation [26, 21]. The formal solution to these equations is however not suitable for numerical implementations. Much

effort has therefore been devoted to reformulating the formal solution in a way that better suits numerical needs. Among the most widely adopted formulations in use today we find Formulation 1 and 1A by Farassat [21]. In the present work, Formulation 1C proposed by Najafi-Yazidi et al. [78] has been adopted. This formulation is similar to Formulation 1A, with the main difference being that a convective form of the Ffowcs Williams - Hawkings equation is solved in order to account for convective effects introduced by a mean flow.

### 1.3 Purpose and Limitations

The purpose of this thesis is to apply, evaluate, and develop the following numerical methods for the purpose of predicting turbomachinery tonal noise

- The Harmonic Balance method proposed by Hall et al. [38]
- The exact, nonlocal, nonreflecting boundary condition proposed by Giles [34, 33] and Hall et al. [37]
- The acoustic analogy proposed by Najafi-Yazidi et al. [78]
- A method for computing duct modes based on a normal mode analysis [105]

The applications reported in this thesis range from small test cases, in which specific aspects of the methods are evaluated, to a real-world application where they are combined to predict the tonal noise of a Counter Rotating Open Rotor. The methods are also evaluated from a theoretical perspective. Finally, lessons learned from applying and evaluating the methods are used to suggest improvements.



## 2 Modeling Unsteady Turbomachinery Flows: The Harmonic Balance Method

The flow field within a turbomachine can be simulated by numerically solving some formulation of the Navier-Stokes equations. In this work, the Favre-Averaged Navier-Stokes equations coupled with an eddy-viscosity turbulence model have been used. These equations describe the spatial and temporal evolution of large scale flow structures, and must, therefore, be discretized in both space and time to be solved numerically. For spatial discretization, the Finite-Volume Method method available in the Chalmers-developed G3D::Flow solver has been used [3]. Temporal discretization is further achieved with the Harmonic Balance method [38], which was added to G3D::Flow in this thesis. This chapter starts with a brief overview of the spatial discretization, followed by a more in-depth analysis of the temporal discretization.

The Favre-Averaged Navier-Stokes equations may be written in compact, conservative form as follows

$$\frac{\partial q}{\partial t} + \frac{\partial F_j}{\partial x_j} = S \quad (2.1)$$

In this equation,  $q \in \mathbb{R}^{N_{\text{var}}}$  is a vector that contains the conserved variables. For the Favre-Averaged Navier-Stokes equations, they are the averaged density, momentum, total energy as well as additional variables inherent to the type of turbulence model being used. The remaining two terms in Eq. (2.1),  $F_j$  and  $S$ , respectively contain the total flux (convective + diffusive) of each conserved variable, and possible source terms. More details regarding the mathematical formulation of the governing equations, including how turbulence is modeled, is provided in [3, 81].

The Finite-Volume discretization available in G3D::Flow has been developed for structured, boundary-fitted, curvilinear, non-orthogonal, multi-block meshes. The unknown convective and diffusive fluxes on cell faces that result from this discretization are approximated by a third-order upwind scheme, and a compact, second-order, centered difference scheme, respectively [3, 81]. The final equations resulting from the spatial discretization may be written as follows

$$\frac{\partial \mathbf{q}}{\partial t} + R(\mathbf{q}) = 0 \quad (2.2)$$

Here,  $\mathbf{q} \in \mathbb{R}^{N_{\text{dof}}}$  is a vector that contains cell-averages of the conserved variables<sup>1</sup>. The function  $R(\mathbf{q}) : \mathbb{R}^{N_{\text{dof}}} \rightarrow \mathbb{R}^{N_{\text{dof}}}$  in the above expression, called the residual, further contains the total (convective + diffusive) flux of each conserved variable as well as the cell-averaged source terms.

The residual in Eq. (2.2) is a nonlinear function of  $\mathbf{q}$ . As a consequence of this, solutions to Eq. (2.2) can contain a wide spectrum of frequencies. Fortunately, most of these frequencies will often have a negligible amplitude due to the dissipative nature of

---

<sup>1</sup> $N_{\text{dof}} = N_{\text{var}} \cdot N_{\text{cells}}$  denotes the number of degrees of freedom in the problem

the Favre-Averaged Navier-Stokes equations. This property can be taken advantage of by seeking for approximate solutions to Eq. (2.2) in the form of a truncated Fourier series

$$\mathbf{q} \approx \sum_{n: \omega_n \in \Lambda} \hat{\mathbf{q}}_n e^{i\omega_n t} \quad (2.3)$$

Here,  $\Lambda$  represents the set of frequencies included in the series expansion

$$\Lambda = \{0, \omega_1, \omega_2, \dots, \omega_N, \omega_{-N}, \dots, \omega_{-1}\} \quad (2.4)$$

The only requirement that will be put on these frequencies is that  $\omega_{-n} = -\omega_n$ .

If we would substitute Eq. (2.3) into Eq. (2.2), the resulting set of equations would not be satisfied  $\forall t$ . The reason for this is that  $R(\mathbf{q})$  is a nonlinear function of  $\mathbf{q}$ , and therefore contains more frequencies than those assumed to be present in  $\mathbf{q}$ . Instead, the appropriate way to proceed is to perform a Galerkin projection of Eq. (2.2) onto the subspace spanned by the Fourier harmonics in Eq. (2.3). This gives the following result

$$\mathbf{\Omega}_\Lambda \hat{\mathbf{q}}_\Lambda + \hat{\mathbf{R}}_\Lambda(\hat{\mathbf{q}}_\Lambda) = 0 \quad (2.5)$$

Here,  $\mathbf{\Omega}_\Lambda = \mathbf{\Omega}_\Lambda \otimes \mathbf{I}$ , where  $\otimes$  is the Kronecker product,  $\mathbf{I}$  is an identity matrix of size  $N_{\text{dof}} \times N_{\text{dof}}$ , and

$$\mathbf{\Omega}_\Lambda = \begin{bmatrix} 0 & 0 & \dots & & 0 \\ 0 & i\omega_1 & 0 & \dots & 0 \\ \vdots & 0 & i\omega_2 & 0 & \dots & 0 \\ & \vdots & 0 & \ddots & & 0 \\ & & \vdots & & & 0 \\ 0 & 0 & 0 & 0 & 0 & i\omega_{-1} \end{bmatrix} \quad (2.6)$$

The vectors  $\hat{\mathbf{q}}_\Lambda$  and  $\hat{\mathbf{R}}_\Lambda(\hat{\mathbf{q}}_\Lambda)$  in Eq. (2.5) further consist of  $2N + 1$  sub vectors, in which the  $n^{\text{th}}$  sub vector contains  $\hat{\mathbf{q}}_n$  and  $\hat{\mathbf{R}}_n$  respectively.

The fact that  $R(\mathbf{q})$  is a nonlinear function of  $\mathbf{q}$  unfortunately makes it very hard to calculate  $\hat{\mathbf{R}}_\Lambda(\hat{\mathbf{q}}_\Lambda)$  analytically, especially when  $\#\Lambda$  is large<sup>2</sup>. The Harmonic Balance method overcomes this difficulty by approximating  $\hat{\mathbf{R}}_\Lambda(\hat{\mathbf{q}}_\Lambda)$  as the discrete Fourier transform (DFT) of  $R(\mathbf{q})$

$$\hat{\mathbf{R}}_\Lambda(\hat{\mathbf{q}}_\Lambda) \approx \mathbf{E}_\Lambda(\mathbf{t}) R(\mathbf{E}_\Lambda^{-1}(\mathbf{t}) \hat{\mathbf{q}}_\Lambda) \quad (2.7)$$

The DFT of the residual is computed in two steps. First,  $R(\mathbf{q})$  is sampled at a set of time instances  $\mathbf{t}$

$$\mathbf{t} = \begin{bmatrix} t_0 \\ t_1 \\ \vdots \\ t_{M-1} \end{bmatrix} \quad (2.8)$$

---

<sup>2</sup> $\#\Lambda$  denotes the cardinality of the set  $\Lambda$ , i.e., the number of elements in the set.

This will in turn require the realization of Eq. (2.3) at these time instances

$$\mathbf{q}^* = \mathbf{E}_\Lambda^{-1}(\mathbf{t})\hat{\mathbf{q}}_\Lambda \quad (2.9)$$

Here,  $\mathbf{E}_\Lambda^{-1}(\mathbf{t}) = E_\Lambda^{-1}(\mathbf{t}) \otimes \mathbf{I}$ , where  $E_\Lambda^{-1}(\mathbf{t})$  is defined as

$$E_\Lambda^{-1}(\mathbf{t}) = \begin{bmatrix} 1 & e^{i\omega_1 t_0} & e^{i\omega_2 t_0} & \dots & e^{i\omega_{-1} t_0} \\ 1 & e^{i\omega_1 t_1} & e^{i\omega_2 t_1} & \dots & e^{i\omega_{-1} t_1} \\ \vdots & \vdots & \vdots & & \vdots \\ 1 & e^{i\omega_1 t_{M-1}} & e^{i\omega_2 t_{M-1}} & \dots & e^{i\omega_{-1} t_{M-1}} \end{bmatrix} \quad (2.10)$$

This matrix will hereinafter be referred to as the inverse discrete Fourier transform matrix.

Once the sampling of the residual in Eq. (2.7) has been computed, its discrete Fourier transform is obtained by multiplying it from the left by the inverse of  $\mathbf{E}_\Lambda^{-1}(\mathbf{t})$ , here denoted  $\mathbf{E}_\Lambda(\mathbf{t})$ . For this inverse to be well defined, the columns in  $\mathbf{E}_\Lambda^{-1}(\mathbf{t})$  must be linearly independent. The structure of  $\mathbf{E}_\Lambda^{-1}(\mathbf{t})$  implies that this can only be satisfied if the columns in  $E_\Lambda^{-1}(\mathbf{t})$  are linearly independent. As it turns out, we can always find  $M = 2N + 1$  time samples such that this holds [68]. If we choose such a time sampling, the matrices  $E_\Lambda^{-1}(\mathbf{t})$  and  $E_\Lambda(\mathbf{t})$  will define an almost periodic Fourier transform (APFT) pair [57]. The APFT can be seen as a generalization of the standard discrete Fourier transform in the sense that the frequencies do not need to be harmonically related and that the time sampling does not have to be uniform.

The frequency-domain formulation of the Harmonic Balance method, also known as the nonlinear frequency domain method [72], is obtained by substituting Eq. (2.7) into Eq. (2.5)

$$\Omega_\Lambda \hat{\mathbf{q}}_\Lambda + \mathbf{E}_\Lambda(\mathbf{t})R(\mathbf{E}_\Lambda^{-1}(\mathbf{t})\hat{\mathbf{q}}_\Lambda) = 0 \quad (2.11)$$

The time-domain formulation of the Harmonic Balance method is further obtained by multiplying the above equation from the left by  $\mathbf{E}_\Lambda^{-1}(\mathbf{t})$  and then make use of Eq. (2.9)

$$\underbrace{\mathbf{E}_\Lambda^{-1}(\mathbf{t})\Omega_\Lambda\mathbf{E}_\Lambda(\mathbf{t})}_{\mathbf{D}}\mathbf{q}^* + \mathbf{E}_\Lambda^{-1}(\mathbf{t})\mathbf{E}_\Lambda(\mathbf{t})R(\mathbf{q}^*) = 0 \quad (2.12)$$

The matrix  $\mathbf{D}$  in this equation is known as the time spectral derivative matrix [38]. It represents a high order finite difference operator that, due to its structure, applies locally to the solution in each cell of the mesh. The matrix  $\mathbf{E}_\Lambda^{-1}(\mathbf{t})\mathbf{E}_\Lambda(\mathbf{t})$  in the above equation will further be equal to the identity matrix if  $M = 2N + 1$  time instances are used. If more than  $2N + 1$  time samples on the other hand are used,  $\mathbf{E}_\Lambda^{-1}(\mathbf{t})\mathbf{E}_\Lambda(\mathbf{t}) \neq \mathbf{I}$ . In this case, it represents a low-pass filter that projects the solution onto the subspace spanned by the columns in  $\mathbf{E}_\Lambda^{-1}(\mathbf{t})$ .

The time-domain Harmonic Balance method based on the standard discrete Fourier transform was implemented into G3D::Flow as part of this thesis work. The frequency-domain Harmonic Balance method was also considered in Paper F, but for a simpler problem than the Favre-Averaged Navier-Stokes equations.

## 2.1 Error Sources

The accuracy of the Harmonic Balance method depends on two factors: how well the solution is approximated by the Fourier series in Eq. (2.3), and how well the Fourier coefficients of the residual are approximated by the DFT in Eq. (2.7). The errors introduced by these two factors will here be referred to as the harmonic truncation error, and the alias error, respectively.

### 2.1.1 Harmonic Truncation Error

The harmonic truncation error will always be present when Eq. (2.3) does not contain all relevant frequencies for a particular problem. If Eq. (2.5) would be solved, then the harmonic truncation error would be the only error introduced by the temporal discretization. This is because the Galerkin projection corresponds (up to a constant) to the standard formula for computing Fourier coefficients in this case.

### 2.1.2 Alias Error

Harmonic Balance solutions can, in addition to the harmonic truncation error, also contain the alias error. This error occurs when the signal  $R(\mathbf{q}^*)$  contains more frequencies than those accounted for by the DFT in Eq. (2.7). To illustrate this more clearly, let  $\Lambda'' = \Lambda \cup \Lambda_R$ , where  $\Lambda_R$  denotes the set of all frequencies present in  $R(\mathbf{q}^*)$ . We may then express  $R(\mathbf{q}^*)$  as follows

$$R(\mathbf{q}^*) = \mathbf{E}_{\Lambda''}^{-1}(\mathbf{t})\hat{\mathbf{R}}_{\Lambda''} \quad (2.13)$$

By definition  $\Lambda \subset \Lambda''$ . Equation (2.13) can therefore be rewritten as

$$R(\mathbf{q}^*) = \mathbf{E}_{\Lambda}^{-1}(\mathbf{t})\hat{\mathbf{R}}_{\Lambda} + \mathbf{E}_{\Lambda'' \setminus \Lambda}^{-1}(\mathbf{t})\hat{\mathbf{R}}_{\Lambda'' \setminus \Lambda} \quad (2.14)$$

This expression may now be used to express the discrete Fourier transform in Eq. (2.7) as

$$\begin{aligned} \mathbf{E}_{\Lambda}(\mathbf{t})R(\mathbf{E}_{\Lambda}^{-1}(\mathbf{t})\hat{\mathbf{q}}_{\Lambda}) &= \mathbf{E}_{\Lambda} \left( \mathbf{E}_{\Lambda}^{-1}(\mathbf{t})\hat{\mathbf{R}}_{\Lambda} + \mathbf{E}_{\Lambda'' \setminus \Lambda}^{-1}(\mathbf{t})\hat{\mathbf{R}}_{\Lambda'' \setminus \Lambda} \right) \\ &= \hat{\mathbf{R}}_{\Lambda} + \mathbf{E}_{\Lambda}(\mathbf{t})\mathbf{E}_{\Lambda'' \setminus \Lambda}^{-1}(\mathbf{t})\hat{\mathbf{R}}_{\Lambda'' \setminus \Lambda} \end{aligned} \quad (2.15)$$

This equation shows that the DFT in Eq. (2.7) consists of two terms. The first term represents the correct (alias-free) Fourier coefficients that correspond to the resolved frequencies. These Fourier coefficients are in fact the same as those obtained from the Galerkin projection. The second term further represents the fold back of the unresolved Fourier coefficients onto the resolved ones. The operator  $\mathbf{E}_{\Lambda}(\mathbf{t})\mathbf{E}_{\Lambda'' \setminus \Lambda}^{-1}(\mathbf{t})$  that defines the fold back of the unresolved Fourier coefficients Eq. (2.15) is here referred to as the *alias operator*. Based on Eq. (2.15), it is straightforward to show that this operator provides

the following bound on the alias error

$$\frac{\|\tilde{\mathbf{R}}_\Lambda - \hat{\mathbf{R}}_\Lambda\|_2}{\|\hat{\mathbf{R}}_{\Lambda'' \setminus \Lambda}\|_2} \leq \|E_\Lambda(\mathbf{t})E_{\Lambda'' \setminus \Lambda}^{-1}(\mathbf{t})\|_2 \quad (2.16)$$

Here,  $\tilde{\mathbf{R}}_\Lambda$  denotes the Fourier coefficients obtained from the DFT in Eq. (2.7).

The alias operator is also related to the condition number of the DFT matrices. To prove this, we start by defining the condition number based on the  $l_2$  norm as

$$\kappa(E_\Lambda^{-1}(\mathbf{t})) = \|E_\Lambda^{-1}(\mathbf{t})\|_2 \|E_\Lambda(\mathbf{t})\|_2 \quad (2.17)$$

This definition may now be used to derive the following relation

$$\begin{aligned} \|E_\Lambda(\mathbf{t})E_{\Lambda'' \setminus \Lambda}^{-1}(\mathbf{t})\|_2 &\leq \|E_\Lambda(\mathbf{t})\|_2 \|E_{\Lambda'' \setminus \Lambda}^{-1}(\mathbf{t})\|_2 \\ &= \kappa(E_\Lambda^{-1}(\mathbf{t})) \underbrace{\frac{\|E_{\Lambda'' \setminus \Lambda}^{-1}(\mathbf{t})\|_2}{\|E_\Lambda^{-1}(\mathbf{t})\|_2}}_{\alpha(\Lambda, \Lambda'', \mathbf{t})} \end{aligned} \quad (2.18)$$

The parameter  $\alpha(\Lambda, \Lambda'', \mathbf{t})$  in this equation must be bounded since the inverse discrete Fourier transform matrix is a bounded operator that by definition is never zero. From this, it follows that the norm of the alias operator is bounded by the condition number in the following way

$$\|E_\Lambda(\mathbf{t})E_{\Lambda'' \setminus \Lambda}^{-1}(\mathbf{t})\|_2 \leq \kappa(E_\Lambda^{-1}(\mathbf{t})) \max_{\mathbf{t}} \{\alpha(\Lambda, \Lambda'', \mathbf{t})\} \quad (2.19)$$

This equation shows that it is favorable from an aliasing perspective to perform the Harmonic Balance computation with a discrete Fourier transform whose condition number is low. A low condition number is also beneficial since it ensures that the columns in the matrix  $E_\Lambda^{-1}(\mathbf{t})$  are linearly independent.

## 2.2 Selection of Time Sampling

The condition number of the DFT matrices can be controlled by a careful selection of the time sampling. When  $\Lambda$  contains a single fundamental frequency and its harmonics, a uniform time sampling between 0 and the reciprocal of the fundamental frequency gives the lowest possible condition number of  $\kappa(E_\Lambda^{-1}(\mathbf{t})) = 1$  [57]. This corresponds to the standard discrete Fourier transform, which is used almost exclusively in single-frequency Harmonic Balance computations. In contrast to the single-frequency case, no analytical way of determining the time sampling such that the condition number of the DFT matrices is minimized appears to exist for the multiple frequency case. Instead, different optimization algorithms are usually employed for this purpose [57, 56, 50, 58, 86, 36, 80].

### 2.2.1 Oversampling

Although a low condition number provides a bound on aliasing through Eq. (2.19), it does not eliminate aliasing when only  $M = 2N + 1$  time samples are employed. This can be proven by first noting that the columns in  $E_{\Lambda}^{-1}(\mathbf{t})$  are required to be linearly independent. From this, it follows that there exists a nonzero matrix  $W$  such that  $E_{\Lambda'' \setminus \Lambda}^{-1}(\mathbf{t}) = E_{\Lambda}^{-1}(\mathbf{t})W$ . But then, the alias operator in Eq. (2.15) must be equal to  $E_{\Lambda}(\mathbf{t})E_{\Lambda'' \setminus \Lambda}^{-1}(\mathbf{t}) = W \neq 0$ , which proves the desired result.

Aliasing can on the other hand be eliminated when  $M'' > 2N + 1$  time samples are employed. In this case, the matrix  $\mathbf{E}_{\Lambda}(\mathbf{t})$  in Eqs. (2.11) and (2.12) represents a left inverse to  $\mathbf{E}_{\Lambda}^{-1}(\mathbf{t})$ . Contrary to the standard inverse of a square matrix, however, the left inverse is not uniquely defined. This gives us the possibility to tailor it in such a way that aliasing is eliminated. Let this tailored inverse be denoted  $E_{\Lambda, \Lambda''}(\mathbf{t})$ . It then follows that it satisfies the following two conditions

$$\begin{aligned} E_{\Lambda, \Lambda''}(\mathbf{t})E_{\Lambda}^{-1}(\mathbf{t}) &= \mathbf{I} \\ E_{\Lambda, \Lambda''}(\mathbf{t})E_{\Lambda'' \setminus \Lambda}^{-1}(\mathbf{t}) &= \mathbf{0} \end{aligned} \quad (2.20)$$

If  $M'' = \#\Lambda''$  time samples are chosen such that the columns in  $E_{\Lambda''}^{-1}(\mathbf{t})$  are linearly independent, the above expression may be rewritten as follows

$$E_{\Lambda, \Lambda''}(\mathbf{t}) = \pi_{\Lambda'', \Lambda} E_{\Lambda''}(\mathbf{t}) \quad (2.21)$$

Here,  $\pi_{\Lambda'', \Lambda}$  is the projection operator that eliminates all rows in  $E_{\Lambda''}(\mathbf{t})$  that do not correspond to frequencies in  $\Lambda$ .

The benefit of using the left inverse defined in Eq. (2.21) is that it eliminates aliasing. Employing this left inverse is also more computationally expensive since the residual must be evaluated at  $M'' > 2N + 1$  time instances. This motivates the use of a left inverse which requires less than  $M''$  time instances but still has the potential to reduce aliasing compared to not using oversampling at all. To define this left inverse, we introduce a new set of frequencies  $\Lambda'$  that satisfies

$$\Lambda \subset \Lambda' \subseteq \Lambda'' \quad (2.22)$$

If we choose  $M' = \#\Lambda'$  time samples such that  $E_{\Lambda'}^{-1}(\mathbf{t})$  is invertible, we may define the following left inverse

$$E_{\Lambda, \Lambda'}(\mathbf{t}) = \pi_{\Lambda', \Lambda} E_{\Lambda'}(\mathbf{t}) \quad (2.23)$$

The idea behind this left inverse is to eliminate aliasing with respect to the frequencies in  $\Lambda' \setminus \Lambda$ . This left inverse would also completely eliminate aliasing if a time sampling can be found such that the unresolved Fourier coefficients only contribute to the amplitude of the Fourier coefficients whose frequencies are in  $\Lambda' \setminus \Lambda$ .

The left inverse can also be calculated as the Moore-Penrose inverse of  $E_{\Lambda}^{-1}(\mathbf{t})$  [13, 14, 50]. This left inverse represents a least squares projection onto the subspace spanned by the columns in  $E_{\Lambda}^{-1}(\mathbf{t})$ . This does in turn mean that the columns in  $E_{\Lambda'' \setminus \Lambda}^{-1}(\mathbf{t})$  must be orthogonal to those in  $E_{\Lambda}^{-1}(\mathbf{t})$  in order for this left inverse to eliminate aliasing.

In Paper F, the impact of time sampling on the aliasing produced in Harmonic Balance computations was evaluated. There, it was found that a time sampling which minimizes the condition number of the DFT matrices was the optimal choice when no oversampling was employed. When oversampling on the other hand was employed, it was found to be beneficial to employ the left inverse defined by Eq. (2.23) over the Moore-Penrose inverse. The time samplings that were used for this comparison were also chosen to minimize the condition number of the DFT matrices. In particular, the time sampling used for Eq. (2.23) was chosen to minimize the condition number of the square matrix  $E_{\Lambda'}(\mathbf{t})$ .

## Implementation Considerations

We conclude this section by looking at how an existing Harmonic Balance solver can be extended to include oversampling. When the frequency-domain formulation is used (Eq. (2.11)), this is easily achieved by increasing the number of time instances at which the residual is sampled, and then use the chosen left inverse to calculate its discrete Fourier transform. When the time-domain Harmonic Balance formulation on the other hand is used (Eq. (2.12)), some additional care is needed. To begin with, the time spectral derivative should naturally be computed using the chosen left inverse. In addition to this, the residual must be low pass filtered (see Eq. (2.12)). This latter step is easy to forget, since no filtering operation is used when  $M = 2N + 1$  time samples are used. Including the filtering step is however of paramount importance, since unresolved Fourier coefficients otherwise can contaminate the solution, and thus reduce the accuracy of the results. Avoiding the filtering operation can also lead to completely redundant solutions. To see this, note that the left inverse contains more columns than rows. From this, it follows that there exists a  $\mathbf{q}' \neq 0$ , containing only unresolved frequencies, such that  $\mathbf{E}_{\Lambda}(\mathbf{t})\mathbf{q}' = 0$ . From the definition of the time spectral derivative matrix, it follows that  $\mathbf{D}\mathbf{q}' = 0$  as well. This is clearly not physically correct, since  $\mathbf{q}'$  corresponds to an oscillation whose time derivative is zero. By incorporating the low pass filter, these types of non-physical solutions can be avoided since the residual is projected onto a subspace spanned by the columns in  $\mathbf{E}_{\Lambda}^{-1}(\mathbf{t})$ . That is, no oscillations that satisfy  $\mathbf{D}\mathbf{q}' = 0$  will be added to the solution.

## 2.3 Stability Analysis

The Harmonic Balance solver implemented in G3D::Flow uses local time stepping to solve Eq. (2.12). Local time stepping is based on adding an additional, fictive, time derivative to the governing equations, and then integrate them in pseudo-time until a steady-state is reached. The number of iterations required to reach a steady-state can typically be reduced by employing a large pseudo-time-step. If the time-step is chosen too large, however, the solution might instead diverge. In order to prevent this, an upper bound on the time-step that ensures convergence of the solution will be derived in this section by performing a stability analysis.

The model problem for the stability analysis is the one dimensional, linearized, Euler

equations for a calorically perfect, ideal gas

$$\frac{\partial q'}{\partial t} + \bar{A} \frac{\partial q'}{\partial x} = 0 \quad (2.24)$$

Here,  $q' = (\rho', v'_x, p')^T$  contains perturbations of the primitive flow variables with respect to a spatially+temporally uniform mean flow  $\bar{q}$ . The matrix  $\bar{A}$  in the above equation is further known as the flux Jacobian

$$\bar{A} = \begin{bmatrix} \bar{v}_x & \bar{\rho} & 0 \\ 0 & \bar{v}_x & 1/\bar{\rho} \\ 0 & \bar{\rho} \bar{c}^2 & \bar{v}_x \end{bmatrix} \quad (2.25)$$

The diagonalization of this matrix reads as follows

$$\bar{A} = W \Lambda W^{-1} \quad (2.26)$$

Here, the matrices  $W$ ,  $\Lambda$  and  $W^{-1}$  respectively contain the right eigenvectors, eigenvalues, and left eigenvectors to  $\bar{A}$ . These matrices read as follows

$$\begin{aligned} W &= \begin{bmatrix} \bar{\rho} & \bar{\rho} & \bar{\rho} \\ 0 & \bar{c} & -\bar{c} \\ 0 & \bar{\rho} \bar{c}^2 & \bar{\rho} \bar{c}^2 \end{bmatrix} & \Lambda &= \begin{bmatrix} \bar{v}_x & 0 & 0 \\ 0 & \bar{v}_x + \bar{c} & 0 \\ 0 & 0 & \bar{v}_x - \bar{c} \end{bmatrix} \\ W^{-1} &= \begin{bmatrix} \frac{1}{\bar{\rho}} & 0 & \frac{-1}{\bar{\rho} \bar{c}^2} \\ 0 & \frac{1}{2\bar{c}} & \frac{1}{2\bar{\rho} \bar{c}^2} \\ 0 & \frac{-1}{2\bar{c}} & \frac{1}{2\bar{\rho} \bar{c}^2} \end{bmatrix} \end{aligned} \quad (2.27)$$

The columns in  $W$  represent planar waves that propagate along the x-axis with a speed given by the corresponding eigenvalue in  $\Lambda$ . The amplitudes of these waves are further determined as  $W^{-1}q'$ .

The stability analysis will be performed by first discretizing Eq. (2.24) in space and time, and then analyze how different modes in the solution grow as the equations are integrated in pseudo-time. We start by computing the spatial discretization of Eq. (2.24) using the Finite-Volume method. For simplicity, this will be done on a uniform mesh that consists of  $2K + 1$  equally sized cells of size  $\Delta x$ , see Fig. 2.1. The Finite-Volume method

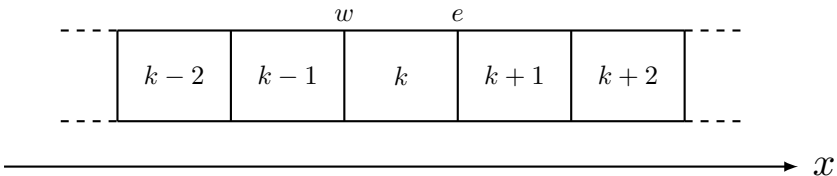


Figure 2.1: *Illustration of mesh used for stability analysis.*



is based on first integrating Eq. (2.24) over one cell in the mesh, and then apply Gauss' divergence theorem to the spatial derivative

$$\Delta x \frac{\partial q'_k}{\partial t} + \bar{A} (q'_e - q'_w) = 0 \quad (2.28)$$

Here,  $q'_k$  contains the cell-averaged primitive flow variables in the  $k^{\text{th}}$  cell. The vectors  $q'_e$  and  $q'_w$  in the above equation further contain face values of the primitive flow variables at the east and west face respectively. These face values are unknown, and must therefore be estimated with some numerical scheme. The numerical scheme used in G3D::Flow is based on first splitting the face values into right and left going waves according to

$$\Delta x \frac{\partial q'_k}{\partial t} + \bar{A} (W_r W_r^{-1} (q'_{e,r} - q'_{w,r}) + W_l W_l^{-1} (q'_{e,l} - q'_{w,l})) = 0 \quad (2.29)$$

Here, subscripts  $\square_l$  and  $\square_r$  were added to the face values to indicate whether they will be projected onto the right or left going waves. These face values are then calculated as a linear combination of the surrounding cell values as follows

$$\begin{aligned} q'_{e,r} &= a_1 q'_{k-1} & + a_2 q'_k & & + a_3 q'_{k+1} & + a_4 q'_{k+2} \\ q'_{w,r} &= a_1 q'_{k-2} & + a_2 q'_{k-1} & + a_3 q'_k & + a_4 q'_{k+1} \\ q'_{e,l} &= a_1 q'_{k+2} & + a_2 q'_{k+1} & + a_3 q'_k & + a_4 q'_{k-1} \\ q'_{w,l} &= a_1 q'_{k+1} & + a_2 q'_k & + a_3 q'_{k-1} & + a_4 q'_{k-2} \end{aligned} \quad (2.30)$$

The weights  $a_i$  in the above equation determine the accuracy of the scheme, as well as the amount of numerical dissipation and dispersion introduced by it. A summary of the different numerical schemes that have been considered for this stability analysis is provided in Table 2.1. More details about the numerical scheme in G3D::Flow is also available in [3].

Abbreviation	Order of Accuracy	$a_1$	$a_2$	$a_3$	$a_4$
FOU	$\mathcal{O}(\Delta x)$	0	1	0	0
TOU	$\mathcal{O}(\Delta x^3)$	-1/6	5/6	2/6	0
TOU-LD	$\mathcal{O}(\Delta x^3)$	-9/96	59/96	53/56	-7/96

Table 2.1: Summary of numerical schemes.

The spatial discretization of Eq. (2.24) also requires that boundary conditions are specified. For simplicity, a periodic boundary condition will be used in this stability analysis. This implies that Eq. (2.30) is modified at the boundaries by selecting, e.g.,  $q'_{2K+2} = q'_1$ . Once the periodic condition has been imposed, the spatial discretization of Eq. (2.24) may be written as

$$\frac{\partial \mathbf{q}'}{\partial t} + R \mathbf{q}' = 0 \quad (2.31)$$

Here,  $\mathbf{q}'$  consists of  $2K + 1$  sub-vectors, in which the  $k^{\text{th}}$  sub-vector contains all elements in  $q'_k$ . The residual operator in the above equation is further defined as

$$R = \frac{1}{\Delta x} \overline{\mathbf{A}} (\mathbf{W}_r \mathbf{W}_r^{-1} \mathbf{F}_r + \mathbf{W}_l \mathbf{W}_l^{-1} \mathbf{F}_l) \quad (2.32)$$

Here,  $\overline{\mathbf{A}} = \mathbf{I} \otimes \overline{A}$ ,  $\mathbf{W}_r \mathbf{W}_r^{-1} = \mathbf{I} \otimes W_r W_r^{-1}$ , and  $\mathbf{W}_l \mathbf{W}_l^{-1} = \mathbf{I} \otimes W_l W_l^{-1}$ , where  $\mathbf{I}$  is an identity matrix of size  $(2K + 1) \times (2K + 1)$ . The matrices  $\mathbf{F}_r$  and  $\mathbf{F}_l$  in Eq. (2.32) in the above equation are further banded, circulant matrices, whose entries read as follows

$$\begin{aligned} \mathbf{F}_r(k, k - 2N_{\text{var}}) &= & - & a_1 & \mathbf{F}_l(k, k - 2N_{\text{var}}) &= & - & a_4 \\ \mathbf{F}_r(k, k - N_{\text{var}}) &= & a_1 & - & a_2 & \mathbf{F}_l(k, k - N_{\text{var}}) &= & a_4 & - & a_3 \\ \mathbf{F}_r(k, k) &= & a_2 & - & a_3 & \mathbf{F}_l(k, k) &= & a_3 & - & a_2 \\ \mathbf{F}_r(k, k + N_{\text{var}}) &= & a_3 & - & a_4 & \mathbf{F}_l(k, k + N_{\text{var}}) &= & a_2 & - & a_1 \\ \mathbf{F}_r(k, k + 2N_{\text{var}}) &= & a_4 & & & \mathbf{F}_l(k, k + 2N_{\text{var}}) &= & a_1 & & \end{aligned} \quad (2.33)$$

Note that the indices in this equation must be modified at the boundaries to impose the periodic condition.

We now proceed by discretizing Eq. (2.31) in time using the time-domain Harmonic Balance method. By following the procedure described earlier, we obtain the following

$$\mathbf{D}\mathbf{q}^* + \mathbf{R}\mathbf{q}^* = 0 \quad (2.34)$$

Here,  $\mathbf{R} = \mathbf{I} \otimes R$ , where  $\mathbf{I}$  is an identity matrix of size  $(2N + 1) \times (2N + 1)$ . What remains is to add a pseudo-time derivative so that the above equation can be solved using local time stepping

$$\frac{\partial \mathbf{q}^*}{\partial \tau} + \mathbf{D}\mathbf{q}^* + \mathbf{R}\mathbf{q}^* = 0 \quad (2.35)$$

Note that once a steady-state is reached, a solution to Eq. (2.34) has been obtained.

Equation (2.35) represents a set of ordinary differential equations that are coupled in space and time through the matrix  $\mathbf{D} + \mathbf{R}$ . These equations will now be converted into a set of uncoupled scalar equations, each one representing the amplitude of one mode in the solution. Here, a mode is defined as an eigenvector to  $\mathbf{D} + \mathbf{R}$ . These eigenvectors are easily obtained by combining the eigenvectors to the different constituents of  $\mathbf{D} + \mathbf{R}$ . To begin with, note that the diagonalization of  $\mathbf{D}$  follows from its definition in Eq. (2.12). The matrix  $\overline{\mathbf{A}}$  in Eq. (2.32) can further be diagonalized by noting that each diagonal sub-block in this matrix is diagonalized by Eq. (2.29). The finite-difference operators  $\mathbf{F}_r$  and  $\mathbf{F}_l$  are finally circulant matrices, and are therefore diagonalized by the discrete Fourier transform (in space). From these observations, it follows that the right eigenvectors to

$\mathbf{D} + \mathbf{R}$  read as follows

$$\mathbf{q}_{p,j,n}^* = \begin{bmatrix} \begin{bmatrix} W_p e^{ik_j x_0} \\ W_p e^{ik_j x_1} \\ \vdots \\ W_p e^{ik_j x_{2K}} \end{bmatrix} e^{i\omega_n t_0} \\ \begin{bmatrix} W_p e^{ik_j x_0} \\ W_p e^{ik_j x_1} \\ \vdots \\ W_p e^{ik_j x_{2K}} \end{bmatrix} e^{i\omega_n t_1} \\ \vdots \\ \begin{bmatrix} W_p e^{ik_j x_0} \\ W_p e^{ik_j x_1} \\ \vdots \\ W_p e^{ik_j x_{2K}} \end{bmatrix} e^{i\omega_n t_{M-1}} \end{bmatrix} \quad (2.36)$$

The axial wavenumber times the spatial coordinate in the above equation may for convenience be expressed as

$$\begin{aligned} k_j x_k &= k_j (k \Delta x) \\ &= k \phi \end{aligned} \quad (2.37)$$

The variable  $\phi = k_j \Delta x$  introduced here represents the relation between the axial wavenumber of the wave, and the highest axial wavenumber that can be resolved on the mesh ( $\pi/\Delta x$ ). Since the number of cells in the mesh can be chosen arbitrarily,  $\phi$  can take on any value between  $(-\pi, \pi)$ .

Now that the eigenvectors to  $\mathbf{D} + \mathbf{R}$  have been defined, we can proceed by deriving a scalar equation that governs the amplitude of one mode (eigenvector) in the solution to Eq. (2.35). This can be done by first noting that the eigenvectors in Eq. (2.36) are linearly independent. From this, it follows that the solution to Eq. (2.35) can be written as a linear combination of these eigenvectors, with weights  $\hat{q}_{p,j,n}$ . By inserting this representation of  $\mathbf{q}^*$  into Eq. (2.35), and then multiply the resulting system of equations by the left eigenvector corresponding to Eq. (2.35), the following scalar equation is obtained

$$\frac{\partial \hat{q}_{p,j,n}}{\partial \tau} + \left( i\omega_n + \frac{\lambda_p}{\Delta x} \xi_p(\phi) \right) \hat{q}_{p,j,n} = 0 \quad (2.38)$$

The expression within the parenthesis in the above equation represents the eigenvalue to  $\mathbf{D} + \mathbf{R}$  that corresponds to the eigenvector in Eq. (2.36). This eigenvalue is in turn composed of eigenvalues to the different constituents in  $\mathbf{D} + \mathbf{R}$ . More precisely, the term  $\lambda_p$  denotes the eigenvalue to  $\bar{A}$  that corresponds to the vector  $W_p$  in Eq. (2.36). The term  $\xi_p(\phi)$  further represents an eigenvalue to the finite difference operator  $\mathbf{F}_r$ , when  $W_p$  is a right going wave, or to  $\mathbf{F}_l$ , when  $W_p$  is a left going wave. An analytical expression for

this eigenvalue can be obtained by applying the finite-difference operator to the spatial Fourier mode in Eq. (2.36)

$$\xi_p(\phi) = \begin{cases} -a_1 e^{-i2\phi} + (a_1 - a_2) e^{-i\phi} + (a_2 - a_3) + (a_3 - a_4) e^{i\phi} + a_4 e^{i2\phi}, & \lambda_p > 0 \\ -a_4 e^{-i2\phi} + (a_4 - a_3) e^{-i\phi} + (a_3 - a_2) + (a_2 - a_1) e^{i\phi} + a_1 e^{i2\phi}, & \lambda_p < 0 \end{cases} \quad (2.39)$$

Note that  $\xi_p(\phi)$  equals the complex conjugate of  $\xi_p(-\phi)$ , and that  $\lambda_p \xi_p(\phi)$  equals the complex conjugate of  $-\lambda_p \xi_p(\phi)$ . Given that  $\phi \in (-\pi, \pi)$ , we may therefore, without loss of generality, restrict ourselves by only considering right going waves in Eq. (2.38). By further omitting all subscripts in this equation, we obtain the following

$$\frac{\partial \hat{q}}{\partial \tau} = - \underbrace{\frac{\lambda}{\Delta x} \left( i\bar{\omega} + \xi(\phi) \right)}_{\Omega} \hat{q} \quad (2.40)$$

Here,  $\Omega$  denotes an eigenvalue to  $-(\mathbf{D} + \mathbf{R})$ . The parameter  $\bar{\omega}$  introduced in the above equation is further defined as

$$\bar{\omega} = \frac{\omega \Delta x}{\lambda} \quad (2.41)$$

This parameter is known as the grid reduced frequency, and it was originally introduced by Gentili [31].

We now proceed by analyzing how the amplitude of one mode evolves as Eq. (2.40) is integrated in pseudo-time. In G3D::Flow, explicit Runge-Kutta schemes are used to integrate the discretized equations in pseudo-time. A general,  $S$ -stage, explicit Runge-Kutta scheme applied to Eq. (2.40) reads as follows [42]

$$\begin{aligned} \hat{q}^{(1)} &= \hat{q}^m \\ \hat{q}^{(2)} &= \hat{q}^m + \Delta\tau \alpha_{2,1} \Omega \hat{q}^{(1)} \\ &\vdots \\ \hat{q}^{(s)} &= \hat{q}^m + \Delta\tau \sum_{r=1}^{s-1} \alpha_{s,r} \Omega \hat{q}^{(r)} \\ &\vdots \\ \hat{q}^{(S)} &= \hat{q}^m + \Delta\tau \sum_{r=1}^{S-1} \alpha_{S,r} \Omega \hat{q}^{(r)} \\ \hat{q}^{(S+1)} &= \hat{q}^m + \Delta\tau \sum_{r=1}^S \beta_r \Omega \hat{q}^{(r)} \\ \hat{q}^{m+1} &= \hat{q}^{(S+1)} \end{aligned} \quad (2.42)$$

Here,  $m$  denotes the pseudo-time step and  $\alpha_{s,r}$ ,  $\beta_r$  are the Runge-Kutta coefficients. These coefficients are commonly summarized in a Butcher tableau, as shown in Table 2.2.

	$\alpha_{2,1}$		
	$\vdots$	$\ddots$	
	$\alpha_{S,1}$	$\dots$	$\alpha_{S,S-1}$
	$\beta_1$	$\dots$	$\beta_{S-1} \quad \beta_S$

Table 2.2: Butcher tableau for Runge-Kutta coefficients.

The two sets of Runge-Kutta coefficients considered in this work are presented in Table 2.3. The first set (Table 2.3a) represents the Runge-Kutta scheme used by the Harmonic Balance solver in G3D::Flow. By inserting these Runge-Kutta coefficients into Eq. (2.42), the following relation between two consecutive time steps is obtained

$$\hat{q}^{m+1} = \underbrace{\left(1 + \Omega\Delta\tau + \frac{1}{2}(\Omega\Delta\tau)^2 + \frac{1}{4}(\Omega\Delta\tau)^3\right)}_{z(\Omega\Delta\tau)} \hat{q}^m \quad (2.43)$$

If the same procedure is followed for the Runge-Kutta coefficients in Table 2.3b, the following relation is obtained

$$\hat{q}^{m+1} = \underbrace{\left(1 + (\Omega\Delta\tau) + \frac{1}{2}(\Omega\Delta\tau)^2 + \frac{1}{6}(\Omega\Delta\tau)^3 + \frac{1}{24}(\Omega\Delta\tau)^4\right)}_{z(\Omega\Delta\tau)} \hat{q}^m \quad (2.44)$$

Equations (2.43) and (2.44) show that the mapping between two consecutive time steps is determined by the function  $z(\Omega\Delta\tau)$ . This function is known as the eigenvalue of the pseudo-time integration scheme [42], and can be seen to depend on the single parameter  $\Omega\Delta\tau$ . For the spatial+temporal discretization used in this work, this parameter reads as follows

$$\begin{aligned} \Omega\Delta\tau &= -\frac{\lambda\Delta\tau}{\Delta x} \left( i\bar{\omega} + \xi(\phi) \right) \\ &= -\sigma \left( i\bar{\omega} + \xi(\phi) \right) \end{aligned} \quad (2.45)$$

Here,  $\sigma$  denotes the well-known Courant–Friedrichs–Lewy (CFL) number.

From Eq. (2.43) (or Eq. (2.44)), it follows that the amplitude of one particular mode will remain bounded if the time-step is selected such that  $|z(\Omega\Delta\tau)| \leq 1$  for the particular values of  $\phi$ ,  $\bar{\omega}$  and  $\lambda$  that define the mode. Since the solution to Eq. (2.35) is a linear

	1		
	1/2	1/2	
	1/2	0	1/2
	(a) RK-3		

	1/4			
	0	1/3		
	0	0	1/2	
	0	0	0	1
	(b) RK-4			

Table 2.3: Butcher tableau for a three stage and a four stage Runge-Kutta method.

combination of all modes, it follows that the solution to this equation will remain bounded if the time-step is chosen such that

$$|z(\Omega\Delta\tau)| \leq 1, \quad \forall \phi, \bar{\omega}, \lambda \quad (2.46)$$

This condition states that the amplitude of each mode must be bounded in order for the complete solution to be bounded.

The stability condition in Eq. (2.46) will be satisfied if all values of  $\Omega\Delta\tau$  obtained from Eq. (2.45) are located inside the contour in the complex plane defined by  $|z(\Omega\Delta\tau)| = 1$ . This contour is commonly referred to as the stability boundary of the pseudo-time integration scheme [42], and is illustrated in Fig. 2.2 for the two Runge-Kutta schemes defined in Table 2.3. In this figure, values of  $\Omega\Delta\tau$  obtained by evaluating Eq. (2.45)  $\forall \phi \in (-\pi, \pi)$ , a couple of values of  $\bar{\omega}$ , and two spatial discretization schemes, have also been included. Looking first at Fig. 2.2a, it can be seen that the amplitude of all modes with zero grid reduced frequency will remain bounded when  $\sigma = 1.2$ . Figure 2.2b shows that the same does not hold for modes with a grid reduced frequency equal to 1. The reason for this is that a non-zero grid reduced frequency will move  $\Omega\Delta\tau$  along the imaginary axis such that it eventually ends up outside of the limited stability boundaries of the two Runge-Kutta schemes considered here.

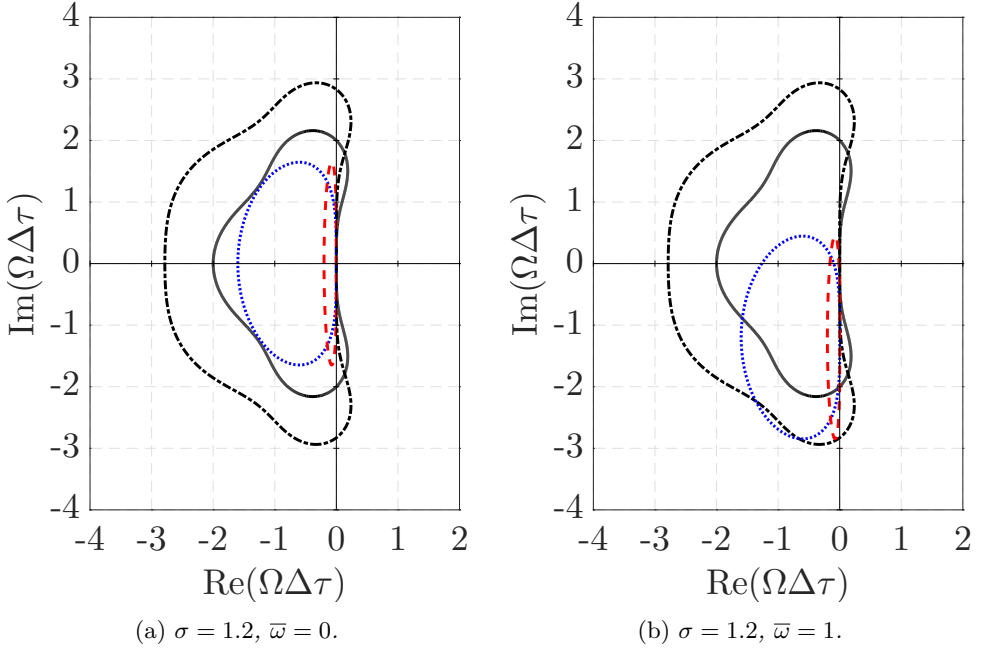


Figure 2.2: Stability boundaries for two Runge-Kutta schemes (— = RK-3, - - - - = RK-4) together with eigenvalue spectra for different combinations of spatial discretization scheme (· · · · · = TOU, - - - - = TOU-LD) and grid reduced frequency.

The stability problem caused by a large grid reduced frequency can be solved by reducing the pseudo-time-step. The relation between the largest pseudo-time-step that ensures stability, here expressed in terms of the CFL number, and the grid reduced frequency is shown in Fig. 2.3. The plots in this figure were derived by finding the largest CFL number such that  $|z(\Omega\Delta\tau)| \leq 1$  for all  $\phi \in (-\pi, \pi)$  and a particular value of  $\bar{\omega}$ . As expected, this figure shows that a higher grid-reduced frequency implies that a smaller CFL number (time-step) must be employed. Next, this result will be used to derive a time-level preconditioner for the Harmonic Balance method such that stability is ensured when the equations are solved with local time stepping.

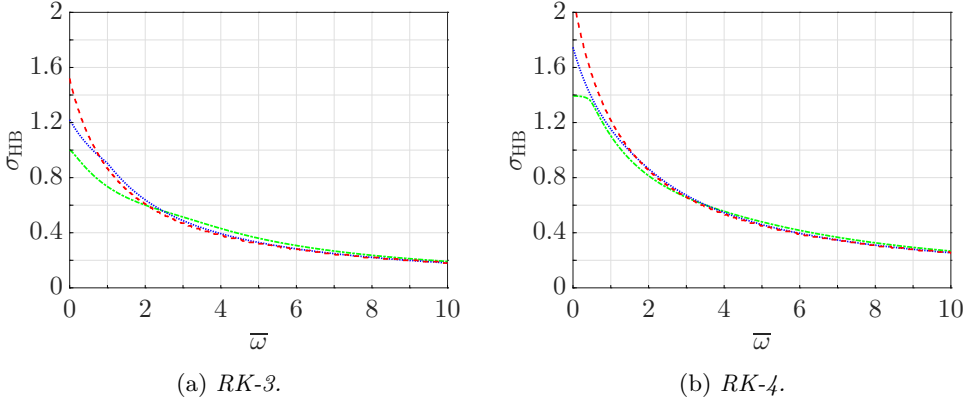


Figure 2.3: Variation of largest allowable CFL number that ensures stability with grid-reduced frequency for different combinations of spatial discretization (--- = FOU, ..... = TOU, --- = TOU-LD) and pseudo-time integration schemes.

## 2.4 Time Level Preconditioner

Stable pseudo-time integration of the Harmonic Balance equations may be obtained by scaling the time-step with which each frequency component in the solution is updated. To define this scaling, we note that there exists three waves, with corresponding wave speeds  $\lambda_1 < \lambda_2 < \lambda_3$ , for the one-dimensional case considered here. For a given grid size and frequency ( $\omega_n$ ), there also exists three grid reduced frequencies  $\bar{\omega}_{n,3} < \bar{\omega}_{n,2} < \bar{\omega}_{n,1}$  that correspond to these waves. In order to ensure stability, the time-step that is used to update each frequency component must then be chosen such that

$$\Delta\tau_n = \min_p(\Delta\tau_{n,p}) \quad (2.47)$$

Here,  $\Delta\tau_{n,p}$  is calculated as

$$\Delta\tau_{n,p} = \sigma_{HB}(\bar{\omega}_{n,p}) \frac{\Delta x}{|\lambda_p|} \quad (2.48)$$

The CFL number in the above equation is further obtained from Fig. 2.3. If this CFL number is scaled by the largest CFL number that ensures stability in a steady-state computation, the following is obtained

$$g(\bar{\omega}) = \frac{\sigma_{\text{HB}}(\bar{\omega})}{\sigma_{\text{Steady}}} \quad (2.49)$$

This ratio can be obtained by normalizing the plots in Fig. 2.3 by their values at  $\bar{\omega} = 0$ . The result of this is shown in Fig. 2.4. In this figure, the following function has also been plotted

$$g_a(\bar{\omega}) = \frac{1}{1 + \gamma|\bar{\omega}|}, \quad \gamma = 0.75 \quad (2.50)$$

Note that this function satisfies  $g_a(\bar{\omega}) \leq g(\bar{\omega})$  for all combinations of spatial discretization, pseudo-time integration scheme and grid reduced frequency. A conservative estimate of the pseudo-time-step in Eq. (2.48) may therefore be obtained as

$$\Delta\tau_{n,p} = \sigma_{\text{Steady}} g_a(\bar{\omega}_{n,p}) \frac{\Delta x}{|\lambda_p|} \quad (2.51)$$

This relation may now be combined with Eq. (2.47) to obtain

$$\Delta\tau_n = \sigma_{\text{Steady}} \min_p \left( \frac{1}{\frac{|\lambda_p|}{\Delta x} + \gamma|\omega_n|} \right), \quad \gamma = 0.75 \quad (2.52)$$

From this equation, it follows that the pseudo-time-step should be chosen based on the largest wave speed as

$$\Delta\tau_n = \frac{\sigma_{\text{Steady}}}{\frac{\max_p(|\lambda_p|)}{\Delta x} + \gamma|\omega_n|}, \quad \gamma = 0.75 \quad (2.53)$$

This expression may now be compared to the time-step that would be used in a steady-state computation

$$\Delta\tau_{\text{Steady}} = \sigma_{\text{Steady}} \frac{\Delta x}{\max_p(|\lambda_p|)} \quad (2.54)$$

The ratio between the time-step that should be used in the Harmonic Balance computation, and the one that should be used in a steady-state computation, therefore reads as follows

$$\frac{\Delta\tau_n}{\Delta\tau_{\text{Steady}}} = \frac{\sigma_{\text{Steady}}}{\sigma_{\text{Steady}} + \gamma|\omega_n|\Delta\tau_{\text{Steady}}}, \quad \gamma = 0.75 \quad (2.55)$$

Note that it is the actual frequency, and not the grid reduced frequency, that is used in the above equation.

A stable pseudo-time integration solver may now be obtained as follows. First, the residual resulting from the spatial+temporal discretization is computed for each cell in the mesh. Next, this residual is scaled by a local time-step obtained from Eq. (2.54). Note that the CFL number used in this equation should be selected to ensure that a



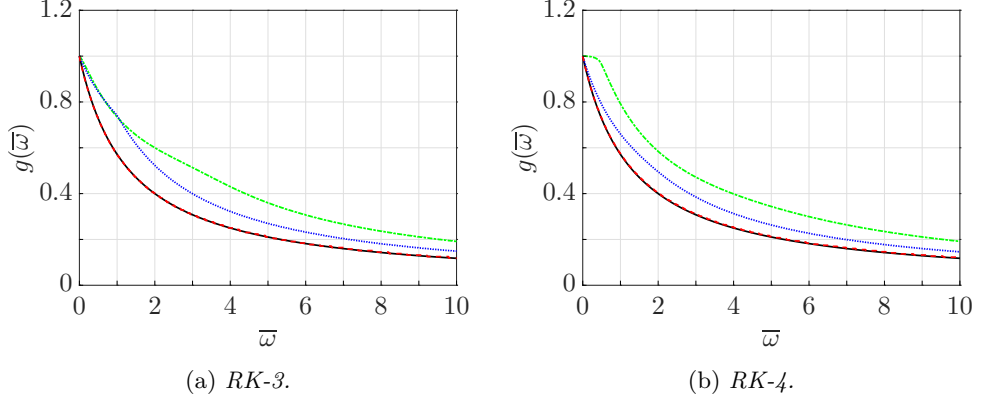


Figure 2.4: Plots of scaling function  $g(\bar{\omega})$  for different combinations of spatial discretization ( $\cdots$  = FOU,  $\cdots$  = TOU,  $---$  = TOU-LD,  $—$  =  $g_a(\bar{\omega})$ ) and pseudo-time integration schemes.

steady-state computation, not a Harmonic Balance computation, would converge. Before the next Runge-Kutta stage, the following preconditioning step is finally performed

$$(\Delta\tau R_{\text{HB}}(\mathbf{q}^*))_{\text{Prec}} = \mathbf{E}_{\Lambda}^{-1}(\mathbf{t}) \mathbf{G}_{\Lambda} \mathbf{E}_{\Lambda}(\mathbf{t}) (\Delta\tau_{\text{Steady}} R_{\text{HB}}(\mathbf{q}^*)) \quad (2.56)$$

Here,  $R_{\text{HB}}(\mathbf{q}^*)$  denotes the residual resulting from the spatial+temporal discretization, i.e. the left hand side of Eq. (2.12), and  $\mathbf{G}_{\Lambda} = G_{\Lambda} \otimes \mathbf{I}$ , where

$$G_{\Lambda} = \begin{bmatrix} \tilde{g}_a(0) & 0 & \cdots & \cdots & 0 \\ 0 & \tilde{g}_a(\omega_1) & 0 & \cdots & 0 \\ \vdots & 0 & \tilde{g}_a(\omega_2) & 0 & \cdots & 0 \\ & \vdots & 0 & \ddots & & 0 \\ & & \vdots & & & 0 \\ 0 & 0 & 0 & 0 & 0 & \tilde{g}_a(\omega_{-1}) \end{bmatrix} \quad (2.57)$$

Here,  $\tilde{g}_a(\omega_n)$  denotes the ratio between the stable Harmonic Balance time-step and the stable steady-state time-step, i.e., the right hand side of Eq. (2.55).

### 3 Boundary Conditions and Duct Modes

Numerical solutions to partial differential equations, such as the Navier-Stokes equations in fluid dynamics, are commonly computed on some finite domain. For a given mesh resolution and spatial discretization scheme, the size of this domain determines the number of degrees of freedom, which in turn will influence the computational cost necessary to obtain a solution. It is therefore highly desirable to limit the size of the domain as much as possible. When the flow inside a turbomachine is simulated, this is often achieved by including only one blade per row in the computational domain. Sometimes, the inlet and outlet ducts are also excluded from the computational domain by placing the inlet/outlet boundaries close to the blades.

A smaller computational domain requires more sophisticated boundary conditions. Otherwise, the position of the boundary may have a nonphysical influence on the solution. In this chapter, a set of boundary conditions that are specifically designed to limit this problem for turbomachinery simulations will be presented. The first boundary condition is a phase-shifted periodic boundary condition. This boundary condition can be used to reduce the computational domain to one blade per row. The second boundary condition is the exact, nonlocal, nonreflecting boundary condition for a single Fourier mode introduced by Giles [34, 33, 35] and Hall et al. [37]. The purpose of this boundary condition is to reduce reflections of waves that propagate across the inlet/outlet boundaries, and thereby reduce the sensitivity of the solution to the position of these boundaries.

Both the phase-shifted periodic boundary condition and the nonreflecting boundary condition presented in this work exploit the temporal and circumferential periodicity of the flow inside a turbomachine. This periodicity can be understood by considering the flow relative to one of the blade rows in Fig. 3.1. Let the rotational speed of this blade row be denoted  $\Omega_c$ , and that of the opposite blade row  $\Omega_o$ . Let further  $N_c$  and  $N_o$  denote the number of blades in the blade row we consider, and the opposite blade row, respectively. If  $\Omega_c \neq \Omega_o$ , the flow inside the blade row that we consider will repeat itself each time the opposite blade row is clocked in the same position as shown in Fig. 3.1. From this observation, we may conclude that the flow inside the blade row we consider is time-periodic, with an angular frequency equal to  $N_o(\Omega_o - \Omega_c)$ . This frequency is often referred to as the relative blade passing frequency since it depends on the relative rotation rate of the two blade rows. In addition to being time-periodic, the flow inside a turbomachine must be periodic in the circumferential direction with a period equal to  $2\pi$ . These observations allow us to express the flow relative to the considered blade row as follows

$$q_c(x, r, \theta_c, t) = \sum_n \sum_m \hat{q}_{n,m,c}(x, r) e^{i(\omega_{n,c}t - m\theta_c)} \quad (3.1)$$

In this expression,  $\theta_c$  is the angle relative to the blade row we consider and

$$\omega_{n,c} = nN_o(\Omega_o - \Omega_c) \quad (3.2)$$

is the  $n^{\text{th}}$  harmonic of the relative blade passing frequency. The vector  $q_c$  in Eq. (3.1) may further be chosen to contain either the primitive or conserved flow variables in cylindrical

coordinates. The choice depends on which boundary condition that is implemented, as will be explained in more detail later.

The second summation in Eq. (3.1) includes all  $m \in \mathbb{Z}$ . As it turns out, however, most of the terms in this summation are zero [101, 85]. This can be proven by first noting that the flow in a certain blade passage must be equal the flow in an adjacent blade passage at a later (or earlier) time instant. This spatial-temporal periodicity may be expressed as

$$q_c(x, r, \theta_c, t) = q_c\left(x, r, \theta_c + \frac{2\pi}{N_c}, t + \frac{2\pi}{N_c(\Omega_o - \Omega_c)}\right) \quad (3.3)$$

This relation may be combined with Eq. (3.1) to derive the following equation

$$\omega_{n,c} \frac{2\pi}{N_c(\Omega_o - \Omega_c)} - m \frac{2\pi}{N_c} = -2\pi k, \quad k \in \mathbb{Z} \quad (3.4)$$

Note that the minus sign on the right hand side in this equation was chosen for convenience. The permissible values of  $m$  may now be obtained by rearranging the above equation slightly

$$m_{n,k,c} = nN_o + kN_c \quad (3.5)$$

This condition was originally derived by Tyler and Sofrin [101] and shows that  $m$  in Eq. (3.1) can only take on values which are integer multiples of the blade counts. By applying this condition in Eq. (3.1), the following final expression for the flow relative to the considered blade row is obtained

$$q_c(x, r, \theta_c, t) = \sum_n \sum_k \hat{q}_{n,k,c}(x, r) e^{i(\omega_{n,c}t - m_{n,k,c}\theta_c)} \quad (3.6)$$

Note that this equation was derived without making any assumption about which one of the two blade rows in Fig. 3.1 that was considered, making it valid for both blade rows.

Equation (3.6) shows that the flow relative to each blade row consists of several circumferential modes, each one rotating with a certain frequency. Often, it is also of interest to know how these modes rotate in the absolute frame of reference. This can be easily achieved by utilizing the following relation between the absolute and relative circumferential coordinate

$$\theta_c = \theta - \Omega_c t \quad (3.7)$$

By inserting this relation into Eq. (3.6), the following is obtained

$$q_c(x, r, \theta, t) = \sum_n \sum_k \hat{q}_{n,k,c}(x, r) e^{i(\omega_{n,k,c}t - m_{n,k,c}\theta)} \quad (3.8)$$

Here,

$$\omega_{n,k,c} = nN_o\Omega_o + kN_c\Omega_c \quad (3.9)$$

is the frequency with which the spinning modes in Eq. (3.8) rotate in the absolute frame of reference.

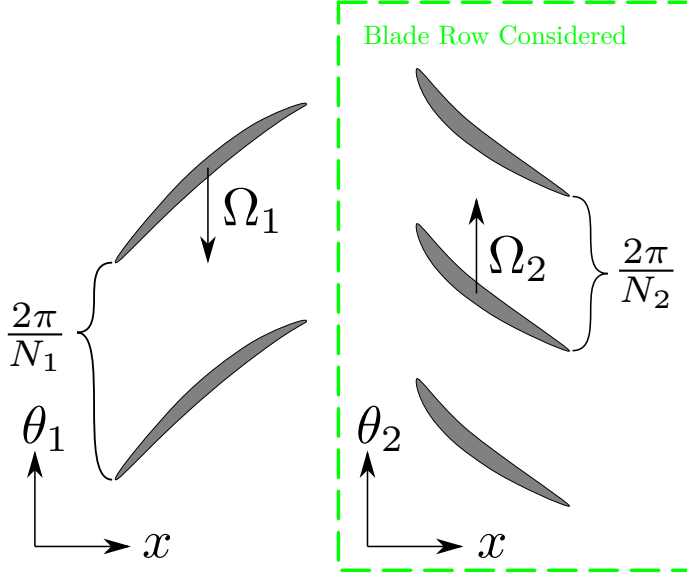


Figure 3.1: *Coordinate system and rotation direction of a single stage turbomachine.*

As mentioned earlier, this chapter mainly deals with boundary conditions that may be used to reduce the size of the computational domain, without a negative impact on the results. Truncating a computational domain does however imply that some information, such as how pressure waves generated by the rotating blades propagate inside the ducts, is lost. This information is clearly of great importance when the noise generated by the turbomachine is of interest. In these cases, the inlet/outlet ducts could be included in the simulation. Another option is to explicitly compute how the spinning modes defined in Eq. (3.8) propagate through the duct. Such a methodology will be presented in the last section of this chapter.

### 3.1 Phase Shifted Periodic Boundary Condition

A computational domain that only contains a single blade per row is shown in Fig. 3.2. As can be seen from this figure, new boundaries that correspond to the interface between two adjacent blade passages will be present when only a single blade per row is used in the computation. The purpose of the phase-shifted periodic boundary condition presented in this section is to couple the solution on these boundaries such that the space-time periodicity defined earlier is satisfied.

The first step in deriving the phase-shifted periodic boundary condition is to express the flow relative to one of the blade rows in Fig. 3.1 as

$$q_c(x, r, \theta_c, t) = \sum_n \hat{q}_{n,c}(x, r, \theta_c) e^{i\omega_{n,c}t} \quad (3.10)$$

This expression is similar to Eq. (3.6) except that the spatial dependence has been included in the Fourier coefficients. We now proceed by imposing the space time periodicity requirement defined in Eq. (3.3) on Eq. (3.10) to obtain

$$\sum_n \hat{q}_{n,c}(x, r, \theta_c) e^{i\omega_{n,c}t} = \sum_n \left[ \hat{q}_{n,c} \left( x, r, \theta_c + \frac{2\pi}{N_c} \right) e^{i\omega_{n,c} \frac{2\pi}{N_c(\Omega_o - \Omega_c)}} \right] e^{i\omega_{n,c}t} \quad (3.11)$$

The exponential functions in Eq. (3.11) are orthogonal with respect to the standard inner product on  $L^2([0, T_c])$ , where  $T_c = 2\pi/N_o|\Omega_o - \Omega_c|$  is the time period of the flow. From this, it follows that Eq. (3.11) can only hold if

$$\hat{q}_{n,c}(x, r, \theta_c) = \hat{q}_{n,c} \left( x, r, \theta_c + \frac{2\pi}{N_c} \right) e^{i\omega_{n,c} \frac{2\pi}{N_c(\Omega_o - \Omega_c)}} \quad (3.12)$$

Or equivalently, if

$$\hat{q}_{n,c}(x, r, \theta_c) e^{-i2\pi n \frac{N_o}{N_c}} = \hat{q}_{n,c} \left( x, r, \theta_c + \frac{2\pi}{N_c} \right) \quad (3.13)$$

This equation shows that the solution in an adjacent blade passage is related to the solution in the current blade passage by a phase shift. This fact will later be used to couple the solution at the periodic boundaries. Before this is done, however, Eq. (3.13) will be generalized slightly. To begin with, note that Eq. (3.3) must be valid independently on whether we move in the positive or negative  $\theta_c$  direction, as long as the sign of the time shift is adjusted accordingly. In addition to this, note that we may add any integer multiple of  $2\pi i$  to the exponent in the left-hand side of Eq. (3.13). Based on these two observations, Eq. (3.13) may be generalized as

$$\hat{q}_{n,c}(x, r, \theta_c) e^{-i\zeta 2\pi n \frac{N_o - N_c}{N_c}} = \hat{q}_{n,c} \left( x, r, \theta_c + \zeta \frac{2\pi}{N_c} \right) \quad (3.14)$$

Here,  $\zeta = \pm 1$  is used to define whether we move in the positive or negative  $\theta_c$  direction.

The coupling strategy employed in this work is based on a two-layer ghost cell technique. In this approach, ghost cell values outside each periodic boundary are computed by applying Eq. (3.14) to the interior solution on the other side (see Fig. 3.2). This can be done directly when the frequency-domain Harmonic Balance method is used. When the time-domain Harmonic Balance method on the other hand is employed, the solution must also be converted to and from the frequency-domain to apply Eq. (3.14). Once the ghost cell values have been computed, the same numerical scheme used in the interior can be used to update the solution on the periodic boundaries. The vector  $q_c$  should further be defined to contain the conserved variables.

The time to frequency domain transformation, phase shift, and frequency to time domain transformation steps necessary for the time-domain Harmonic Balance method may be conveniently grouped into a single matrix-vector multiplication as follows

$$\mathbf{q}_c^* \left( x, r, \theta_c + \zeta \frac{2\pi}{N_c} \right) = \mathbf{E}_\Lambda^{-1}(\mathbf{t}) \mathbf{P}_c \mathbf{E}_\Lambda(\mathbf{t}) \mathbf{q}_c^*(x, r, \theta_c) \quad (3.15)$$

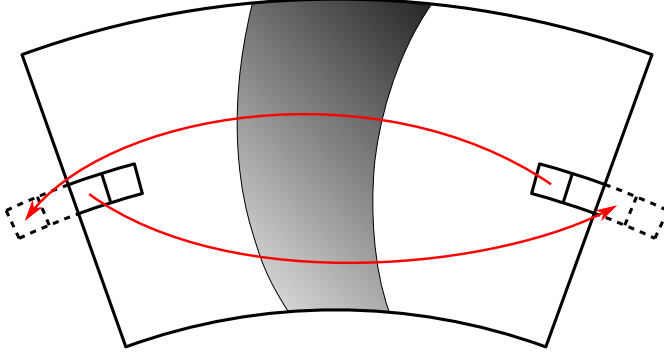


Figure 3.2: *Illustration showing how the phase shifted periodic boundary condition is implemented. The red arrows illustrate that the interior solution on one periodic boundary is phase shifted and inserted into the ghost cells outside the other periodic boundary.*

Here,  $\mathbf{E}_\Lambda(\mathbf{t})$  and  $\mathbf{E}_\Lambda^{-1}(\mathbf{t})$  represent the *standard*<sup>1</sup> discrete Fourier transform matrices introduced in chapter 2. The vector  $\mathbf{q}_c^*$  further consists of  $M$  sub-vectors, in which each sub-vector contains the conserved variables at the corresponding time instance. The matrix  $\mathbf{P}_c$  in Eq. (3.15) is finally defined as  $\mathbf{P}_c = P_c \otimes \mathbf{I}$ , where

$$P_c = \begin{bmatrix} 0 & 0 & \cdots & & 0 \\ 0 & e^{-i\zeta 2\pi \frac{N_o - N_c}{N_c}} & 0 & \cdots & 0 \\ \vdots & 0 & e^{-i\zeta 4\pi \frac{N_o - N_c}{N_c}} & 0 & \cdots & 0 \\ & \vdots & 0 & \ddots & & 0 \\ & & \vdots & & & 0 \\ 0 & 0 & 0 & 0 & 0 & e^{i\zeta 2\pi \frac{N_o - N_c}{N_c}} \end{bmatrix} \quad (3.16)$$

It should be noted that the exponent used in the above expression also can be written as

$$-i\zeta 2\pi n \frac{N_o - N_c}{N_c} = i\omega_{n,c} \Delta t_c \quad (3.17)$$

Here,  $\Delta t_c = \zeta \beta_c T_c / 2\pi$  and

$$\beta_c = -2\pi \operatorname{sgn}(\Omega_1 - \Omega_2) \frac{N_1 - N_2}{N_c} \quad (3.18)$$

is the phase shift between two adjacent blade passages used in [32].

---

<sup>1</sup>The standard discrete Fourier transform is here defined as the special case when the frequencies in  $\Lambda$  are harmonically related, and the time samples are chosen uniformly between 0 and  $T_c$ , where  $T_c$  is the time period of the flow.

## 3.2 Exact, Nonlocal, Nonreflecting Boundary Condition for a Single Fourier Mode

The boundary condition considered in this section is the exact, nonlocal, nonreflecting boundary condition for a single Fourier mode developed by Giles [34, 33, 35] and Hall et al. [37]. Giles originally constructed this boundary condition by considering the linearized Euler equations in two dimensions. Later, Saxer et al. [88] extended the boundary condition to work with three-dimensional simulations of axial flow turbomachines. This was done by assuming that the flow along stream surfaces with constant radius obeys the following form of the linearized Euler equations

$$\frac{\partial q'}{\partial t} + \bar{A} \frac{\partial q'}{\partial x} + \frac{1}{r} \bar{C} \frac{\partial q'}{\partial \theta} = 0 \quad (3.19)$$

In this equation,  $q' = q - \bar{q}$  is a vector that contains perturbations of the primitive flow variables with respect to a temporal+circumferential average state. The matrices  $\bar{A}$  and  $\bar{C}$  in Eq. (3.19) are further defined as

$$\bar{A} = \begin{bmatrix} \bar{v}_x & \bar{p} & 0 & 0 & 0 \\ 0 & \bar{v}_x & 0 & 0 & 1/\bar{\rho} \\ 0 & 0 & \bar{v}_x & 0 & 0 \\ 0 & 0 & 0 & \bar{v}_x & 0 \\ 0 & \gamma \bar{p} & 0 & 0 & \bar{v}_x \end{bmatrix} \quad \bar{C} = \begin{bmatrix} \bar{v}_\theta & 0 & 0 & \bar{p} & 0 \\ 0 & \bar{v}_\theta & 0 & 0 & 0 \\ 0 & 0 & \bar{v}_\theta & 0 & 0 \\ 0 & 0 & 0 & \bar{v}_\theta & 1/\bar{\rho} \\ 0 & 0 & 0 & \gamma \bar{p} & \bar{v}_\theta \end{bmatrix} \quad (3.20)$$

Note that for a calorically perfect ideal gas,  $\gamma \bar{p} = \bar{\rho} \bar{c}^2$ , where  $\bar{c}$  is the average speed of sound and  $\gamma$  the ratio of specific heats.

The boundary condition considered in this section is referred to as *exact* since it will be perfectly nonreflecting when Eq. (3.19) is satisfied at the boundary. Clearly, this is not the case when three dimensional, nonlinear, viscous flows are considered. Equation (3.19) can however provide a reasonable approximation of the flow provided that nonlinearities, spanwise variations, and viscous effects are not too dominant. More details on this are provided in Appendix A, where Eq. (3.19) is derived from the three dimensional, nonlinear Euler equations.

Boundary conditions that account for spanwise flow variations and/or viscous dissipation have also been developed [74, 75, 51]. These boundary conditions are generally more computationally expensive than the one considered in this section since they require the whole boundary to be included simultaneously in the analysis. Some more details regarding this will be provided in the section on duct modes, which are the building blocks for the aforementioned boundary conditions.

### 3.2.1 Modal Decomposition

The derivation of the nonreflecting boundary condition starts by making the variable substitution  $z = r\theta$  in Eq. (3.19) to obtain

$$\frac{\partial q'}{\partial t} + \bar{A} \frac{\partial q'}{\partial x} + \bar{C} \frac{\partial q'}{\partial z} = 0 \quad (3.21)$$

We proceed by looking for wave-like solutions to this equation on the following form [34, 89, 51]

$$q'(x, r, \theta, t) = \hat{q}(r) e^{i(\omega t - k_x x - k_z z)} \quad (3.22)$$

Here,  $k_x$  is the axial wavenumber of the wave and  $k_z z = m\theta$ , where  $k_z = m/r$  is the azimuthal wavenumber of the wave. By inserting this ansatz into Eq. (3.21), we obtain

$$(\omega - k_x \bar{A} - k_z \bar{C}) \hat{q}(r) = 0 \quad (3.23)$$

An eigenvalue problem for the axial wavenumber, with corresponding eigenvector  $\hat{q}(r)$ , may now be obtained by multiplying Eq. (3.23) from the left by  $\bar{A}^{-1}$

$$(\omega \bar{A}^{-1} - k_z \bar{A}^{-1} \bar{C} - k_x I) \hat{q}(r) = 0 \quad (3.24)$$

Note that this relation is only valid if  $\bar{A}$  is invertible, which holds true if  $\det(\bar{A}) = \bar{v}_x^3 (\bar{c}^2 - \bar{v}_x^2) \neq 0$ . To ensure this, we assume that the mean axial velocity is nonzero and subsonic. It can also be noted that the eigenvalue problem in Eq. (3.24) is not well defined if  $\omega = k_z = 0$ . This special case does however not pose a problem since it corresponds to the mean flow, and therefore is treated separately when the boundary condition is imposed.

The eigenvalue problem presented in Eq. (3.24) can be solved for a given combination of frequency and azimuthal wavenumber to obtain five eigenvalue/eigenvector pairs  $(k_{x,j}, \hat{q}_j)$ . These pairs may then be substituted back into Eq. (3.22) to obtain all the waves that are allowed to exist in the flow according to Eq. (3.21). Before this is done, however, it should be noted that eigenvectors are only defined up to a constant. If the geometric multiplicity of an eigenvalue further is greater than one, then any linear combination of two corresponding eigenvectors is also an eigenvector. As a result of this non-uniqueness, care must be taken when the eigenvectors are defined. In particular, it is advantageous to ensure that the eigenvectors have a physically relevant meaning in the sense that they correspond to entropy, vorticity, and acoustic waves [33]. It is also important from a numerical point of view to choose the eigenvectors in such a way that they never contain a division by zero or become a null vector for some combination of  $\bar{q}$ ,  $\omega$  and  $k_z$ . The eigenvectors selected in this work satisfy all the aforementioned conditions.

## Entropy and Vorticity Waves

The first eigenvalue of the matrix  $(\omega \bar{A}^{-1} - k_z \bar{A}^{-1} \bar{C})$  has an algebraic multiplicity equal to three and reads as follows

$$k_{x,1} = k_{x,2} = k_{x,3} = \frac{\omega - k_z \bar{v}_\theta}{\bar{v}_x} \quad (3.25)$$



As it turns out, the geometric multiplicity of this eigenvalue is also three. The eigenvectors corresponding to the eigenvalue defined in Eq. (3.25) have been selected as

$$\hat{q}_1 = \begin{bmatrix} \bar{\rho} \\ 0 \\ 0 \\ 0 \\ 0 \end{bmatrix} \quad \hat{q}_2 = \begin{bmatrix} 0 \\ 0 \\ \bar{c} \\ 0 \\ 0 \end{bmatrix} \quad \hat{q}_3 = \begin{bmatrix} 0 \\ -\bar{c}k_z \\ 0 \\ \bar{c}k_{x,1} \\ 0 \end{bmatrix} \quad (3.26)$$

The structure of these eigenvectors shows that they respectively correspond to an entropy wave, radial vorticity wave, and axial-circumferential vorticity wave. It can also be noted that none of these vectors will become a null vector or contain a division by zero under the stated assumptions.

The direction of propagation of the waves defined by the first three eigenvalue/eigenvector pairs may be determined from the group velocity since both the frequency and axial/circumferential wavenumbers are real-valued. The relevant component of the group velocity in our case is the axial one, which may be computed as [33]

$$v_{g,x,j} = \frac{\partial \omega}{\partial k_{x,j}} = \left( \frac{\partial k_{x,j}}{\partial \omega} \right)^{-1} = \bar{v}_x, \quad j = 1, 2, 3 \quad (3.27)$$

This result shows that the entropy and vorticity waves are convected downstream with the mean flow, as should be expected.

### Acoustic Waves

The remaining two eigenvalues of  $(\omega \bar{A}^{-1} - k_z \bar{A}^{-1} \bar{C})$  may be written as

$$k_{x,4} = \frac{-\bar{v}_x(\omega - k_z \bar{v}_\theta) + \bar{c}\sqrt{\Lambda}}{\bar{c}^2 - \bar{v}_x^2} \quad (3.28)$$

$$k_{x,5} = \frac{-\bar{v}_x(\omega - k_z \bar{v}_\theta) - \bar{c}\sqrt{\Lambda}}{\bar{c}^2 - \bar{v}_x^2}$$

where

$$\Lambda = (\omega - k_z \bar{v}_\theta)^2 - k_z^2(\bar{c}^2 - \bar{v}_x^2) \quad (3.29)$$

The eigenvectors corresponding to these eigenvalues have been selected as

$$\hat{q}_4 = \begin{bmatrix} \bar{\rho} \\ \frac{-\bar{c}^2 k_{x,4}}{\bar{v}_x k_{x,4} - \bar{v}_x k_{x,1}} \\ 0 \\ \frac{-\bar{c}^2 k_z}{\bar{v}_x k_{x,4} - \bar{v}_x k_{x,1}} \\ \frac{\bar{\rho}}{\bar{c}^2} \end{bmatrix} \quad \hat{q}_5 = \begin{bmatrix} \bar{\rho} \\ \frac{-\bar{c}^2 k_{x,5}}{\bar{v}_x k_{x,5} - \bar{v}_x k_{x,1}} \\ 0 \\ \frac{-\bar{c}^2 k_z}{\bar{v}_x k_{x,5} - \bar{v}_x k_{x,1}} \\ \frac{\bar{\rho}}{\bar{c}^2} \end{bmatrix} \quad (3.30)$$

The structure of these eigenvectors shows that the last two eigenvalue/eigenvector pairs define two acoustic waves.

The direction of propagation of the acoustic waves is determined by first considering  $\Lambda$  in Eq. (3.29). If  $\Lambda > 0$ , the group velocity can be used to determine the direction of propagation since the eigenvalues in Eq. (3.28) then become real-valued. The axial component of the group velocity for the acoustic waves reads as follows

$$\begin{aligned} v_{g,x,4} &= -\frac{\bar{c}^2 - \bar{v}_x^2}{\bar{v}_x - \frac{\bar{c}(\omega - k_z \bar{v}_\theta)}{\sqrt{\Lambda}}} \\ v_{g,x,5} &= -\frac{\bar{c}^2 - \bar{v}_x^2}{\bar{v}_x + \frac{\bar{c}(\omega - k_z \bar{v}_\theta)}{\sqrt{\Lambda}}} \end{aligned} \quad (3.31)$$

If the mean axial velocity is subsonic and  $\Lambda > 0$  it is possible to show that if  $v_{g,x,4} > 0$ , then  $v_{g,x,5} < 0$  and vice versa. Under these conditions, one acoustic wave will therefore propagate upstream and the other one downstream. If on the other hand  $\Lambda < 0$ , Eq. (3.28) gives two complex eigenvalues, one with positive and one with negative imaginary part. If these eigenvalues are inserted into Eq. (3.22) it is found that a negative imaginary part corresponds to a wave that is exponentially decaying in the positive axial direction, whereas a positive imaginary part gives exponential decay in the negative axial direction. In this work, the direction of propagation of an acoustic wave with a complex axial wavenumber is taken to be the direction in which it decays. This definition has also been adopted by other authors [28, 74]. As a consequence of this definition, acoustic waves with a complex axial wavenumber are interpreted as decaying from their respective point of origin, which motivates the commonly used abbreviation "cut-off". Acoustic waves associated with a real-valued axial wavenumber will on the other hand be referred to as "cut-on", since they propagate without decaying.

As will be shown later, the construction of the nonreflecting boundary condition presented in this work requires that there exists 5 linearly independent eigenvectors, for which the direction of propagation of the associated waves is known. Unfortunately, the special case when  $\Lambda = 0$  violates this condition. This special case is known as acoustic resonance [28], since it gives rise to a single standing wave that does not propagate either upstream or downstream. To ensure that acoustic resonance does not occur, the regularization proposed by Frey et al. [28] has been adopted. This regularization will be outlined next.

### Regularization to Prevent Acoustic Resonance

Frey et al. [28] show that acoustic resonance can be avoided by including an additional damping term in Eq. (3.21)

$$\frac{\partial q'}{\partial t} + \bar{A} \frac{\partial q'}{\partial x} + \bar{C} \frac{\partial q'}{\partial z} + \varepsilon q' = 0 \quad (3.32)$$

Here,  $\varepsilon > 0$  is a real value that sets the amount of damping. By following the same procedure as before, we obtain the following eigenvalue problem from Eq. (3.32)

$$\left( (\omega - i\varepsilon) \bar{A}^{-1} - k_z \bar{A}^{-1} \bar{C} - k_x I \right) \hat{q}(r) = 0 \quad (3.33)$$

This eigenvalue problem can also be obtained by replacing  $\omega$  in Eq. (3.24) with the following, modified frequency

$$\tilde{\omega} = \omega - i\varepsilon \quad (3.34)$$

This means that we can obtain solutions to Eq. (3.33) by substituting  $\omega$  with  $\tilde{\omega}$  in the solutions to Eq. (3.24). This will in turn prevent acoustic resonance by ensuring that  $\Lambda$  in Eq. (3.29) always becomes a non-zero, complex number.

When the frequency defined in Eq. (3.34) is used the acoustic waves will always be cut-off. This raises a question regarding how the direction of propagation of an acoustic wave that is cut-on in the original analysis should be determined when the damping term is included. The answer to this question is also provided by Frey et al. [28], who show that the direction of propagation of a wave that is cut-on in the original analysis, will be the same as the direction of damping of when the modified frequency in Eq. (3.34) is used. This elegant result allows us to treat all acoustic waves consistently when the modified frequency is being employed. That is, the direction of propagation of the acoustic waves can always be determined from the imaginary part of  $k_{x,4}, k_{x,5}$  when the modification of  $\omega$  in Eq. (3.34) is employed. It should also be pointed out that the modification of  $\omega$  only applies when the eigenvalues/eigenvectors are being computed, not for calculating the temporal evolution of the wave in Eq. (3.22). The group velocity is also still used for computing the direction of propagation of the convected waves.

### 3.2.2 Nonreflecting Condition

The foregoing analysis showed that there exist five waves that satisfy Eq. (3.21) for a given frequency/azimuthal wavenumber pair. This implies that the most general form of a flow perturbation with a certain frequency and azimuthal wavenumber may be written as

$$q'(x, r, \theta, t) = \sum_{j=1}^5 \alpha_j(r) \hat{q}_j e^{i(\omega t - k_{x,j} x - k_z z)} \quad (3.35)$$

Here,  $\alpha_j(r)$  is a complex number that defines the amplitude and phase of the  $j^{\text{th}}$  wave. For convenience, we may absorb the axial dependence of the  $j^{\text{th}}$  wave into this constant to obtain the following

$$q'(x, r, \theta, t) = \sum_{j=1}^5 \alpha_j^*(x, r) \hat{q}_j e^{i(\omega t - k_z z)} \quad (3.36)$$

This equation may also be written in matrix form as

$$q'(x, r, \theta, t) = T \alpha^*(x, r) e^{i(\omega t - k_z z)} \quad (3.37)$$

Here,  $\alpha^*(x, r)$  is a  $5 \times 1$  vector that contains the modal amplitudes  $\alpha_j^*(x, r)$ , and  $T$  is a  $5 \times 5$  matrix that contains the eigenvectors  $\hat{q}_j$  structured into its columns

$$T = \begin{bmatrix} \bar{\rho} & 0 & 0 & \frac{-\bar{\rho}}{\bar{v}_x k_{x,4} - \bar{v}_x k_{x,1}} & \frac{-\bar{\rho}}{\bar{v}_x k_{x,5} - \bar{v}_x k_{x,1}} \\ 0 & 0 & -\bar{c}k_z & 0 & 0 \\ 0 & \bar{c} & 0 & 0 & 0 \\ 0 & 0 & \bar{c}k_{x,1} & \frac{-\bar{c}^2 k_z}{\bar{v}_x k_{x,4} - \bar{v}_x k_{x,1}} & \frac{-\bar{c}^2 k_z}{\bar{v}_x k_{x,5} - \bar{v}_x k_{x,1}} \\ 0 & 0 & 0 & \frac{\bar{\rho}}{\bar{c}^2} & \frac{\bar{\rho}}{\bar{c}^2} \end{bmatrix} \quad (3.38)$$

It should be noted that these eigenvectors have also been used by Kersken et al. [51].

Let us now turn back to Eq. (3.8) and note that, since  $k_z z = m\theta$  and  $z = r\theta$ , each Fourier mode in this series expansion represents a flow perturbation with a known frequency and azimuthal wavenumber. Therefore, if we choose  $k_z = m_{n,k,c}/r$  and  $\omega = \omega_{n,k,c}$  in Eq. (3.37), we may equate this expression to the corresponding Fourier mode in Eq. (3.8) to obtain

$$\hat{q}_{n,k,c}(x, r) = T\alpha^*(x, r) \quad (3.39)$$

Equation (3.39) can be used to calculate  $\alpha^*(x, r)$  from the Fourier coefficient  $\hat{q}_{n,k,c}(x, r)$  provided that  $T$  has full rank. It is a fairly simple task to show that  $T$  satisfies this condition under the previously stated assumptions, provided that  $\Lambda \neq 0$  and that the modified frequency defined in Eq. (3.34) is not employed. A similar proof for the case when Eq. (3.34) is used to prevent acoustic resonance has however not been completed due to the additional complexity that a complex-valued frequency adds to the algebra. If it is assumed that  $T$  indeed is invertible under all circumstances when the modified frequency is used, Eq. (3.39) may be rewritten as

$$T^{-1}\hat{q}_{n,k,c}(x, r) = \alpha^*(x, r) \quad (3.40)$$

Here,  $T^{-1}$  denotes the inverse of  $T$ . It reads as follows

$$T^{-1} = \begin{bmatrix} \frac{1}{\bar{\rho}} & 0 & 0 & 0 & \frac{-1}{\bar{\rho} \bar{c}^2} \\ 0 & 0 & \frac{1}{\bar{c}} & 0 & 0 \\ 0 & \frac{-k_z}{\bar{c}(k_{x,1}^2 + k_z^2)} & 0 & \frac{k_{x,1}}{\bar{c}(k_{x,1}^2 + k_z^2)} & \frac{-k_z}{\bar{\rho} \bar{c} \bar{v}_x (k_{x,1}^2 + k_z^2)} \\ 0 & \frac{-\bar{v}_x (k_{x,4} k_{x,1} - k_{x,1}^2 k_z)}{2\bar{c}^2 (k_{x,4} k_{x,1} + k_z^2)} & 0 & \frac{-\bar{v}_x (k_{x,4} k_z - k_{x,1} k_z)}{2\bar{c}^2 (k_{x,4} k_{x,1} + k_z^2)} & \frac{1}{2\bar{\rho} \bar{c}^2} \\ 0 & \frac{-\bar{v}_x (k_{x,5} k_{x,1} - k_{x,1}^2 k_z)}{2\bar{c}^2 (k_{x,5} k_{x,1} + k_z^2)} & 0 & \frac{-\bar{v}_x (k_{x,5} k_z - k_{x,1} k_z)}{2\bar{c}^2 (k_{x,5} k_{x,1} + k_z^2)} & \frac{1}{2\bar{\rho} \bar{c}^2} \end{bmatrix} \quad (3.41)$$

The rows in this matrix contain the left eigenvectors to  $(\omega \bar{A}^{-1} - k_z \bar{A}^{-1} \bar{C})$ .

Equation (3.40) shows that the left eigenvectors measure the amplitude of each wave that constitutes  $\hat{q}_{n,k,c}(x, r)$ . At a boundary, we want the amplitude of the incoming waves to be zero. This may be stated as

$$T_{\text{inc}}^{-1} \hat{q}_{n,k,c}(x, r) = 0 \quad (3.42)$$

Here,  $T_{\text{inc}}^{-1}$  contains the rows in  $T^{-1}$  that correspond to incoming waves.

It is also possible to imagine that the foregoing analysis is used to couple the solution on both sides of a blade row interface. In this case, we want the amplitude of the incoming waves on one side of the interface to match the amplitude of the corresponding waves on the other side of the interface. This may be expressed as

$$T_{\text{inc}}^{-1} \hat{q}_{n,k,c}(x, r) = T_{\text{inc}}^{-1} \hat{q}_{l,p,o}(x, r) \quad (3.43)$$

Here,  $\hat{q}_{l,p,o}(x, r)$  should be selected to satisfy the following conditions

$$\begin{aligned} \omega_{n,k,c} &= \omega_{l,p,o} \\ m_{n,k,c} &= m_{l,p,o} \end{aligned} \quad (3.44)$$

If  $\Omega_c \neq \Omega_o$ , this system of equations can be used to show that  $l = k$  and  $p = n$ , or in other words, that  $\hat{q}_{n,k,c}(x, r)$  corresponds to  $\hat{q}_{k,n,o}(x, r)$ . It should also be noted that once Eq. (3.43) is satisfied on both sides of an interface,  $\hat{q}_{n,k,c}(x, r) = \hat{q}_{l,p,o}(x, r)$  [27].

### 3.2.3 Implementation Strategy

Equations (3.42) and (3.43) are an underdetermined system of equations that do not possess unique solutions. Physically, this means that there can exist several different flow fields that do not contain any incoming waves. Unfortunately, this also means that there exists an infinite amount of ways in which Eq. (3.42) or Eq. (3.43) can be enforced during an iterative solution process. As noted by Giles [33], the chosen implementation strategy can have a large impact on the numerical stability of the solver. Therefore, it makes sense to choose an implementation strategy that, loosely speaking, maximizes stability for the particular solver employed. Finding such an implementation strategy would likely require a rigorous stability analysis and has not been attempted in this work. Instead, two different implementation strategies described in the literature have been implemented and tested.

Both strategies considered in this work require that the Fourier coefficients in Eq. (3.8) are known. These Fourier coefficients can be calculated by utilizing the fact that the Fourier harmonics in Eq. (3.6) (which contains the same Fourier coefficients as Eq. (3.8)) are orthogonal with respect to the standard inner product on  $L^2([0, T_c] \times [0, 2\pi/N_c])$ . Numerically,  $\hat{q}_{n,k,c}(x, r)$  is calculated by first calculating  $\hat{q}_{n,c}(x, r, \theta_c)$  as the discrete Fourier transform of  $q_c(x, r, \theta_c, t)$ . After this, the following integral is approximated by the rectangle rule

$$\hat{q}_{n,k,c}(x, r) = \frac{N_c}{2\pi} \int_0^{2\pi/N_c} \hat{q}_{n,c}(x, r, \theta_c) e^{im_{n,k,c}\theta_c} d\theta_c \quad (3.45)$$

Note that  $q_c(x, r, \theta_c, t)$  should be converted to cylindrical coordinates and the absolute frame of reference before the Fourier coefficients are calculated. It should also be noted that the aforementioned steps make the boundary condition non-local in both space and time. This may seem like a disadvantage at first. As shown by Engquist and Majda [16], however, nonreflecting boundary conditions for hyperbolic problems must be non-local to be exact.

Once all Fourier coefficients have been calculated, they can be used to compute a new set of Fourier coefficients  $\hat{q}_{n,k,c}^{\text{nrbc}}(x, r)$  that satisfy Eq. (3.42) for a boundary, or Eq. (3.43) for an interface. These Fourier coefficients may then be combined with the specified mean flow to obtain a new boundary state for the next solver iteration. Computing the new set of Fourier coefficients may however become computationally expensive if many terms are included in Eq. (3.8). Wukie, Orkwis, Lindblad, and Andersson [106] avoid this problem by limiting the number of terms in Eq. (3.8), and then apply a simpler nonreflecting boundary condition based on characteristic variables to all flow perturbations corresponding to unresolved Fourier coefficients. This approach may be written as follows

$$q_c^{\text{nrbc}}(x, r, \theta_c, t) = \bar{q}^{\text{bc}} + \sum_{n \neq 0} \sum_{k \neq 0} \hat{q}_{n,k,c}^{\text{nrbc}}(x, r) e^{i(\omega_{n,c}t - m_{n,k,c}\theta_c)} + T_{1\text{D},\text{out}} T_{1\text{D},\text{out}}^{-1} \left( q'_c(x, r, \theta_c, t) - \sum_{n \neq 0} \sum_{k \neq 0} \hat{q}_{n,k,c}(x, r) e^{i(\omega_{n,c}t - m_{n,k,c}\theta_c)} \right) \quad (3.46)$$

The matrices  $T_{1\text{D}}, T_{1\text{D}}^{-1}$  in this equation represent the mapping between the characteristic and the primitive variables and are defined in Appendix A. It can now be noted that  $\hat{q}_{n,k,c}(x, r)$  should correspond to  $\hat{q}_{n,k,c}^{\text{nrbc}}(x, r)$  in the converged limit. It is thus permissible to substitute  $\hat{q}_{n,k,c}(x, r)$  for  $\hat{q}_{n,k,c}^{\text{nrbc}}(x, r)$  in Eq. (3.46) to obtain the following

$$q_c^{\text{nrbc}}(x, r, \theta_c, t) = \bar{q}^{\text{bc}} + T_{1\text{D},\text{out}} T_{1\text{D},\text{out}}^{-1} q'_c(x, r, \theta_c, t) + T_{1\text{D},\text{inc}} T_{1\text{D},\text{inc}}^{-1} \left( \sum_{n \neq 0} \sum_{k \neq 0} \hat{q}_{n,k,c}^{\text{nrbc}}(x, r) e^{i(\omega_{n,c}t - m_{n,k,c}\theta_c)} \right) \quad (3.47)$$

This equation has been used to enforce the nonreflecting state at the boundary in both implementation strategies. The benefit of using this equation is that it treats all unresolved Fourier coefficients using a standard nonreflecting boundary condition based on characteristic variables and that it reduces to a standard nonreflecting boundary condition based on characteristic variables when no Fourier coefficients are included in the analysis.

## Direct Approach

In the first implementation strategy, a new set of Fourier coefficients that satisfy Eq. (3.43) is computed as follows

$$\hat{q}_{n,k,c}^{\text{nrbc}}(x, r) = T_{\text{out}} T_{\text{out}}^{-1} \hat{q}_{n,k,c}(x, r) + T_{\text{inc}} T_{\text{inc}}^{-1} \hat{q}_{l,p,o}(x, r) \quad (3.48)$$

This approach is thus based on directly splitting the solution at the boundary into incoming and outgoing waves, and then select the outgoing waves from the interior and the incoming waves from the other side of the interface. Note that, in cases when the nonreflecting boundary state should satisfy Eq. (3.42),  $\hat{q}_{l,p,o}(x, r)$  is simply set to 0 in the above equation.

To favor convergence, under-relaxation has been used to update the nonreflecting boundary state. This is easily achieved by modifying Eq. (3.48) as follows

$$\hat{q}_{n,k,c}^{\text{nrbc}}(x, r) = \sigma \left( T_{\text{out}} T_{\text{out}}^{-1} \hat{q}_{n,k,c}(x, r) + T_{\text{inc}} T_{\text{inc}}^{-1} \hat{q}_{l,p,o}(x, r) \right) + (1 - \sigma) \hat{q}_{n,k,c}^{\text{nrbc,prev}}(x, r) \quad (3.49)$$

Here,  $\hat{q}_{n,k,c}^{\text{nrbc,prev}}$  is the nonreflecting state computed in the previous iteration and  $\sigma \leq 1$  is an under-relaxation factor.

Although under-relaxation might provide improved stability, it does not guarantee that the solver converges. In particular, the direct implementation approach outlined above has been reported to be numerically unstable when used in conjunction with a pseudo-time integration solver [29, 51, 67]. For this reason, it was decided to implement the next approach, which has been reported to be more stable [51].

## Reformulation using Characteristic Variables

The next implementation strategy that has been considered was originally proposed by Giles [33] and is based on reformulating Eq. (3.42) in terms of the characteristic variables. Later, Kersken et al. [51] generalized this approach to Eq. (3.43). In this work, the generalization of Kersken et al. [51] has been adopted to ensure that the implementation can be used for both boundaries and blade row interfaces.

The derivation of the second implementation strategy starts by expressing  $\hat{q}_{n,k,c}(x, r)$  in terms of the corresponding characteristic variables

$$\hat{q}_{n,k,c}(x, r) = T_{1D} \hat{c}_{n,k,c}(x, r) \quad (3.50)$$

The characteristic variables in this equation can be obtained in either of two ways. The first option is to first compute  $\hat{q}_{n,k,c}(x, t)$ , and then invert Eq. (3.50) to obtain  $\hat{c}_{n,k,c}(x, r)$ . Alternatively,  $q_c(x, r, \theta_c, t)$  can first be converted to characteristic variables, and then integrated in space and time to obtain  $\hat{c}_{n,k,c}(x, r)$ . The reason why both these approaches work is that  $T_{1D}$  is defined in terms of the time-azimuthal average  $\bar{q}$ , and therefore commutes with integration in  $t$  and  $\theta_c$ .

We now proceed by substituting Eq. (3.50) into Eq. (3.43) to obtain

$$T_{\text{inc}}^{-1} T_{1D} \hat{c}_{n,k,c} = T_{\text{inc}}^{-1} \hat{q}_{l,p,o} \quad (3.51)$$

Note that the spatial dependence of the Fourier coefficients was omitted here for brevity. The above equation may be further rewritten by splitting the left-hand side into incoming and outgoing characteristic variables, and then rearrange it as follows

$$T_{\text{inc}}^{-1} T_{1D, \text{inc}} \hat{c}_{n,k,c, \text{inc}} = T_{\text{inc}}^{-1} (\hat{q}_{l,p,o} - T_{1D, \text{out}} \hat{c}_{n,k,c, \text{out}}) \quad (3.52)$$

From this equation, we can obtain a relation that expresses the incoming characteristic variables as a function of the outgoing ones as

$$\hat{c}_{n,k,c, \text{inc}} = (T_{\text{inc}}^{-1} T_{1D, \text{inc}})^{-1} T_{\text{inc}}^{-1} (\hat{q}_{l,p,o} - T_{1D, \text{out}} \hat{c}_{n,k,c, \text{out}}) \quad (3.53)$$

This equation may be used to compute a new set of incoming characteristic variables as a function of the outgoing ones. A new set of characteristic variables that satisfy Eq. (3.51) is then obtained by combining the incoming characteristic variables obtained from Eq. (3.53) with the outgoing characteristic variables computed in the current iteration. This new set of characteristic variables may finally be used to compute a set of Fourier coefficients that satisfy Eq. (3.43) using Eq. (3.50).

Although the aforementioned steps give a Fourier coefficient that satisfies Eq. (3.43), it is often favorable from a stability point of view to relax the update of the incoming characteristic variables obtained from Eq. (3.53) [51]. This can be done by first computing the difference between the incoming characteristic variables used in the previous iteration, here denoted  $\hat{c}_{n,k,c}^{\text{nrbc,prev}}$ , and the new incoming characteristic variables as

$$\Delta \hat{c}_{n,k,c,\text{inc}}^{\text{nrbc}} = (T_{\text{inc}}^{-1} T_{1\text{D},\text{inc}})^{-1} T_{\text{inc}}^{-1} \left( \hat{q}_{l,p,o} - T_{1\text{D},\text{out}} \hat{c}_{n,k,c,\text{out}} - T_{1\text{D},\text{inc}} \hat{c}_{n,k,c,\text{inc}}^{\text{nrbc,prev}} \right) \quad (3.54)$$

From this, the relaxed update of the nonreflecting boundary state may be computed as

$$\hat{q}_{n,k,c}^{\text{nrbc}} = T_{1\text{D},\text{inc}} \left( \hat{c}_{n,k,c,\text{inc}}^{\text{nrbc,prev}} + \sigma \Delta \hat{c}_{n,k,c,\text{inc}} \right) + T_{1\text{D},\text{out}} \hat{c}_{n,k,c,\text{out}} \quad (3.55)$$

Here,  $\sigma \leq 1$  is an under-relaxation factor.

If we substitute Eq. (3.55) into Eq. (3.47), the following is obtained

$$\begin{aligned} q_c^{\text{nrbc}}(x, r, \theta_c, t) = & \bar{q}^{\text{bc}} + T_{1\text{D},\text{out}} T_{1\text{D},\text{out}}^{-1} q_c'(x, r, \theta_c, t) \\ & + T_{1\text{D},\text{inc}} \left( \sum_{n \neq 0} \sum_{k \neq 0} \left( \hat{c}_{n,k,c,\text{inc}}^{\text{nrbc,prev}} + \sigma \Delta \hat{c}_{n,k,c,\text{inc}} \right) e^{i(\omega_{n,c} t - m_{n,k,c} \theta_c)} \right) \end{aligned} \quad (3.56)$$

It is straightforward to prove that the boundary state defined by the above expression will satisfy Eq. (3.43) for all Fourier coefficients included in Eq. (3.8) when  $\sigma = 1$ . Higher order perturbations will further be treated with a standard nonreflecting boundary condition based on characteristic variables.

## Application to a Cell Centered Finite Volume Solver

Both approaches for enforcing Eq. (3.43) have been implemented into the G3D::Flow solver. G3D::Flow is a cell-centered finite-volume solver, meaning that the solution is not directly available *at* the boundary. Instead, the solution at the boundary must be calculated by extrapolating the interior solution, before calculating the nonreflecting boundary state. The approach taken in this work is to first calculate  $\hat{q}_{n,k,c}$  in two cell layers inside the boundary using Eq. (3.45), and then use linear extrapolation to obtain the Fourier coefficients *at* the boundary.

Extrapolation must also be employed when Eq. (3.47) (or Eq. (3.56)) is used to compute a nonreflecting state at the boundary. The reason for this is that  $q_c'(x, r, \theta_c, t)$  is unknown at the boundary. These values are here estimated by employing linear extrapolation of the primitive flow variables. Ideally, the face values obtained from this extrapolation



should also be used to calculate  $\hat{q}_{n,k,c}$ . The reason why the Fourier coefficients were first calculated, and then extrapolated, is that a different implementation strategy than the ones covered in this chapter was used in early implementations of the nonreflecting boundary condition.

The nonreflecting boundary state obtained from Eq. (3.47) (or Eq. (3.56)) is used to directly calculate the flux across all boundary faces. Alternatively, the flux across the boundary could be obtained by first populating ghost cell values, and then utilize the existing flux routines in G3D::Flow at the boundary. This strategy is however not favorable, since the flux at the face is a complicated function of the surrounding cell values. As such, great care must be taken to ensure that the ghost cell values, combined with the interior cell values, give the correct flux at the boundary. This complication is completely avoided by directly calculating the flux from the nonreflecting boundary state.

### Selecting Frame of Reference

It is important to note that all computations for the nonreflecting boundary condition are performed in cylindrical coordinates and the absolute frame of reference. This means that all flow variables, including both the averages and the perturbations, in the equations above are assumed to be in cylindrical coordinates and the absolute frame of reference. The frequency and nodal diameter are further calculated from Eq. (3.9) and Eq. (3.5), respectively.

The absolute frame of reference was mainly chosen to facilitate the implementation of the nonreflecting condition for blade row interfaces. It should however be emphasized that the nonreflecting analysis presented in this work would give equivalent results if the relative blade passing frequency (Eq. (3.2)) and the relative tangential velocity would have been used. This is because both the factor  $(\tilde{\omega} - k_z \bar{v}_\theta)$ , and all Fourier coefficients obtained from Eq. (3.45) except the zeroth one, are independent on the frame of reference.

### Differentiating between Incoming and Outgoing Waves

In section 3.2.1, it was shown that the entropy and vorticity waves are convected with the mean flow. This means that for an inlet, these waves are incoming, whereas for an outlet, they are outgoing. In section 3.2.1, it was also shown that, for an axially subsonic flow, one acoustic wave propagates upstream, and one downstream. It is however not known in advance which one that, e.g., propagates upstream. To determine this, the direction of propagation of each acoustic wave must be calculated. When the regularization proposed by Frey et al. [28] is used, this is done by checking the sign of  $\text{Im}(k_{x,4})$  and  $\text{Im}(k_{x,5})$ . In this work, it was decided to sort the acoustic waves such that the first one always is incoming for an inlet, and outgoing for an outlet. This of course also means that the second acoustic wave always is outgoing for an inlet, and incoming for an outlet. This sorting of the waves is easily achieved by swapping the values of  $k_{x,4}$  and  $k_{x,5}$  in cases when the first acoustic wave turns out to be either outgoing for an inlet or incoming for an outlet. The reason why this simple swap is enough is that the matrices  $T$  and  $T^{-1}$  are defined in terms of  $k_{x,4}$  and  $k_{x,5}$ .

The matrix  $T_{1D}$  can also be defined such that the first four columns always represent incoming waves for an inlet and outgoing waves for an outlet. To do this, we start by

defining the speed of the two acoustic waves, here denoted  $\lambda_4$  and  $\lambda_5$ , as follows

$$\begin{aligned} \bar{v}_x n < 0 : \begin{cases} \lambda_4 &= \bar{v}_x - n\bar{c} \\ \lambda_5 &= \bar{v}_x + n\bar{c} \end{cases} \\ \bar{v}_x n > 0 : \begin{cases} \lambda_4 &= \bar{v}_x + n\bar{c} \\ \lambda_5 &= \bar{v}_x - n\bar{c} \end{cases} \end{aligned} \quad (3.57)$$

Here,  $n = \pm 1$  indicates whether the boundary is pointing in the positive, or negative, axial direction. Using the above definition of the acoustic wave speeds, the matrix  $T_{1D}$  may be written as

$$T_{1D} = \begin{bmatrix} \bar{\rho} & 0 & 0 & \bar{\rho} & \bar{\rho} \\ 0 & 0 & 0 & \lambda_4 - \bar{v}_x & \lambda_5 - \bar{v}_x \\ 0 & \bar{c} & 0 & 0 & 0 \\ 0 & 0 & \bar{c} & 0 & 0 \\ 0 & 0 & 0 & \bar{\rho} \bar{c}^2 & \bar{\rho} \bar{c}^2 \end{bmatrix} \quad (3.58)$$

Note that this matrix, apart from a possible permutation of the fourth and fifth column, is equivalent to the one defined in Appendix A.

Now that we have defined  $T_{1D, \text{inc}}$ , we can compute the inverse of  $T_{\text{inc}}^{-1} T_{1D, \text{inc}}$  used in Eq. (3.53). For an inlet, it becomes

$$(T_{\text{inc}}^{-1} T_{1D, \text{inc}})^{-1} = \begin{bmatrix} 1 & 0 & 0 & 0 \\ 0 & 1 & 0 & 0 \\ 0 & 0 & \kappa_1 (\xi_1 k_{x,1} (\bar{v}_x - \lambda_4) \bar{v}_x + \xi_2 (k_{x,1}^2 + k_z^2) \bar{v}_x \bar{c}) & 2\kappa_1 \xi_2 k_z (\bar{c}^2 - \bar{v}_x^2 + \lambda_4 \bar{v}_x) \\ 0 & 0 & \kappa_1 \xi_1 k_z \bar{v}_x \bar{c} & 2\kappa_1 \xi_2 k_{x,1} \bar{v}_x \bar{c} \end{bmatrix} \quad (3.59)$$

where

$$\begin{aligned} \kappa_1 &= \frac{1}{\bar{v}_x (\xi_1 (\bar{v}_x - \lambda_4) + \xi_2 k_{x,1} \bar{c} + k_z^2 (k_{x,1} - k_{x,4}) \bar{c}^2)} \\ \xi_1 &= (k_{x,1}^2 + k_z^2) (k_{x,4} - k_{x,1}) \bar{v}_x \\ \xi_2 &= (k_{x,1} k_{x,4} + k_z^2) \bar{c} \end{aligned} \quad (3.60)$$

For an outlet, the inverse of  $T_{\text{inc}}^{-1} T_{1D, \text{inc}}$  further becomes

$$(T_{\text{inc}}^{-1} T_{1D, \text{inc}})^{-1} = [2\kappa_2 \bar{v}_x \xi_4 k_{x,1} \bar{c}] \quad (3.61)$$

where

$$\begin{aligned} \kappa_2 &= \frac{1}{\bar{v}_x (\xi_3 (\bar{v}_x - \lambda_5) + \xi_4 k_{x,1} \bar{c} + k_z^2 (k_{x,1} - k_{x,5}) (\bar{v}_x - \lambda_5) \bar{v}_x)} \\ \xi_3 &= (k_{x,1}^2 + k_z^2) (k_{x,5} - k_{x,1}) \bar{v}_x \\ \xi_4 &= (k_{x,1} k_{x,5} + k_z^2) \bar{c} \end{aligned} \quad (3.62)$$

### 3.3 Duct Modes

In this section, a normal mode analysis of the linearized Euler equations will be used to compute how small-amplitude disturbances propagate through an annular duct with a constant cross-section. A normal mode analysis has previously been adopted by several other authors for the same purpose, see e.g. [40, 74, 75, 79, 70, 95, 51]. A normal mode analysis is one of several methods that can be used to calculate how these disturbances, hereinafter referred to as duct-modes, propagate. Other approaches include solving an initial boundary value problem [99] or using a Green’s function approach [84]. Although the normal mode analysis is a rather simple approach for computing duct modes, it must be pointed out that it does not necessarily provide all permissible modes in complex situations including, e.g., swirling flows [99]. The normal mode analysis can also give spurious modes, i.e., modes that have no physical meaning. Although filtering can be used to eliminate some of them, there appears to exist no rigorous method for determining which ones that are physical and not.

The aim of the present work was to create a simple, transparent, and well-documented tool for computing duct-modes based on a normal mode analysis approach. The result of this effort is **noisyduck**, an open-source Python tool available on GitHub. In what follows, a brief overview of the numerical methods employed in **noisyduck** will be presented. Before this is done, however, it should be noted that some differences with regards to nomenclature exist between the equations presented in this thesis and the ones employed in **noisyduck**. For a complete reference on the equations used in **noisyduck**, the reader is referred to the official publication [105] and to the documentation available on GitHub.

#### 3.3.1 Linearized Euler Equations

The duct modes analyzed in the present work are assumed to satisfy the following form of the linearized Euler equations

$$\frac{\partial q'}{\partial t} + \overline{A} \frac{\partial q'}{\partial x} + \overline{B} \frac{\partial q'}{\partial r} + \frac{1}{r} \overline{C} \frac{\partial q'}{\partial \theta} - \overline{D} q' = 0 \quad (3.63)$$

Here,  $q' = (\rho', v'_x, v'_r, v'_\theta, p')^T$  contains perturbations of the primitive flow variables with respect to a temporally+circumferentially averaged mean flow  $\bar{q}$ . The matrices  $\overline{A}$ ,  $\overline{B}$ ,  $\overline{C}$  and  $\overline{D}$  in the above equation are defined in Appendix A.

Equation (3.63) was obtained by first linearizing the nonlinear Euler equations for a perfect, ideal gas, with respect to the mean flow  $\bar{q}$ . The resulting system of equations was then further simplified by assuming that  $\bar{q}$  remains constant with  $x$  and that the duct has a constant cross-section. From these assumptions, it follows that the most general mean flow is an axial/circumferential flow that satisfies radial equilibrium

$$\begin{aligned} \bar{\rho} &= \bar{\rho}(r) \\ \bar{v}_x &= \bar{v}_x(r) & \bar{v}_r &= 0 & \bar{v}_\theta &= \bar{v}_\theta(r) \\ \frac{\partial \bar{p}}{\partial r} &= \frac{\bar{\rho} \bar{v}_\theta^2}{r} \end{aligned} \quad (3.64)$$

More details on the derivation of Eq. (3.63), including a proof of Eq. (3.64), is provided in Appendix A.

### 3.3.2 Normal Mode Analysis

The normal mode analysis adopted in this work assumes that a flow perturbation in Eq. (3.63) takes on the following form [40, 74, 79]

$$q'(x, r, \theta, t) = \hat{q}(r)e^{i(\omega t - k_x x - m\theta)} \quad (3.65)$$

This equation is equivalent to the ansatz used in section 3.2 to determine which modes that can exist in the flow according to Eq. (3.21). By substituting Eq. (3.65) into Eq. (3.63), we obtain the following

$$\left[ i\omega - ik_x \bar{A} + \bar{B} \frac{\partial}{\partial r} - i \frac{m}{r} \bar{C} - \bar{D} \right] \hat{q}(r) = 0 \quad (3.66)$$

This is an ordinary differential equation in  $r$ . Next, the numerical method used to solve this differential equation will be outlined.

### 3.3.3 Spatial Discretization

The numerical method adopted in the present work is based on discretizing Eq. (3.66) on a grid that consists of  $N$  uniformly distributed nodes in the radial direction. The final result of the discretization may be written as

$$[i\omega \mathcal{I} + \mathcal{L}_r - \mathcal{L}_\theta - \mathcal{S}] \hat{\mathbf{q}} = k_x \mathcal{L}_x \hat{\mathbf{q}} \quad (3.67)$$

Here,  $\hat{\mathbf{q}} \in \mathbb{C}^{5N}$  is a vector that contains the discrete values of  $\hat{q}(r)$ , organized as

$$\hat{\mathbf{q}} = \begin{bmatrix} \hat{\rho} \\ \hat{v}_x \\ \hat{v}_r \\ \hat{v}_\theta \\ \hat{p} \end{bmatrix} \quad (3.68)$$

The matrices in Eq. (3.67) are further defined as

$$\begin{aligned}
\mathcal{L}_x &= \begin{bmatrix} i[\bar{\mathbf{v}}_x] & i[\bar{\boldsymbol{\rho}}] & 0 & 0 & 0 \\ 0 & i[\bar{\mathbf{v}}_x] & 0 & 0 & i[1/\bar{\boldsymbol{\rho}}] \\ 0 & 0 & i[\bar{\mathbf{v}}_x] & 0 & 0 \\ 0 & 0 & 0 & i[\bar{\mathbf{v}}_x] & 0 \\ 0 & i[\gamma\bar{\boldsymbol{\rho}}] & 0 & 0 & i[\bar{\mathbf{v}}_x] \end{bmatrix} & \mathcal{L}_r &= \begin{bmatrix} 0 & 0 & [\bar{\boldsymbol{\rho}}]\mathcal{D} & 0 & 0 \\ 0 & 0 & 0 & 0 & 0 \\ 0 & 0 & 0 & 0 & [1/\bar{\boldsymbol{\rho}}]\mathcal{D} \\ 0 & 0 & 0 & 0 & 0 \\ 0 & 0 & [\gamma\bar{\boldsymbol{\rho}}]\mathcal{D} & 0 & 0 \end{bmatrix} \\
\mathcal{L}_\theta &= \begin{bmatrix} im[\mathcal{R}\bar{\mathbf{v}}_\theta] & 0 & 0 & im[\mathcal{R}\bar{\boldsymbol{\rho}}] & 0 \\ 0 & im[\mathcal{R}\bar{\mathbf{v}}_\theta] & 0 & 0 & 0 \\ 0 & 0 & im[\mathcal{R}\bar{\mathbf{v}}_\theta] & 0 & 0 \\ 0 & 0 & 0 & im[\mathcal{R}\bar{\mathbf{v}}_\theta] & im[\mathcal{R}(1/\bar{\boldsymbol{\rho}})] \\ 0 & 0 & 0 & im[\gamma\mathcal{R}\bar{\boldsymbol{\rho}}] & im[\mathcal{R}\bar{\mathbf{v}}_\theta] \end{bmatrix} \\
\mathcal{S} &= \begin{bmatrix} 0 & 0 & -[\mathcal{D}\bar{\boldsymbol{\rho}}] - [\mathcal{R}\bar{\boldsymbol{\rho}}] & 0 & 0 \\ 0 & 0 & -[\mathcal{D}\bar{\mathbf{v}}_x] & 0 & 0 \\ [\mathcal{R}(\bar{\mathbf{v}}_\theta^2/\bar{\boldsymbol{\rho}})] & 0 & 0 & [2\mathcal{R}\bar{\mathbf{v}}_\theta] & 0 \\ 0 & 0 & -[\mathcal{D}\bar{\mathbf{v}}_\theta] - [\mathcal{R}\bar{\mathbf{v}}_\theta] & 0 & 0 \\ 0 & 0 & -[\mathcal{D}\bar{\boldsymbol{\rho}}] - [\gamma\mathcal{R}\bar{\boldsymbol{\rho}}] & 0 & 0 \end{bmatrix}
\end{aligned} \tag{3.69}$$

Here,  $[\mathbf{f}] = \text{diag}(\mathbf{f})$  is used to denote the diagonal matrix generated by the vector  $\mathbf{f}$ . The matrices  $\mathcal{D}$  and  $\mathcal{R}$  in the above equation further represent the fourth-order, vertex based, finite difference operator introduced by [54], and a matrix that contains the inverse radial scaling. They are respectively defined as

$$\mathcal{D} = \frac{1}{12\Delta r} \begin{bmatrix} -25 & 48 & -36 & 16 & -3 \\ -3 & -10 & 18 & -6 & 1 \\ 1 & -8 & 0 & 8 & -1 \\ & \cdot & \cdot & \cdot & \cdot \\ & & \cdot & \cdot & \cdot & \cdot \\ & & & \cdot & \cdot & \cdot & \cdot \\ & & & & 1 & -8 & 0 & 8 & -1 \\ & & & & -1 & 6 & -18 & 10 & 3 \\ & & & & 3 & -16 & 36 & -48 & 25 \end{bmatrix} \tag{3.70}$$

and

$$\mathcal{R} = \begin{bmatrix} \frac{1}{r_1} & 0 & \dots & & 0 \\ 0 & \frac{1}{r_2} & 0 & \dots & 0 \\ \vdots & 0 & \frac{1}{r_3} & 0 & \dots & 0 \\ & \vdots & 0 & \ddots & & 0 \\ & & \vdots & & & 0 \\ 0 & 0 & 0 & 0 & 0 & \frac{1}{r_N} \end{bmatrix} \tag{3.71}$$

## Boundary Conditions

Before Eq. (3.67) can be solved, appropriate boundary conditions must be specified at the duct walls. In the present work, a simple hard-wall boundary condition has been adopted [99, 70, 55]

$$\hat{v}_r(r_1) = \hat{v}_r(r_N) = 0 \quad (3.72)$$

This boundary condition is implemented by modifying the first/last row in Eq. (3.67).

### 3.3.4 Numerical Solution Strategy

Equation (3.67) represents a generalized eigenvalue problem, in which the eigenvalues represent the axial wavenumbers, and the eigenvectors the mode shapes. In the present work, this eigenvalue problem is solved using the eigenvalue solver available in SciPy. Unfortunately, some of the duct-modes that are obtained from the eigenvalue solver will be spurious, i.e., contain no physical information. To sort these out, the filtering procedure proposed by Maldonado et al. [70] has been adopted. In this approach, the 15 point DRP filter proposed by Tam [98] is first applied to the pressure mode according to

$$\tilde{p}(r_j) = \sum_{k=-7}^7 a_k \hat{p}(r_{j+k}), \quad j = 1, \dots, N \quad (3.73)$$

Here,  $a_k$  are the coefficients used by the filter, and  $\tilde{\mathbf{p}}$  represents the filtered pressure. Note that the above equation also is applied at the end-points of the domain by mirroring the solution there.

The DRP filter in Eq. (3.73) has been designed to remove low frequency components from the solution [98]. Given that we are mainly interested in well-resolved modes (i.e. with low radial mode order), a mode should be kept if the norm of  $\tilde{\mathbf{p}}$  is significantly lower than  $\hat{\mathbf{p}}$ . That is, if the ratio

$$\alpha = \frac{\|\tilde{\mathbf{p}}\|_2}{\|\hat{\mathbf{p}}\|_2} \quad (3.74)$$

is lower than some predefined value  $\alpha_{\max}$ . The  $l_2$  norm in the above equation has been modified to account for the cylindrical coordinate system as [70]

$$\|\mathbf{f}\|_2^2 = \frac{1}{2} \sum_{j=1}^{N-1} (r_{j+1} - r_j) (r_j |f(r_j)|^2 + r_{j+1} |f(r_{j+1})|^2) \quad (3.75)$$

### 3.3.5 Classification of Modes

The duct modes obtained in the previous section describe how flow-disturbances with known frequencies and nodal diameters propagate through an annular duct with a constant cross-section. This information can be used for several purposes, such as post-processing a numerical simulation, or constructing nonreflecting boundary conditions. In both of these cases, the direction of propagation of the modes, as well as their physical meaning,

must be determined. For example, if we are interested in computing how noise propagates upstream through the inlet of an axial flow turbomachine, we are mainly interested in acoustic modes that propagate upstream. If on the other hand, we want to construct a nonreflecting boundary condition, then all physically meaningful duct modes must be identified and then split into upstream and downstream propagating ones.

The method proposed by Moinier et al. [74] for splitting modes into upstream and downstream propagating ones was adopted in this work. In this method, it is assumed that no unstable (exponentially growing) modes are present in the flow. From this assumption, it follows that all modes which satisfy  $\text{Im}(k_x) \neq 0$  can be interpreted as decaying. Their direction or propagation, or rather, their direction of decay, can furthermore be determined from the sign of  $\text{Im}(k_x)$ . Referring to Eq. (3.65), it can be seen that a negative imaginary part implies that the mode decays in the positive axial direction, whereas the opposite holds for a mode with a positive imaginary part.

All modes do however not have axial wavenumbers with a non-zero imaginary part, i.e., they are not decaying. To be able to treat these modes in the same way as the decaying ones, a small, negative, imaginary part is added to the frequency before the eigenvalue problem is solved. As shown by Moinier et al. [74], this causes a mode that would normally not decay, to decay in a direction consistent with its group velocity. Note that the same approach was adopted to determine the direction of propagation of the two-dimensional waves used for the construction of the nonreflecting boundary condition described in section 3.2.

Once the direction of propagation of modes has been determined, they can be split into upstream and downstream propagating modes. What remains to be determined before a boundary condition, or post-processing tool, can be constructed is the physical nature of the modes. No effort has been put on this step in the present work. One possible way that this can be achieved, however, would be to adopt the method presented by Moinier et al. [74]. In this approach, all upstream propagating modes are assumed to be acoustic modes. The downstream modes are then classified as either entropy, vorticity, or downstream propagating acoustic modes by examining the amplitude of the density and pressure perturbations that they induce. Although this approach does not necessarily give a perfect classification, it has been shown to give satisfactory results when used to construct nonreflecting boundary conditions by Moinier et al. [75].

## 4 Generation and Propagation of Sound: The Acoustic Analogy

The aeroacoustic analogy was introduced by Sir Michael James Lighthill to define the processes through which sound is generated in a turbulent flow field [60, 61]. In his acoustic analogy, the aerodynamic sound source is defined as the difference between the exact wave equation written in terms of density fluctuations, and the wave equation that governs density fluctuations in the far-field (where the flow is assumed to be uniform and at rest). The exact wave equation is obtained by rewriting the continuity and momentum equations, which read

$$\begin{aligned}\frac{\partial \rho}{\partial t} + \frac{\partial \rho u_i}{\partial x_i} &= 0 \\ \frac{\partial \rho u_i}{\partial t} + \frac{\partial \rho u_i u_j}{\partial x_j} + \frac{\partial p_{ij}}{\partial x_j} &= 0\end{aligned}\tag{4.1}$$

Here,  $p_{ij} = p\delta_{ij} - \sigma_{ij}$  is the compressive stress tensor. By taking the time derivative of the continuity equation and then subtracting the divergence of the momentum equation from the resulting expression, the following is obtained

$$\frac{\partial^2 \rho}{\partial t^2} = \frac{\partial^2 \rho u_i u_j}{\partial x_i \partial x_j} + \frac{\partial^2 p_{ij}}{\partial x_i \partial x_j}\tag{4.2}$$

Perturbation variables are now defined to be the difference between the local fluid state and the far field state as

$$\begin{aligned}\rho' &= \rho - \rho_0 \\ u'_i &= u_i - U_{i,0} \\ p' &= p - p_0\end{aligned}\tag{4.3}$$

By introducing these perturbation variables into Eq. (4.2) and then subtract  $c_0^2 \frac{\partial^2 \rho'}{\partial x_i \partial x_i}$  from both sides of the resulting expression, the famous Lighthill equation is obtained

$$\frac{\partial^2 \rho'}{\partial t^2} - c_0^2 \frac{\partial^2 \rho'}{\partial x_i \partial x_i} = \frac{\partial^2 T_{ij}}{\partial x_i \partial x_j}\tag{4.4}$$

Here,

$$T_{ij} = \rho u'_i u'_j + (p' - c_0^2 \rho') \delta_{ij} - \sigma_{ij}\tag{4.5}$$

is the Lighthill tensor. It should be noted that it was derived under the assumption that the far-field state is at rest, i.e. that  $U_{i,0} = 0$ .

By comparing Eq. (4.4) to the ordinary wave equation, it can be seen that  $\frac{\partial^2 T_{ij}}{\partial x_i \partial x_j}$  represents a source term. More precisely, since the Lighthill equation was derived without assumptions from the Navier-Stokes equations, the source term includes all effects that the flow has on sound generation and propagation.



The Lighthill equation presented in Eq. (4.4) can be formally solved by forming a convolution between the right-hand side of Eq. (4.4) and a free-space Green's function to the wave operator. This will give the density fluctuation at the observer expressed as a volume integral over the subset of  $\mathbb{R}^3$  where  $T_{ij}$  has non-negligible amplitude. Since the Lighthill tensor includes all effects of sound generation and propagation, this solution will furthermore be exact. By utilizing the isentropic relation  $p' = c_0^2 \rho'$ , which is assumed to be valid at the observer, the pressure signal can finally be obtained at the observer.

An important achievement obtained by Lighthill is the direct connection between the sound at an observer and the sound sources defined in Eq. (4.5). The exact value of the sound source is however still an unknown that must be obtained by other means, such as from a CFD simulation. Lighthill's analogy is however seldom used to post-process CFD simulations since it does not take solid surfaces into account. The presence of stationary, solid, surfaces was added to Lighthill's analogy by Curle [11]. An even more general acoustic analogy for surfaces in arbitrary motion was later developed by Ffowcs Williams and Hawkings [24].

The fundamental problem that occurs when solid surfaces are present is that the flow equations are no longer valid throughout  $\mathbb{R}^3$ , which prevents a free-space Green's function from being applied to solve Eq. (4.4). The pioneering idea introduced by Ffowcs Williams and Hawkings to solve this problem was to "cut out" the part of  $\mathbb{R}^3$  where solid surfaces are present and replace this volume with a fluid attaining the far-field state. This approach is illustrated in Fig. 4.1, where the fluid in  $V$  is assumed to attain the state  $\rho_0$ ,  $U_{i,0}$ , and  $p_0$ , whereas the fluid remains in its actual state outside  $\partial V$ . If  $f$  is defined to be a scalar field such that  $f(\mathbf{x}, t) < 0$  for  $\mathbf{x} \in V$  and  $f(\mathbf{x}, t) > 0$  elsewhere, new fluid fields defined throughout  $\mathbb{R}^3$  may be defined in terms of the Heaviside step function

$$\begin{aligned}\underline{\rho} &= \rho_0(1 - H(f)) + \rho H(f) \\ \underline{p} &= p_0(1 - H(f)) + p H(f) \\ \underline{u}_i &= U_{i,0}(1 - H(f)) + u_i H(f)\end{aligned}\tag{4.6}$$

At this point, we note that the new fields satisfy Eq. (4.1) everywhere except at the boundary  $\partial V$  where they are discontinuous. This non-differentiability can be overcome by reinterpreting the new fields in terms of distributions, also known as generalized functions. In this thesis, only some basic results from generalized function theory will be used to derive the Ffowcs Williams-Hawkings equation. For a good introduction to the subject, including many useful formulas for aerodynamic and acoustic applications, the reader is referred to the work of Farassat [22]. Some more fundamentals on generalized function theory that also may help in following the derivation presented hereinafter may be found in introductory textbooks on the subjects of Fourier- and Functional analysis, see e.g. [25, 12]

Let  $\mathcal{D}(\mathbb{R}^N)$  denote the set of all infinitely differentiable functions on  $\mathbb{R}^N$  that have bounded support. A function  $\phi(\mathbf{x})$  that belongs to this set is commonly called a test function. A distribution  $g[\phi] : \mathcal{D}(\mathbb{R}^N) \mapsto \mathbb{C}$  is defined as a continuous, linear mapping between the set of all test functions and the complex numbers. In other words,  $g[\phi]$  is a continuous, linear functional defined on  $\mathcal{D}(\mathbb{R}^N)$ . For a rigorous definition of the concepts of linearity and continuity, see [12]. In case  $g(\mathbf{x})$  is an integrable function, the

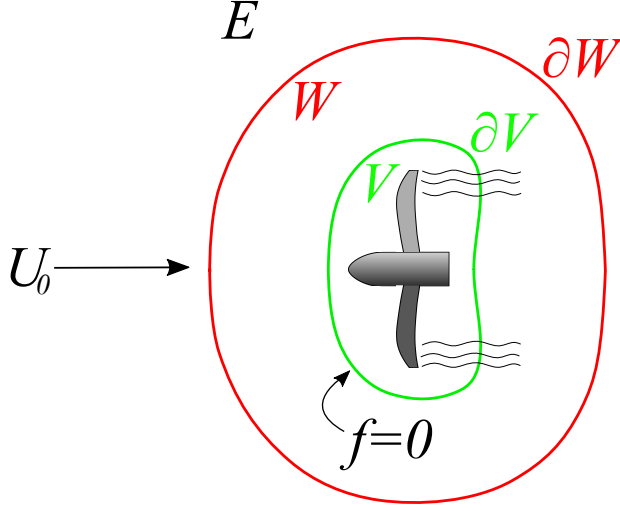


Figure 4.1: *Schematic View of the Ffowcs Williams-Hawkins Approach.*

corresponding distribution  $g[\phi]$  is referred to as a regular distribution, and the mapping is defined by an integral

$$g[\phi] = \int_{\mathbb{R}^N} g(\mathbf{x})\phi(\mathbf{x})d^N \mathbf{x} \quad (4.7)$$

This also defines the notation that will be used throughout this thesis, namely that the underlying function is denoted by  $g$  or  $g(\mathbf{x})$ , whereas the corresponding distribution is denoted  $g[\phi]$ . Note however that not all distributions can be defined in terms of an integral. These distributions are known as singular distributions [25]. The partial derivative of any distribution is defined as follows [25]

$$\begin{aligned} (\partial^\alpha g)[\phi] &= (-1)^{|\alpha|} g[\partial^\alpha \phi] \\ \partial^\alpha &= \frac{\partial^{|\alpha|}}{\partial x_1^{\alpha_1} \partial x_2^{\alpha_2} \dots \partial x_N^{\alpha_N}} \\ |\alpha| &= \alpha_1 + \alpha_2 + \dots + \alpha_N \end{aligned} \quad (4.8)$$

for some positive integers  $\alpha_1, \dots, \alpha_N$ .

In the next section, the continuity and momentum equations formulated in terms of distributional derivatives will be derived. These are later combined in the same way as was done previously in order to derive the Lighthill equation. This will result in the famous Ffowcs Williams - Hawkins equation, which essentially is the Lighthill equation with some additional sources that account for the sound generation introduced by the discontinuity surface  $\partial V$ .

## 4.1 Derivation of the Convective Ffowcs Williams - Hawkings Equation

In the original paper by Ffowcs Williams and Hawkings [24], an inhomogeneous wave equation for the special case when  $\partial V$  coincides with a solid surface is presented. The derivation presented in [24] does however not rely on this simplification, and their theory is thus fully applicable to arbitrary surfaces that enclose all solid boundaries. A complete wave equation where the simplification was not included was later presented by di Francescantonio [26]. In this latter case,  $\partial V$  is often referred to as a porous surface, since the fluid can cross it.

The acoustic analogies cited so far all assumed that the surrounding fluid is at rest ( $U_{i,0} = 0$ ). It is possible to include the effects of a uniform mean flow by moving both the observer and the surface when evaluating the integral solution of the Ffowcs Williams - Hawkings equation [21]. Another approach presented by Najafi-Yazidi et al. is to explicitly account for the presence of a uniform mean flow in the derivation [78]. The resulting wave equation, hereinafter referred to as the convective Ffowcs Williams-Hawkings equation, will include a convective wave operator, in which the time derivative is replaced by a Lagrangian derivative according to

$$\frac{\partial^2}{\partial t^2} - c_0^2 \frac{\partial^2}{\partial x_j \partial x_j} \rightarrow \left( \frac{\partial}{\partial t} + U_{j,0} \frac{\partial}{\partial x_j} \right)^2 - c_0^2 \frac{\partial^2}{\partial x_j \partial x_j} \quad (4.9)$$

In this thesis, a derivation of the convective Ffowcs Williams-Hawkings equation for the case when  $\partial V$  is a stationary, porous surface is presented. This implies that the function  $f$  that defines  $\partial V$  is a function of space, but not time.

The derivation of the convective Ffowcs Williams-Hawkings equation starts by expressing the continuity and momentum equations in terms of derivatives of the distributions generated by the new fields defined in Eq. (4.6). By noting that the test functions are functions of both space and time, the following is obtained

$$\begin{aligned} \frac{\partial \rho}{\partial t}[\phi] + \frac{\partial \rho u_i}{\partial x_i}[\phi] &= - \int_t \int_{\mathbb{R}^3} \rho \frac{\partial \phi}{\partial t} d^3 \mathbf{x} dt - \int_t \int_{\mathbb{R}^3} \rho u_i \frac{\partial \phi}{\partial x_i} d^3 \mathbf{x} dt \\ &= - \underbrace{\int_t \int_V \rho_0 \frac{\partial \phi}{\partial t} d^3 \mathbf{x} dt}_I - \underbrace{\int_t \int_W \rho \frac{\partial \phi}{\partial t} d^3 \mathbf{x} dt}_{II} \\ &\quad - \underbrace{\int_t \int_E \rho \frac{\partial \phi}{\partial t} d^3 \mathbf{x} dt}_{III} - \underbrace{\int_t \int_V \rho_0 U_{i,0} \frac{\partial \phi}{\partial x_i} d^3 \mathbf{x} dt}_{IV} \\ &\quad - \underbrace{\int_t \int_W \rho u_i \frac{\partial \phi}{\partial x_i} d^3 \mathbf{x} dt}_V - \underbrace{\int_t \int_E \rho u_i \frac{\partial \phi}{\partial x_i} d^3 \mathbf{x} dt}_{VI} \end{aligned} \quad (4.10)$$

The terms  $I$  and  $II$  in Eq. (4.10) can be integrated by parts in time. Similarly, the terms  $IV$  and  $V$  can be integrated by parts using the divergence theorem. Since  $\phi$  vanishes

when  $t \rightarrow \pm\infty$  due to the bounded support of the test functions, the following is obtained

$$\begin{aligned}
\frac{\partial \rho}{\partial t}[\phi] + \frac{\partial \rho u_i}{\partial x_i}[\phi] = & \underbrace{\int_t \int_V \frac{\partial \rho_0}{\partial t} \phi d^3 \mathbf{x} dt}_I + \underbrace{\int_t \int_W \frac{\partial \rho}{\partial t} \phi d^3 \mathbf{x} dt}_{II} \\
& - \underbrace{\int_t \int_E \rho \frac{\partial \phi}{\partial t} d^3 \mathbf{x} dt}_{III} + \underbrace{\int_t \int_V \frac{\partial \rho_0 U_{i,0}}{\partial x_i} \phi d^3 \mathbf{x} dt}_{IV} \\
& + \underbrace{\int_t \int_W \frac{\partial \rho u_i}{\partial x_i} \phi d^3 \mathbf{x} dt}_V - \underbrace{\int_t \int_E \rho u_i \frac{\partial \phi}{\partial x_i} d^3 \mathbf{x} dt}_{VI} \\
& - \underbrace{\int_t \int_{\partial V} \rho_0 U_{i,0} n_i \phi dS dt}_{VII} + \underbrace{\int_t \int_{\partial V} \rho u_i n_i \phi dS dt}_{VIII} \\
& - \underbrace{\int_t \int_{\partial W} \rho u_i n_i \phi dS dt}_{IX}
\end{aligned} \tag{4.11}$$

Here,  $dS$  is used to denote the area element of the surface that the integral is being evaluated over. Note that the integral denoted  $VIII$  in Eq. (4.11) stems from the integration by parts of term  $V$  in Eq. (4.10) and that the sign of this integral has been changed to define the integral with a unit normal pointing out of the volume  $V$ . At this point, it can be noted that the combination of the terms  $I$  and  $IV$  in Eq. (4.11) will cancel since the mean flow satisfies the continuity equation inside  $V$ . The same argument results in that the terms  $II$  and  $V$  cancel. We now let the surface  $\partial W$  expand to infinity in the sense that it becomes large enough for  $\phi$  to be zero on and outside it. This will make the terms  $III$ ,  $VI$ , and  $IX$  vanish, yielding the following final form of the continuity equation

$$\begin{aligned}
\frac{\partial \rho}{\partial t}[\phi] + \frac{\partial \rho u_i}{\partial x_i}[\phi] &= \int_t \int_{\partial V} (\rho(U_{0,i} + u'_i) - \rho_0 U_{i,0}) n_i \phi dS dt \\
&= Q[\phi]
\end{aligned} \tag{4.12}$$

The integral on the right hand side defines a new distribution  $Q[\phi]$  that represents a mass flux term necessary for maintaining mass conservation on both sides of  $\partial V$ .

The momentum equation written in terms of derivatives of the distributions generated

by the fields in Eq. (4.6) is furthermore given by

$$\begin{aligned}
\frac{\partial \rho u_i}{\partial t}[\phi] + \frac{\partial \rho u_i u_j}{\partial x_j}[\phi] + \frac{\partial p_{ij}}{\partial x_j}[\phi] = & - \underbrace{\int_t \int_V \rho_0 U_{i,0} \frac{\partial \phi}{\partial t} d^3 \mathbf{x} dt}_I - \underbrace{\int_t \int_W \rho u_i \frac{\partial \phi}{\partial t} d^3 \mathbf{x} dt}_{II} \\
& - \underbrace{\int_t \int_E \rho u_i \frac{\partial \phi}{\partial t} d^3 \mathbf{x} dt}_{III} \\
& - \underbrace{\int_t \int_V (\rho_0 U_{i,0} U_{j,0} + p_0 \delta_{ij}) \frac{\partial \phi}{\partial x_j} d^3 \mathbf{x} dt}_{IV} \\
& - \underbrace{\int_t \int_W (\rho u_i u_j + p_{ij}) \frac{\partial \phi}{\partial x_j} d^3 \mathbf{x} dt}_V \\
& - \underbrace{\int_t \int_E (\rho u_i u_j + p_{ij}) \frac{\partial \phi}{\partial x_j} d^3 \mathbf{x} dt}_{VI}
\end{aligned} \tag{4.13}$$

In this equation, the term  $IV$  has been simplified by the fact that the viscous stress tensor  $\sigma_{ij} = 0$  inside the volume  $V$ . The procedure for rewriting the right-hand side of Eq. (4.13) is similar to the one used for the continuity equation. First, the terms  $I$  and  $II$  are integrated by parts in time and the fact that the test functions vanish at infinity is used to remove the integrated terms. The divergence theorem is then used to integrate the terms  $IV$  and  $V$  by parts. The volume integrals over  $V$  and  $W$  resulting from the integration by parts can then be canceled since the momentum equation is satisfied inside both these volumes. By finally letting  $\partial W$  grow to infinity, all integrals over  $\partial W$  and  $E$  will disappear to yield the following expression

$$\begin{aligned}
\frac{\partial \rho u_i}{\partial t}[\phi] + \frac{\partial \rho u_i u_j}{\partial x_j}[\phi] + \frac{\partial p_{ij}}{\partial x_j}[\phi] &= \int_t \int_{\partial V} [\rho u_i u_j - \rho_0 U_{i,0} U_{j,0} + (p - p_0) \delta_{ij} - \sigma_{ij}] n_j \phi dS dt \\
&= \tilde{L}_i[\phi]
\end{aligned} \tag{4.14}$$

The integral on the right hand side defines the distribution  $\tilde{L}_i[\phi]$ , which represents an extra momentum flux necessary to satisfy conservation of momentum on both sides of  $\partial V$ .

In order to rigorously derive the convective Ffowcs Williams - Hawkings equations, new discontinuous perturbation variables are now defined based on Eq. (4.6) as

$$\begin{aligned}
\underline{\rho}' &= \underline{\rho} - \rho_0 \\
\underline{p}' &= \underline{p} - p_0 \\
\underline{u}'_i &= \underline{u}_i - U_{i,0}
\end{aligned} \tag{4.15}$$

It is easy to verify that these definitions are equivalent to the perturbation variables defined in Eq. (4.3) multiplied by  $H(f)$ , e.g.  $\underline{\rho}' = H(f)\rho'$ . The distributions defined by the discontinuous perturbation variables will be denoted by e.g.  $\rho'[\phi]$  for the density. It is easy to verify that these new distributions satisfy the following intuitive relation

$$(\partial^\alpha \rho)[\phi] = (\partial^\alpha \rho')[\phi] \quad (4.16)$$

By taking the material derivative of the continuity equation (4.12) and subtracting the divergence of the momentum equation (4.14), the following is obtained

$$\begin{aligned} \frac{\partial^2 \rho}{\partial t^2}[\phi] + U_{j,0} \frac{\partial^2 \rho}{\partial x_j \partial t}[\phi] + U_{j,0} \frac{\partial^2 \rho u_i}{\partial x_j \partial x_i}[\phi] - \frac{\partial^2 \rho u_i u_j}{\partial x_i x_j}[\phi] &= \left( \frac{\partial}{\partial t} + U_{j,0} \frac{\partial}{\partial x_j} \right) Q[\phi] \\ &\quad - \frac{\partial}{\partial x_i} \tilde{L}_i[\phi] \\ &\quad + \frac{\partial^2 p_{ij}}{\partial x_i \partial x_j}[\phi] \end{aligned} \quad (4.17)$$

The two last terms on the left-hand side of Eq. (4.17) can be rewritten as follows using the continuity equation

$$\begin{aligned} U_{j,0} \frac{\partial^2 \rho u_i}{\partial x_j \partial x_i}[\phi] - \frac{\partial^2 \rho u_i u_j}{\partial x_i x_j}[\phi] &= + U_{i,0} U_{j,0} \frac{\partial^2 \rho}{\partial x_j \partial x_i}[\phi] + U_{j,0} \frac{\partial^2 \rho u'_i}{\partial x_j \partial x_i}[\phi] \\ &\quad - U_{j,0} \frac{\partial^2 \rho u_i}{\partial x_j \partial x_i}[\phi] - U_{i,0} \frac{\partial^2 \rho u'_j}{\partial x_i \partial x_j}[\phi] - \frac{\partial^2 \rho u'_i u'_j}{\partial x_i \partial x_j}[\phi] \\ &= + U_{i,0} U_{j,0} \frac{\partial^2 \rho}{\partial x_j \partial x_i}[\phi] - U_{j,0} \frac{\partial}{\partial x_j} Q[\phi] \\ &\quad + U_{j,0} \frac{\partial^2 \rho}{\partial x_j \partial t}[\phi] - \frac{\partial^2 \rho u'_i u'_j}{\partial x_i \partial x_j}[\phi] \end{aligned} \quad (4.18)$$

By inserting this result into Eq. (4.17), the following is obtained

$$\begin{aligned} \frac{\partial^2 \rho}{\partial t^2}[\phi] + 2U_{j,0} \frac{\partial^2 \rho}{\partial x_j \partial t}[\phi] + U_{i,0} U_{j,0} \frac{\partial^2 \rho}{\partial x_j \partial x_i}[\phi] &= \left( \frac{\partial}{\partial t} + U_{j,0} \frac{\partial}{\partial x_j} \right) Q[\phi] \\ &\quad - \frac{\partial}{\partial x_i} \tilde{L}_i[\phi] + U_{j,0} \frac{\partial}{\partial x_j} Q[\phi] \\ &\quad + \frac{\partial^2 \rho u'_i u'_j}{\partial x_i \partial x_j}[\phi] + \frac{\partial^2 p_{ij}}{\partial x_i \partial x_j}[\phi] \end{aligned} \quad (4.19)$$

To obtain a convective wave equation, the identity in Eq. (4.16) is used to rewrite some of the terms in Eq. (4.19). After this,  $c_0^2 \frac{\partial^2 \rho'}{\partial x_i \partial x_i}[\phi]$  is subtracted from both sides to obtain the convective Ffowcs Williams-Hawkins equation for stationary, permeable surfaces

$$\square^2 \rho'[\phi] = \left( \frac{\partial}{\partial t} + U_{j,0} \frac{\partial}{\partial x_j} \right) Q[\phi] - \frac{\partial}{\partial x_i} L_i[\phi] + \frac{\partial^2}{\partial x_i \partial x_j} T_{ij}[\phi] \quad (4.20)$$

Here,  $\square^2$  is the convective wave operator,  $L_i[\phi]$  is a new source term, and  $T_{ij}[\phi]$  is the distribution generated by the Lighthill tensor

$$\begin{aligned}\square^2 &= \frac{\partial^2}{\partial t^2} + 2U_{j,0} \frac{\partial^2}{\partial x_j \partial t} + U_{i,0} U_{j,0} \frac{\partial^2}{\partial x_j \partial x_i} - c_0^2 \frac{\partial^2}{\partial x_i \partial x_i} \\ L_i[\phi] &= \int_t \int_{\partial V} (\rho u'_i (U_{j,0} + u'_j) + p' \delta_{ij} - \sigma_{ij}) n_j \phi dS dt \\ T_{ij}[\phi] &= (\rho u'_i u'_j + (p' - c_0^2 \rho') \delta_{ij} - \sigma_{ij}) [\phi]\end{aligned}\tag{4.21}$$

It is emphasized that all terms in Eq. (4.20) are distributions, i.e. they represent integrals of some field multiplied by a test function. This equation can also be written in functional form by only writing out the underlying fields

$$\begin{aligned}\square^2 [H(f)\rho'] &= \left( \frac{\partial}{\partial t} + U_{j,0} \frac{\partial}{\partial x_j} \right) \left[ \underbrace{(\rho(U_{0,i} + u'_i) - \rho_0 U_{i,0}) n_i}_{Q(\mathbf{x},t)} \delta(f) \right] \\ &\quad - \frac{\partial}{\partial x_i} \left[ \underbrace{(\rho u'_i (U_{j,0} + u'_j) + p' \delta_{ij} - \sigma_{ij}) n_j}_{L_i(\mathbf{x},t)} \delta(f) \right] \\ &\quad + \frac{\partial^2}{\partial x_i \partial x_j} [H(f) T_{ij}(\mathbf{x}, t)]\end{aligned}\tag{4.22}$$

The delta functions appearing in this expression comes from the fact that a surface integral may be rewritten as a volume integral over  $\mathbb{R}^3$  if the integrand is multiplied by  $\delta(f)$ , where  $f$  is a scalar field that is zero at the surface [22]. In Eq. (4.22), the functions corresponding to the distributions  $Q[\phi]$  and  $L_i[\phi]$  have also been defined. Equation (4.22) is equivalent to the convective Ffowcs Williams - Hawkings equation derived by Najafi-Yazidi et al. [78] if the integration surface is kept stationary in their equation. Equation (4.22) has also been derived earlier by Lockard [69] by performing a Galilean transformation of the original Ffowcs Williams - Hawkings equation.

## 4.2 Solution of the Convective Ffowcs Williams - Hawkings Equation

The solution to Eq. (4.22) is obtained by forming a convolution between the right hand side and a Green's function to the convective wave operator. If the ambient flow is

assumed to be aligned with the  $x_1$  axis, the Green's function becomes [78]

$$\begin{aligned}
G(\mathbf{x}, t) &= \begin{cases} \frac{\delta(t - R(\mathbf{x})/c_0)}{4\pi c_0^2 R^*(\mathbf{x})} & t > 0 \\ 0 & \text{else} \end{cases} \\
R(\mathbf{x}) &= \frac{-M_0 x_1 + R^*(\mathbf{x})}{\beta^2} \\
R^*(\mathbf{x}) &= \sqrt{x_1^2 + \beta^2(x_2^2 + x_3^2)} \\
\beta &= \sqrt{1 - M_0^2}
\end{aligned} \tag{4.23}$$

This Green's function represents the solution to the convective wave equation for the case when the right-hand side is a unit impulse in the origin at  $t = 0$ :  $\delta(\mathbf{x})\delta(t)$ . By examining the structure of Eq. (4.23), it can be seen that the response to this impulse is zero everywhere except when  $R(\mathbf{x}) = c_0 t$ . This condition is satisfied for all points on a sphere with radius  $r = c_0 t$  and center at  $x_1 = M_0 c_0 t$ , representing the fact that the sound impulse is convected downstream with the flow while at the same time traveling radially outwards relative to the flow.

The convolution between the right hand side of Eq. (4.22) and (4.23) reads as follows

$$\begin{aligned}
c_0^2 \rho'(\mathbf{x}, t) &= \left( \frac{\partial}{\partial t} + U_{1,0} \frac{\partial}{\partial x_1} \right) \int_{-\infty}^t \int_{\mathbb{R}^3} \frac{Q(\mathbf{y}, \tau) \delta(f(\mathbf{y})) \delta(t - \tau - R(\mathbf{x} - \mathbf{y})/c_0)}{4\pi R^*(\mathbf{x} - \mathbf{y})} d^3 \mathbf{y} d\tau \\
&\quad - \frac{\partial}{\partial x_i} \int_{-\infty}^t \int_{\mathbb{R}^3} \frac{L_i(\mathbf{y}, \tau) \delta(f(\mathbf{y})) \delta(t - \tau - R(\mathbf{x} - \mathbf{y})/c_0)}{4\pi R^*(\mathbf{x} - \mathbf{y})} d^3 \mathbf{y} d\tau \\
&\quad + \frac{\partial^2}{\partial x_i \partial x_j} \int_{-\infty}^t \int_{\mathbb{R}^3} \frac{H(f(\mathbf{y})) T_{ij}(\mathbf{y}, \tau) \delta(t - \tau - R(\mathbf{x} - \mathbf{y})/c_0)}{4\pi R^*(\mathbf{x} - \mathbf{y})} d^3 \mathbf{y} d\tau
\end{aligned} \tag{4.24}$$

Physically, the above equation expresses the density perturbation at position  $\mathbf{x}$  and time  $t$  as a function of the source terms at all positions  $\mathbf{y} \in \mathbb{R}^3$  and times  $\tau < t$ . The delta function will however restrict the integral at a position  $\mathbf{y}$  to be evaluated at a single time instant  $\tau_{\text{ret}} = t - R(\mathbf{x} - \mathbf{y})/c_0$ . If  $\mathbf{x}$  is taken to be the position of the observer, then  $\tau_{\text{ret}}$  represents the time when an acoustic signal generated at  $\mathbf{y}$  reaches the observer at time  $t$ . Although it is not obvious from the notation in Eq. (4.24), the presence of  $\delta(f)$  in the first two integrals will convert these volume integrals into a surface integral over  $\partial V$  [22]. Also, the third integral is only non-zero outside of  $\partial V$ . This last observation implies that, if  $\partial V$  is placed such that it encloses all relevant noise sources, then the third integral can be omitted. This simplification will be adopted for the remainder of this thesis.

The next thing that should be noted is that all derivatives are taken with respect to observer coordinates  $(\mathbf{x}, t)$ , and appear outside the integrals in Eq. (4.24). The fact that this is permissible, as opposed to differentiating  $Q(\mathbf{y}, \tau)\delta(f)$ ,  $L_i(\mathbf{y}, \tau)\delta(f)$  and  $H(f)T_{ij}(\mathbf{y}, \tau)$  before forming the convolution with the Green's function, was proven by Farassat [21]. We repeat the proof here for completeness. Let  $I_Q(\mathbf{x}, t)$ ,  $I_{L_i}(\mathbf{x}, t)$ , and  $I_{T_{ij}}(\mathbf{x}, t)$  respectively denote the first, second, and third integral on the right hand side of



Eq. (4.24). Clearly, these functions satisfy the following wave equations

$$\begin{aligned}\square^2 I_Q(\mathbf{x}, t) &= c_0^2 Q(\mathbf{x}, t) \delta(f) \\ \square^2 I_{L_i}(\mathbf{x}, t) &= c_0^2 L_i(\mathbf{x}, t) \delta(f) \\ \square^2 I_{T_{ij}}(\mathbf{x}, t) &= c_0^2 H(f) T_{ij}(\mathbf{x}, t)\end{aligned}\tag{4.25}$$

Based on this result, we can apply the convective wave operator to Eq. (4.24) to obtain

$$\begin{aligned}c_0^2 \square^2 \rho'(\mathbf{x}, t) &= \square^2 \left( \frac{\partial}{\partial t} + U_{1,0} \frac{\partial}{\partial x_1} \right) I_Q(\mathbf{x}, t) - \square^2 \frac{\partial}{\partial x_i} I_{L_i}(\mathbf{x}, t) + \square^2 \frac{\partial^2}{\partial x_i \partial x_j} I_{T_{ij}}(\mathbf{x}, t) \\ &= c_0^2 \left( \frac{\partial}{\partial t} + U_{1,0} \frac{\partial}{\partial x_1} \right) [Q(\mathbf{x}, t) \delta(f)] - c_0^2 \frac{\partial}{\partial x_i} [L_i(\mathbf{x}, t) \delta(f)] \\ &\quad + c_0^2 \frac{\partial^2}{\partial x_i \partial x_j} [H(f) T_{ij}(\mathbf{x}, t)]\end{aligned}\tag{4.26}$$

This shows that the density perturbation obtained from Eq. (4.24) indeed satisfies Eq. (4.22).

We now proceed by rewriting Eq. (4.24) in a form which is suitable for numerical implementations. The first step in this process is to change the order of integration, and then calculate the integral in  $\tau$

$$\begin{aligned}c_0^2 \rho'(\mathbf{x}, t) &= \left( \frac{\partial}{\partial t} + U_{1,0} \frac{\partial}{\partial x_1} \right) \int_{\mathbb{R}^3} \frac{Q(\mathbf{y}, \tau_{\text{ret}}) \delta(f(\mathbf{y}))}{4\pi R^*(\mathbf{x} - \mathbf{y})} d^3 \mathbf{y} \\ &\quad - \frac{\partial}{\partial x_i} \int_{\mathbb{R}^3} \frac{L_i(\mathbf{y}, \tau_{\text{ret}}) \delta(f(\mathbf{y}))}{4\pi R^*(\mathbf{x} - \mathbf{y})} d^3 \mathbf{y}\end{aligned}\tag{4.27}$$

All spatial derivatives can be moved inside the integrals in Eq. (4.27) since the integration boundary does not depend on  $\mathbf{x}$ . If  $h(\mathbf{y}, \tau_{\text{ret}})$  is used to denote either  $Q$  or  $L_i$ , this gives the following result

$$\begin{aligned}\frac{\partial}{\partial x_i} \left( \frac{h(\mathbf{y}, \tau_{\text{ret}})}{R^*} \right) &= - \frac{\dot{h}(\mathbf{y}, \tau_{\text{ret}})}{R^* c_0} \frac{\partial R}{\partial x_i} - \frac{h(\mathbf{y}, \tau_{\text{ret}})}{R^{*2}} \frac{\partial R^*}{\partial x_i} \\ &= - \frac{\dot{h}(\mathbf{y}, \tau_{\text{ret}}) \tilde{R}_i}{R^* c_0} - \frac{h(\mathbf{y}, \tau_{\text{ret}}) \tilde{R}_i^*}{R^{*2}}\end{aligned}\tag{4.28}$$

Here, a dot represents a partial derivative with respect to the retarded time  $\tau_{\text{ret}}$ . It should also be emphasized that the spatial dependency in the above equation was omitted for brevity, i.e.  $R = R(\mathbf{x} - \mathbf{y})$ . The new functions introduced in Eq. (4.28) are defined as [78]

$$\begin{aligned}\tilde{R}_1(\mathbf{x}) &= \frac{1}{\beta^2} \left( -M_0 + \tilde{R}_1^*(\mathbf{x}) \right), & \tilde{R}_2(\mathbf{x}) &= \frac{x_2}{R^*(\mathbf{x})}, & \tilde{R}_3(\mathbf{x}) &= \frac{x_3}{R^*(\mathbf{x})} \\ \tilde{R}_1^*(\mathbf{x}) &= \frac{x_1}{R^*(\mathbf{x})}, & \tilde{R}_2^*(\mathbf{x}) &= \beta^2 \frac{x_2}{R^*(\mathbf{x})}, & \tilde{R}_3^*(\mathbf{x}) &= \beta^2 \frac{x_3}{R^*(\mathbf{x})}\end{aligned}\tag{4.29}$$

Bringing the time derivative inside the integral is simpler, since it holds true that

$$\frac{\partial}{\partial t} h(\mathbf{y}, \tau_{\text{ret}}) = \dot{h}(\mathbf{y}, \tau_{\text{ret}}) \quad (4.30)$$

By introducing Eq. (4.28) and (4.30) into Eq. (4.27), we obtain

$$\begin{aligned} c_0^2 \rho'(\mathbf{x}, t) = & + \int_{\mathbb{R}^3} \frac{\dot{Q}(\mathbf{y}, \tau_{\text{ret}})(1 - M_0 \tilde{R}_1(\mathbf{x} - \mathbf{y}))}{4\pi R^*(\mathbf{x} - \mathbf{y})} \delta(f(\mathbf{y})) d^3 \mathbf{y} \\ & - \int_{\mathbb{R}^3} \frac{Q(\mathbf{y}, \tau_{\text{ret}}) U_{1,0} \tilde{R}_1^*(\mathbf{x} - \mathbf{y})}{4\pi R^{*2}(\mathbf{x} - \mathbf{y})} \delta(f(\mathbf{y})) d^3 \mathbf{y} \\ & + \int_{\mathbb{R}^3} \frac{1}{c_0} \frac{\dot{L}_i(\mathbf{y}, \tau_{\text{ret}}) \tilde{R}_i(\mathbf{x} - \mathbf{y})}{4\pi R^*(\mathbf{x} - \mathbf{y})} \delta(f(\mathbf{y})) d^3 \mathbf{y} \\ & + \int_{\mathbb{R}^3} \frac{L_i(\mathbf{y}, \tau_{\text{ret}}) \tilde{R}_i^*(\mathbf{x} - \mathbf{y})}{4\pi R^{*2}(\mathbf{x} - \mathbf{y})} \delta(f(\mathbf{y})) d^3 \mathbf{y} \end{aligned} \quad (4.31)$$

Finally, we rewrite the volume integral into a surface integral, rearrange some terms slightly, and assume that at the observer, the isentropic relation  $p'(\mathbf{x}, t) = c_0^2 \rho'(\mathbf{x}, t)$  holds. This gives us the following result

$$\begin{aligned} p'_{\text{obs}}(\mathbf{x}, t) = & + \int_{\partial V} \frac{\dot{Q}(\mathbf{y}, \tau_{\text{ret}}) R(\mathbf{x} - \mathbf{y})}{4\pi R^{*2}(\mathbf{x} - \mathbf{y})} dS - \int_{\partial V} \frac{Q(\mathbf{y}, \tau_{\text{ret}}) U_{1,0} \tilde{R}_1^*(\mathbf{x} - \mathbf{y})}{4\pi R^{*2}(\mathbf{x} - \mathbf{y})} dS \\ & + \int_{\partial V} \frac{1}{c_0} \frac{\dot{L}_i(\mathbf{y}, \tau_{\text{ret}}) \tilde{R}_i(\mathbf{x} - \mathbf{y})}{4\pi R^*(\mathbf{x} - \mathbf{y})} dS + \int_{\partial V} \frac{L_i(\mathbf{y}, \tau_{\text{ret}}) \tilde{R}_i^*(\mathbf{x} - \mathbf{y})}{4\pi R^{*2}(\mathbf{x} - \mathbf{y})} dS \end{aligned} \quad (4.32)$$

Note that all integrals in this expression should be evaluated with respect to  $\mathbf{y}$ .

### 4.3 Implementation of Convective Ffowcs Williams - Hawkings Equation

A major goal of the present work was to develop a computational framework for predicting the noise generated by a Counter Rotating Open Rotor (CROR). The final framework that was developed is based on first computing the unsteady flow field in the vicinity of the CROR using the Harmonic Balance method. In the next step, the noise at an arbitrary distance from the CROR is obtained by evaluating the integral in Eq. (4.32), using the Harmonic Balance solution computed earlier as input. The latter step will be detailed next.

The integral in Eq. (4.32) is evaluated using the source time dominant algorithm [5]. In this algorithm,  $\tau_{\text{ret}}$  is kept constant when the integral in Eq. (4.32) is evaluated. The contribution from each surface element is then added to the observer pressure signal at the following time-step

$$t = \tau_{\text{ret}} + \frac{R(\mathbf{x} - \mathbf{y})}{c_0} \quad (4.33)$$

All surface elements are generally not located at the same distance from the observer. As a consequence of this, a single iteration of the source time dominant algorithm will give a small contribution to a large set of observer time instances. The complete observer signal must thus be built up over several iterations, i.e., by evaluating Eq. (4.32) at enough source time instances to obtain a complete pressure signal at the observer. It should also be noted that, since  $t$  in Eq. (4.33) rarely will coincide with the discrete time-instances stored at the observer, linear interpolation is used to interpolate the contribution of each surface element onto the two nearest observer time instances.

A method similar to the one proposed by Sharma et al. [94] has been adopted to interpolate the Harmonic Balance solution onto the integration surface used in Eq. (4.32). In this method, the Harmonic Balance solution is extracted on surfaces in front of, above, and behind the rotor blades (see Fig. 4.2). The interpolated solution is then copied, rotated, and phase-shifted (using Eq. (3.18)) to obtain the flow field on a surface that covers the whole circumference. Note that this latter step must be performed since the Harmonic Balance simulation uses the phase-shifted periodic boundary conditions described in section 3.1, and therefore only contains one blade per row. It should also be noted that the new surface obtained will miss the parts of the end caps where the hub of the CROR is situated. In the present work, these missing surfaces are neglected in the analysis. This approximation has also been adopted by other authors [97, 94], and implies that the effect of the hub is neglected.

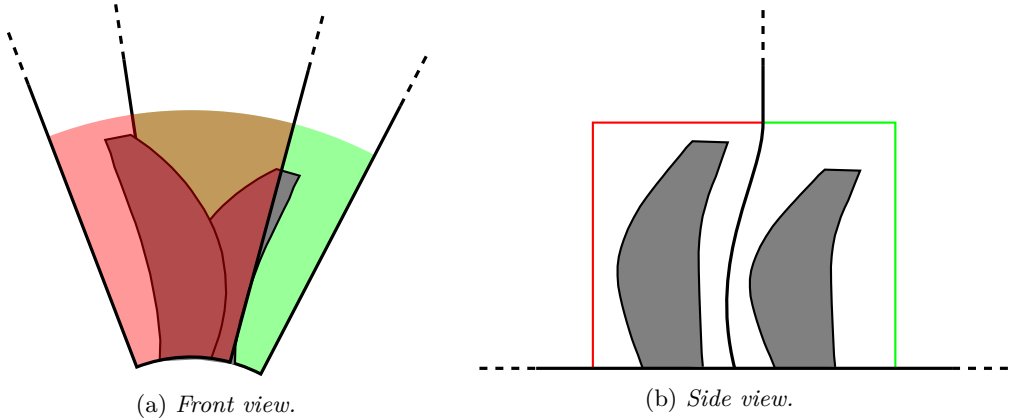


Figure 4.2: *Illustration of surfaces used to extract data from the Harmonic Balance simulation.*

In each iteration of the source time dominant algorithm, the interpolated solution obtained in the previous step is rotated according to the rotational speed of the corresponding blade row. This step is necessary since the Harmonic Balance solution is computed in a rotating frame of reference, whereas the input to Eq. (4.32) assumes that the solution is expressed in an inertial frame of reference. After the solution has been rotated, it must also be interpolated in time to obtain the conserved variables at the

current source time-step. This is easily achieved as follows

$$q(\tau_{\text{ret}}) = \mathbf{E}_{\Lambda}^{-1}(\tau_{\text{ret}})\mathbf{E}_{\Lambda}(\mathbf{t})\mathbf{q}^* \quad (4.34)$$

Here,  $\mathbf{E}_{\Lambda}^{-1}(\tau_{\text{ret}})$  only contains a single row, corresponding to the inverse discrete Fourier transform evaluated at  $\tau_{\text{ret}}$ .

Once the solution has been rotated and interpolated in time, it is converted to primitive flow variables in the absolute frame of reference. After this, the free stream velocity is subtracted from the velocity vector, and the resulting flow field is then finally interpolated onto the stationary grid used to evaluate Eq. (4.32). It should also be noted that temporal derivatives in Eq. (4.32) are evaluated using a fourth-order backward-difference scheme.

## 5 Summary of Papers

This chapter contains a brief description of each paper that is appended to this thesis.

### 5.1 Paper A

D. Lindblad and N. Andersson. “Validating the Harmonic Balance Method for Turbomachinery Tonal Noise Predictions”. 55th AIAA Aerospace Sciences Meeting (Grapevine, TX, Jan. 9–13, 2017). AIAA Paper 2017-1171. DOI: 10.2514/6.2017-1171

#### Motivation and Background

At the beginning of the Ph.D. project reported in this thesis, the Harmonic Balance method was implemented into the G3D::Flow code. The purpose of Paper A was to validate this implementation on two test cases from the Fourth Computational Aeroacoustics Workshop on Benchmark Problems, hosted by NASA. In the first test case, known as the “Single Airfoil Gust Response Problem”, the acoustic response of an isolated airfoil that is subjected to a vortical velocity gust is computed [92]. The second test case is further known as the “Cascade-Gust Interaction Problem”, and is based on computing the acoustic response of a two-dimensional cascade of outlet guide vanes (OGVs) that is subjected to a vortical velocity gust [17].

#### Work and Results

The Harmonic Balance solver and the phase-shifted periodic boundary condition used in Paper A were implemented by the author of this thesis. Valuable input on the implementation, including guidance on how to integrate the new features with the rest of the G3D::Flow code, was provided by Niklas Andersson. In G3D::Flow, explicit pseudo-time integration is mainly used to solve steady problems. To reuse as much code as possible, it was decided to use explicit pseudo-time integration for the Harmonic Balance solver as well. It was known by the authors at the time of writing Paper A that this could give rise to stability problems. In an attempt to avoid these problems, the point implicit Runge-Kutta (PIRK) technique proposed by Campobasso et al. [6] was implemented. Unfortunately, stability problems were still encountered when working on Paper A. For this reason, it was decided to use a fully explicit treatment of the Harmonic Balance source term in all future works.

In general, the results obtained with G3D::Flow compared very well with results published by other authors. In particular, none of the codes that were compared stood out from the rest. This shows that, at least for the test cases considered, the Harmonic Balance solver in G3D::Flow gives comparable results to well-established codes such as GUST3D [91], BASS [43], and HYDRA/HYDLIN [9].

The results reported in Paper A also showed that a one dimensional, nonreflecting boundary condition was insufficient for the Cascade Gust Interaction Problem. To partly remedy this issue, the computational domain was extended significantly downstream, and

a sponge layer was added upstream of the outlet to damp out any fluctuations. Although this improved the results considerably, the need for higher-order nonreflecting boundary conditions became apparent from working on Paper A.

All results published in Paper A were produced by the author of this thesis. The manuscript was also written by the author of this thesis. Valuable input on both results and the writing was provided by Niklas Andersson.

## Comments

The work in Paper A inspired much of the work that was performed for the remainder of this thesis. In particular, the stability problems encountered in Paper A inspired the work reported in Paper E, where a linear stability analysis was used to derive a new preconditioner for the Harmonic Balance solver. The reflections that occurred for the second test case further inspired the work on nonreflecting boundary conditions reported in Paper C. After learning more about the Harmonic Balance method from working on Paper A, it was also realized that aliasing might become a problem. This was one of the motivations for the work reported in Paper F.

## 5.2 Paper B

D. Lindblad, G. Montero Villar, N. Andersson, A. Capitao Patrao, S.-k. Courty-Audren, and G. Napias. “Aeroacoustic Analysis of a Counter Rotating Open Rotor based on the Harmonic Balance Method”. 2018 AIAA Aerospace Sciences Meeting (Kissimmee, FL, Jan. 8–12, 2018). AIAA Paper 2018-1004. DOI: 10.2514/6.2018-1004

### Motivation and Background

The purpose of Paper B was to develop and demonstrate a complete framework for predicting the tonal noise generated by a Counter Rotating Open Rotor (CROR). To accomplish this, several problems had to be solved. To begin with, a representative CROR geometry was needed. After this, a high-quality structured mesh that would satisfy the needs for a computational aeroacoustics simulation had to be developed. With regards to CFD, no blade row interface that could be used with the Harmonic Balance solver was available in G3D::Flow, and therefore had to be implemented. In addition to this, a suitable acoustic analogy was needed to calculate the far-field acoustic signature of the CROR.

### Work and Results

The work reported in Paper B was performed in collaboration with ISAE-SUPAERO in Toulouse. To begin with, Alexandre Capitao Patrao at Chalmers designed a CROR geometry based on data available in the public literature. After this, the people at ISAE-SUPAERO designed a high-quality block-structured mesh. The author of this thesis implemented a Fourier-based blade-row interface in G3D::Flow together with Gonzalo Montero Villar. The author of this thesis also implemented and validated the chosen acoustic analogy using Python, ran all simulations, and post-processed the results. All authors contributed when writing the final manuscript.

The aforementioned framework was used in Paper B to compute the noise generated by the newly designed CROR in cruise. This operating point is not as important as the take-off condition from a noise perspective. Performing a simulation in take-off was however not possible within the time frame allocated for Paper B. This is because the CROR geometry likely would have needed further improvements to perform well in take-off, where the blades are highly loaded. Despite this, many interesting results could be obtained for the cruise condition. To begin with, it was found that the Harmonic Balance method is very convenient to use. In particular, the fact that the entire time-period is stored makes it easy to monitor convergence, and to couple the solution with an acoustic analogy.

Another interesting finding in Paper B was that spurious noise is generated when rotor wakes cross the downstream integration surface used by the acoustic analogy. This problem is known to occur when the volume integral is omitted and a porous surface is used to solve the Ffowcs Williams - Hawkins equation [23]. Unfortunately, no time was available within the scope of this thesis to investigate the problem further.

## Comments

It is important to note that no experimental data, nor any numerical results from other authors, were available for the CROR geometry used in Paper B. It was therefore impossible to validate the noise prediction framework presented in Paper B. Access to reference data would however not solve the validation problem in itself. This is because the noise prediction framework presented in Paper B contains several different modeling assumptions. From this, it follows that the results obtained by the noise prediction framework more than likely would have deviated from any reference data. To minimize this deviation, each modeling aspect would have to be evaluated. This is a time-consuming process that would have been hard to complete within the time frame allocated for Paper B.

Another comment should be made about the acoustic analogy. In Paper B, the convective Ffowcs Williams - Hawkings equation presented in section 4.1 was solved in the time-domain (see section 4.3 for details). Although the time-domain implementation is relatively simple and intuitive, it is not believed to be the optimal one. In particular, it can be noted that the Harmonic Balance method only resolves a selected number of frequencies in each blade row. These frequencies are in turn generated by circumferential variations of the flow in the adjacent blade row, c.f. Eq. (3.44). Therefore, it would be advantageous to filter the solution before performing the noise propagation step, such that all flow perturbations that correspond to time-azimuthal Fourier coefficients which are not resolved in both blade rows, are removed from the solution. This is not done in the present work, but could be easily achieved with the frequency domain formulation of the convective Ffowcs Williams - Hawkings equation presented in [102]. Applying this formulation could also help in reducing the amount of spurious noise generated by sharp wakes crossing the integration surface.



## 5.3 Paper C

D. Lindblad, N. A. Wukie, G. Montero Villar, and N. Andersson. “A Nonreflecting Formulation for Turbomachinery Boundaries and Blade Row Interfaces”. 2019 AIAA Aerospace Sciences Meeting (San Diego, CA, Jan. 7–11, 2019). AIAA Paper 2019-1804. DOI: 10.2514/6.2019-1804

### Motivation and Background

The results reported in Paper A indicated that higher-order nonreflecting boundary conditions were needed to get accurate predictions of turbomachinery tonal noise. After reviewing the literature, it became clear that the exact, nonlocal, nonreflecting boundary condition for a single Fourier mode developed by Giles [34, 33] and Hall et al. [37] was a popular choice for this purpose. It was therefore decided to implement this boundary condition into the G3D::Flow code. The initial implementation was reported in [67], and was based on the Fourier-based blade-row interface reported in Paper B. After reviewing the implementation, it became apparent that the implementation would not work well for inlet/outlet boundaries. It was therefore decided to perform a second implementation, which would be applicable to both boundaries and interfaces. The results of this effort were reported in Paper C.

### Work and Results

The work reported in Paper C was done in close collaboration with Nathan Wukie, who visited Chalmers during the spring of 2018. The author of this thesis derived the mathematical formulation for the nonreflecting boundary condition. Valuable input on the formulation was provided by Nathan Wukie. Together with Gonzalo Montero Villar, the author of this thesis then implemented the boundary condition into the G3D::Flow code. Nathan Wukie also implemented the boundary condition into his CFD code, see [106]. With great support from all authors of Paper C, the author of this thesis wrote the manuscript.

As noted previously, different flavors of the nonreflecting boundary condition considered in Paper C have already been adopted by many authors. The main contribution of Paper C is therefore not the application of the boundary condition, but rather the extensive analysis behind it that is provided in the paper. In particular, great care was put into every part of the derivation to ensure that the formulation would work for both steady simulations, as well as unsteady simulations using the Harmonic Balance method. The regularization proposed by Frey et al. [28] was also adopted to avoid problems with acoustic resonance. The stability problem associated with the boundary condition was also partly addressed in Paper C.

### Comments

Although the work reported in Paper C constitutes a great improvement over the original work reported in [67], it still should be seen as a work in progress. For a complete reference

on the nonreflecting boundary condition, the reader should consult section 3.2 in this thesis.

## 5.4 Paper D

N. A. Wukie, D. Lindblad, and N. Andersson. “noisyduck: an open-source Python tool for computing eigenmode decompositions of duct flows”. 25<sup>th</sup> AIAA/CEAS Aeroacoustics Conference (Delft, The Netherlands, May 20–23, 2019). AIAA Paper 2019-2418. DOI: 10.2514/6.2019-2418

### Motivation and Background

Propagation of flow disturbances in ducts is an important aspect of turbomachinery aeroacoustics. To understand how these disturbances propagate, they can be decomposed into elementary modes, called duct-modes. A common approach for computing these duct-modes is to employ a normal mode analysis of the linearized Euler equations. After reviewing the literature, it became apparent that the numerical implementation strategy, as well as the exact form of the governing equations, differed between different publications. Based on this observation, it was decided to create a well documented, open-source tool for computing duct-modes. The result of this effort is the **noisyduck** code, which is described in Paper D.

### Work and Results

Nathan Wukie initiated the work reported in Paper D. In particular, Nathan selected the numerical methodology, wrote the implementation in Python, and published **noisyduck** open-source on GitHub. The author of this thesis derived the linearized Euler equations that are implemented in **noisyduck**. The author of this thesis also contributed by writing the part of the paper that details the derivation of the linearized Euler equations. The rest of the paper was written by Nathan Wukie.

Paper D presents a thorough derivation of the linearized Euler equations used in **noisyduck**. These equations appear to be the most widely adopted ones for analyzing duct-modes, and the derivation provided in Paper D should therefore be a valuable reference for researchers in the field of turbomachinery aeroacoustics. The numerical methodology implemented in **noisyduck** is also detailed in Paper D, which hopefully will help researchers who are interested in adopting the tool to understand it.

The results obtained with **noisyduck** compared well to both analytical solutions, as well as to numerical results published by other authors. Some differences could however be observed, especially when the results from **noisyduck** were compared to other numerical results. The cause of this discrepancy is hard to point out, given that all details on how the reference results were obtained are not known. This also highlights the value of open-source. If researchers are interested in comparing their results to **noisyduck**, they have access to both the source code and examples of how to use it on GitHub.

### Comments

After Paper D was published, it was discovered that the mean flow used in one of the test cases was not homentropic, as stated in the paper. This error has since then been

corrected, and an updated test case is published on GitHub. Unfortunately, correcting this error did not help in reducing the discrepancy between the results obtained with `noisyduck`, and the reference data. For more details on this, see Appendix C.

## 5.5 Paper E

D. Lindblad and N. Andersson. Convergence Acceleration of the Harmonic Balance Method using a Time-Level Preconditioner. *AIAA Journal* (in press)

### Motivation and Background

The Harmonic Balance method is today widely used to simulate time-periodic flows in various applications. The Harmonic Balance form of the governing equations is commonly solved using either explicit or implicit pseudo-time integration schemes. In G3D::Flow, explicit pseudo-time integration is used for steady-state calculations. To reuse as much code as possible, it was decided to employ the same strategy in the Harmonic Balance solver. From the literature, it is well known that this can lead to stability problems. In an attempt to overcome this issue, the point implicit Runge-Kutta (PIRK) method proposed in [6] was implemented in G3D::Flow. Unfortunately, this did not ensure convergence, despite choosing a CFL number which would normally work in a steady-state simulation. This motivated further work on improving the stability of the Harmonic Balance solver in G3D::Flow. The results of this work are reported in Paper E.

### Work and Results

Several authors have investigated under which conditions pseudo-time integration of the Harmonic Balance equations is stable. This has been done both from a theoretical point of view, using a von Neumann stability analysis, and from a practical point of view, using numerical experiments. In Paper E, a review of these research efforts is presented. This review shows that theoretical and numerical investigations generally reach the same conclusion regarding stability. The review also shows that several different strategies, including the PIRK approach mentioned earlier, have been proposed for stabilizing explicit pseudo-time integration of the Harmonic Balance equations. Unfortunately, most of these approaches have not been extensively evaluated yet. In Paper E, a von Neumann stability analysis was therefore performed for some of these stabilization approaches. This analysis showed that the most reliable method for stabilizing the Harmonic Balance solver is to restrict the pseudo-time-step in each cell based on the local grid reduced frequency. Existing approaches for doing this are however quite conservative, and therefore sub-optimal from a convergence point of view. This inspired development of the time-level preconditioner presented in Paper E (see section 2.4 for details).

### Comments

Although the preconditioner proposed in Paper E is close to optimal from a theoretical point of view, its practical advantage over earlier approaches that reduce the pseudo-time-step based on the grid reduced frequency is rather limited. More details on this are provided in Paper E.

## 5.6 Paper F

D. Lindblad, C. Frey, L. Junge, G. Ashcroft, and N. Andersson. Minimizing Aliasing in Multiple Frequency Harmonic Balance Computations. *Journal of Scientific Computing* (submitted)

### Motivation and Background

An important property of the Harmonic Balance method is that it can be applied to nonlinear equations. In general, solutions to nonlinear equations can contain an infinite number of frequencies. Unfortunately, only a limited number of these frequencies can be accounted for by the discrete Fourier transform used in the Harmonic Balance method. The remaining frequencies will instead contaminate the resolved ones. This phenomenon, known as aliasing, reduces the accuracy of the solution and can, in the worst case, prevent the solver from converging.

Aliasing can be controlled by carefully selecting the time samples used in the discrete Fourier transform. For problems that contain a single fundamental frequency and its harmonics, the time samples are commonly distributed uniformly between 0 and the reciprocal of the fundamental frequency. For problems that contain multiple fundamental frequencies, on the other hand, a non-uniform time sampling that minimizes the condition number of the discrete Fourier transform matrices is often used. For both single and multiple frequency problems, oversampling can also be used to further reduce aliasing.

After reading about time sampling approaches for single and multiple frequency problems, it was not clear to the authors of Paper F why a uniform time sampling always was used for single frequency problems. In addition to this, it was not clear why the condition number was the right metric for selecting a time sampling in a multiple frequency problem. Finally, since oversampling does not lead to a uniquely defined discrete Fourier transform pair (see section 2.2.1 for details), the authors of Paper F were interested in how oversampling should be done optimally.

### Work and Results

The work reported in Paper F was done in close collaboration with the people at the numerical methods department at the German Aerospace Center (DLR) in Cologne. In particular, Laura Junge introduced the author of this thesis to multiple frequency problems and the almost periodic Fourier transform. Graham Ashcroft suggested the topic and arranged for the author of this thesis to visit DLR during the spring of 2019. Christian Frey helped the author of this thesis a lot by sharing his extensive knowledge in mathematics, helped planning the work, and also proposed the alias operator presented in section 2.1. The author of this thesis conducted most of the simulations presented in the paper. With great support from the remaining authors, the author of this thesis also wrote the paper.

The results presented in Paper F suggest that a uniform time sampling is the optimal choice for problems that contain a single fundamental frequency. The results also suggest that the condition number is the right metric for choosing a time sampling for the

multiple frequency problem. It can therefore be concluded that there is no need to change established approaches for choosing a time sampling, provided that oversampling is not used. If oversampling, on the other hand, is employed, the situation becomes more complicated. To this date, no final recipe for constructing the discrete Fourier transform pair for the multiple frequency problem has been developed. The results presented in Paper F do however suggest that the Moore-Penrose is not necessarily the optimal choice. Instead, it might be advantageous to use the left inverse defined in section 2.2.1.

## Comments

Paper F presents a combined theoretical/numerical investigation of how aliasing occurs in Harmonic Balance computations. The theoretical results, which are mainly based on the alias operator, correspond well with numerical results obtained on the Duffing oscillator. A perfect correlation between the norm of the alias operator, and the amount of aliasing obtained in a Harmonic Balance computation, was however not achieved. This is expected since the alias operator expresses the maximal amount of aliasing that a discrete Fourier transform can produce. The numerical alias error is on the other hand accumulated during the iterative solution process since the discrete Fourier transform is employed once per iteration. Therefore, one can run into situations when the alias errors introduced in different iterations cancel each other, leading to a small accumulated error, despite the fact that each Fourier transform produces a large error. More challenging problems, such as the spatially discretized Favre-Averaged Navier-Stokes equations, also remain to be investigated.

## 6 Concluding Remarks

This thesis has investigated some numerical methods that can be used for predicting turbomachinery tonal noise. These methods can be divided into two categories. The first category contains methods which can be used for computing noise sources based on CFD. It includes the time-domain Harmonic Balance method [38] and the exact, nonlocal, nonreflecting boundary condition developed by Giles [34, 33] and Hall et al. [37]. The second category contains methods which are devoted to noise propagation, and includes the convective Ffowcs Williams - Hawkings equation for permeable surfaces introduced by Najafi-Yazidi et al. [78] and a tool for computing duct modes. The lessons learned from working on these methods will be summarized in the following paragraphs.

**Harmonic Balance Method** The Harmonic Balance method can be used to construct a high-order approximation of the time derivative term if the spectral content of the solution can be estimated in advance. Both the time-domain and the frequency-domain formulation of the Harmonic Balance method have been considered in this thesis.

From a practical point of view, the time-domain Harmonic Balance method is very attractive since it is easy to implement into an existing CFD solver. This statement is mainly based on the author's experience with the G3D::Flow code, that uses explicit pseudo-time integration to solve the Harmonic Balance equations. If an implicit approach on the other hand is used, a large linear system must be constructed, which requires additional storage and is expensive to solve. A fully implicit scheme can however be made unconditionally stable, which enables large pseudo-time steps to be used.

Stability problems can occur when explicit pseudo-time integration is used to solve the Harmonic Balance equations. This is a well-known problem, that was investigated using a von Neumann stability analysis in this thesis. The stability analysis showed that the temporal discretization introduced by the Harmonic Balance method moves the eigenvalue spectra of the spatial discretization along the imaginary axis. This explains why an explicit pseudo-time integration scheme, which has a limited stability region in the complex plane, can diverge when the Harmonic Balance equations are solved. The stability analysis used in this work was also used in Paper E to assess some stabilization approaches proposed in the literature (see [62] for details). In the future, it would be interesting to investigate other stabilization approaches. It would also be interesting to investigate how methods such as implicit residual smoothing would affect stability and convergence. I believe that the theory presented in this work is well suited for these purposes.

Based on knowledge gained from the stability analysis, a novel preconditioner for the time-domain Harmonic Balance method was derived. This preconditioner scales the pseudo-time-step with which each frequency component in the solution is updated, such that the solver remains stable. When this preconditioner is used, the solver converged in fewer iterations compared to when other stabilization approaches were employed. The wall-clock time was however not significantly reduced since the preconditioner is relatively expensive to use. It is therefore suggested to use a simpler stabilization approach, such as the pseudo-time step restriction proposed by Weide et al. [103], when explicit pseudo-time



integration is used to solve the Harmonic Balance equations. If multi-grid is used, the preconditioner proposed in this work might be more valuable, see Paper E for details [62].

It is well-known that aliasing can occur when the Harmonic Balance method is applied to nonlinear equations. In this work, the alias error was quantified by introducing an operator that describes how Fourier coefficients that correspond to unresolved frequencies fold back (alias) onto the resolved ones. The norm of this operator is also shown to provide an a-priori bound on aliasing. This operator can therefore be used to estimate the amount of aliasing that a particular time sampling causes. In Paper F, it was found that a uniform time sampling is optimal for the single frequency case, whereas a non-uniform time sampling that minimizes the condition number of the discrete Fourier transform is optimal for the multiple frequency case. This confirms that the most widely adopted approaches for selecting a time sampling in both cases indeed are the right ones. Note that this statement only holds when oversampling is not used. In this work, a new oversampling strategy has therefore been developed for the multiple frequency case. This strategy appears to give less aliasing than other approaches, but more work is needed to confirm this.

**Nonreflecting Boundary Conditions** The exact, nonlocal, nonreflecting boundary condition for a single Fourier mode developed by Giles [34, 33] and Hall et al. [37] has been considered in this work. This boundary condition ensures that all waves that satisfy the two-dimensional, linearized Euler equations, can exit the computational domain without being reflected. This does in turn enable the inlet/outlet boundaries to be placed closer to the blades, leading to a smaller computational domain.

The nonreflecting boundary condition considered in this thesis was originally developed in the 1980's. Since then, different flavors of the boundary condition have been used by many authors. The purpose of this thesis was to construct the most generic formulation of the boundary condition possible. It is believed that this goal was achieved. In particular, the formulation presented in this thesis can be applied to both steady-state simulations and to unsteady simulations. It also avoids problems associated with acoustic resonance by including the regularization proposed by Frey et al. [28]. It should be noted that the formulation employed in this work previously was proposed by Kersken et al. [51].

Two numerical implementation strategies of the nonreflecting boundary condition were evaluated in this work. In the first implementation strategy, the boundary condition is enforced directly. This approach has previously been reported to cause numerical instabilities [29, 51]. The second implementation strategy is based on reformulating the boundary condition in terms of characteristic variables, as originally proposed by Giles [33]. This strategy is more involved than the first one, but has been reported to be more numerically stable than the first one. In this work, both implementation strategies were found to be numerically stable. Despite this, it is suggested that the second implementation strategy is used. It is also suggested that the solution first is extrapolated to the boundary, then converted to characteristic variables, and finally Fourier transformed, before Eq. (3.56) is used to calculate a new boundary state for the next iteration. For more details on this, see section 3.2.3.

In both implementation strategies, unresolved Fourier coefficients are treated with a one-dimensional nonreflecting boundary condition based on characteristic variables,

as originally proposed in [106]. This additional step is believed to improve the stability of the solver. In fact, when the boundary condition is imposed according to Eq. (3.56) (second implementation strategy), all unresolved Fourier coefficients are implicitly treated with a nonreflecting boundary condition based on characteristic variables. This could explain why other authors have reported that the second implementation strategy is more stable than the first one. This hypothesis is further strengthened by the fact that the first implementation strategy was found to be numerically stable when the unresolved Fourier coefficients were treated with the one-dimensional boundary condition. As noted previously, however, it is the author's opinion that the second implementation strategy is the best one, if it is implemented in such a way that  $\hat{c}_{n,k,c}$  are calculated from the extrapolated characteristic variables. This approach has previously been used in [51].

**Duct Modes** A small part of this thesis was devoted to duct modes. Duct modes describe how flow perturbations propagate inside ducts. This makes them useful for post processing numerical simulations, or for constructing higher-order nonreflecting boundary conditions. Calculating the duct modes is however not a trivial task. In the present work, a normal mode analysis was used for this purpose. Although this method is relatively simple to use, the duct modes obtained from it probably do not give a complete representation of the flow. In particular, the normal mode analysis assumes that the flow disturbances vary harmonically in the axial direction. No mathematical or physical justification for this assumption has been found in the literature, which raises questions regarding its validity.

The main outcome of this work is an open-source tool for computing duct modes based on a normal mode analysis, called `noisyduck` [105]. The validation of `noisyduck` presented in this thesis showed that the code compares well with previously published results. It is the hope of the author that the theory presented in this thesis, the official publication [105], the documentation available on GitHub, and the source-code itself, will be useful for people who wish to work on duct modes in the future.

**Noise propagation based on Ffowcs Williams - Hawkings Equation** The Ffowcs Williams - Hawkings equation is an inhomogeneous wave equation, in which the right hand side contains all sources of sound that moving surfaces and a turbulent flow field can generate [24]. This equation can be formally solved with a free-space Green's function, to obtain the noise at an observer as a function of the noise sources. The formal solution is however not suitable for numerical implementation, and several reformulations have therefore been proposed in the literature. In this work, Formulation 1C by Najafi-Yazidi et al. [78], which is similar to Formulation 1A by Farassat [21], has been used. Formulation 1C expresses the noise at the observer as a surface integral over a closed surface, plus a volume integral over the volume exterior to the surface. In this work, the volume integral is neglected. This assumption is justified as long as the surface is chosen large enough to enclose all noise sources [26].

Formulation 1C was chosen since it includes the effects that a uniform mean flow has on noise propagation. It is therefore directly applicable to wind tunnel problems, i.e., problems when the noise relative to an engine in forward flight is of interest. In this work, Formulation 1C was used to compute the far-field acoustic signature of a

counter rotating open rotor (CROR). The surface integral was evaluated by extracting data from a CFD simulation based on the time-domain Harmonic Balance method. This combination proved to be very convenient, especially when used together with the forward time algorithm [5]. For wind-tunnel problems, Formulation 1C [78] is therefore highly recommended.

Unfortunately, spurious noise was generated when the wakes of the CROR crossed the downstream integration surface. This is a problem that is known to occur when a porous surface is used to define the noise sources [23]. No solution to this problem was found in this thesis. An interesting approach that might be able to solve the problem was proposed in [102].

**Final Comment** Among all the things that I have learned from working on this thesis, one thing stands out: never overlook a single detail, because *"Det finns inga genvägar fram till det perfekta ljudet"* (English: *"There are no shortcuts when you want to obtain the perfect sound"*)<sup>1</sup>.

---

<sup>1</sup>This is a famous quote by Farbror Barbro, a character in the Swedish TV series "NileCity 105,6"

# References

- [1] Advisory Council for Aviation Research and Innovation in Europe. *Strategic Research and Innovation Agenda - 2017 Update - Volume 1*. Accessed online at <https://www.acare4europe.org/sria> (2020-06-29). Advisory Council for Aviation Research and Innovation in Europe, 2017.
- [2] Airbus S.A.S. *Global Market Forecast 2019-2038*. Accessed online at [www.airbus.com](http://www.airbus.com) (2020-06-29). AIRBUS S.A.S., 2019. ISBN: 978-2-9554382-4-6.
- [3] N. Andersson. “A Study of Subsonic Turbulent Jets and Their Radiated Sound Using Large-Eddy Simulation”. PhD thesis. Gothenburg, Sweden: Division of Fluid Dynamics, Department of Applied Mechanics, Chalmers University of Technology, 2005. ISBN: 91-7291-679-6.
- [4] G. Ashcroft et al. Advanced Numerical Methods for the Prediction of Tonal Noise in Turbomachinery — Part I: Implicit Runge–Kutta Schemes. *Journal of Turbomachinery* **136.2** (Feb. 2014), 02-1002-1-021002–9. DOI: 10.1115/1.4023904.
- [5] K. S. Brentner and F. Farassat. Modeling aerodynamically generated sound of helicopter rotors. *Progress in Aerospace Sciences* **39.2-3** (Feb. 2003), 83–120. DOI: 10.1016/S0376-0421(02)00068-4.
- [6] M. S. Campobasso and M. H. Baba-Ahmadi. Analysis of Unsteady Flows Past Horizontal Axis Wind Turbine Airfoils Based on Harmonic Balance Compressible Navier-Stokes Equations With Low-Speed Preconditioning. *Journal of Turbomachinery* **134.6** (Nov. 2012), 061020-1-011001–13. DOI: 10.1115/1.4006293.
- [7] A. Capitao Patrao et al. “Aerodynamic and aeroacoustic comparison of optimized high-speed propeller blades”. 2018 AIAA Joint Propulsion Conference (Cincinnati, OH, July 9–11, 2018). AIAA Paper 2018-4658. DOI: 10.2514/6.2018-4658.
- [8] Y. Colin et al. “Computational strategy for predicting CROR noise at low-speed Part II: Investigation of the Noise Sources Computation with the Chorochronic Approach”. 18th AIAA/CEAS Aeroacoustics Conference (Colorado Springs, CO, June 4–6, 2012). AIAA Paper 2012-2222. DOI: 10.2514/6.2012-2222.
- [9] J. Coupland. “Linear Unsteady CFD Analysis of the Cascade-Gust Interaction Problem”. *Fourth Computational Aeroacoustics (CAA) Workshop on Benchmark Problems*. Ed. by M. D. Dahl. NASA/CP-2004-212954. Sept. 2004, pp. 97–105.
- [10] J. Crespo, R. Corral, and J. Pueblas. An Implicit Harmonic Balance Method in Graphics Processing Units for Oscillating Blades. *Journal of Turbomachinery* **138.3** (Nov. 2015), 31001-1-031001–10. DOI: 10.1115/1.4031918.
- [11] N. Curle. The Influence of Solid Boundaries upon Aerodynamic Sound. *Proceedings of the Royal Society of London. Series A, Mathematical and Physical Sciences* **231.1187** (Sept. 1955), 505–514. DOI: 10.1098/rspa.1955.0191.
- [12] L. Debnath and P. Mikusiński. *Introduction to Hilbert Spaces. With Applications*. 3rd ed. Academic Press, Sept. 2005. ISBN: 9780122084386.
- [13] K. Ekici and K. C. Hall. Nonlinear Analysis of Unsteady Flows in Multistage Turbomachines Using Harmonic Balance. *AIAA Journal* **45.5** (May 2007), 1047–1057. DOI: 10.2514/1.22888.

- [14] K. Ekici and K. C. Hall. Nonlinear Frequency-Domain Analysis of Unsteady Flows in Turbomachinery with Multiple Excitation Frequencies. *AIAA Journal* **46.8** (Aug. 2008), 1912–1920. DOI: 10.2514/1.26006.
- [15] K. Ekici, K. C. Hall, and E. H. Dowell. Computationally fast harmonic balance methods for unsteady aerodynamic predictions of helicopter rotors. *Journal of Computational Physics* **227.12** (June 2008), 6206–6225. DOI: 10.1016/j.jcp.2008.02.028.
- [16] B. Engquist and A. Majda. Absorbing Boundary Conditions for the Numerical Simulation of Waves. *Mathematics of Computation* **31.139** (July 1977), 629–651. DOI: 10.1090/S0025-5718-1977-0436612-4.
- [17] E. Envia. “Cascade-Gust Interaction”. *Fourth Computational Aeroacoustics (CAA) Workshop on Benchmark Problems*. Ed. by M. D. Dahl. NASA/CP-2004-212954. Sept. 2004, pp. 59–66.
- [18] E. Envia, A. G. Wilson, and D. L. Huff. Fan Noise: A Challenge to CAA. *International Journal of Computational Fluid Dynamics* **18.6** (Aug. 2004), 471–480. DOI: 10.1080/10618560410001673489.
- [19] A. G. Escribano, A. Serrano, and C. Vasco. “Cascade-Gust-Interaction Problem Analysis Based on Linear CFD Analysis”. *Fourth Computational Aeroacoustics (CAA) Workshop on Benchmark Problems*. Ed. by M. D. Dahl. NASA/CP-2004-212954. Sept. 2004, pp. 81–88.
- [20] European Commission. *Flightpath 2050, Europe’s Vision for Aviation*. European Union, 2011. ISBN: 978-92-79-19724-6. DOI: 10.2777/50266.
- [21] F. Farassat. *Derivation of Formulations 1 and 1A of Farassat*. Technical Report NASA/TM-2007-214853. Hampton, VA: NASA, Mar. 2007.
- [22] F. Farassat. *Introduction to Generalized Functions With Applications in Aerodynamics and Aeroacoustics*. Technical Paper NASA-TP-3428. Corrected Copy. Hampton, VA: NASA, Apr. 1996.
- [23] F. Farassat. *Open Rotor Noise Prediction at NASA Langley - Capabilities, Research and Development*. Technical Report NASA/TM-2010-216178. Hampton, VA: NASA, Jan. 2010.
- [24] J. E. Ffowcs Williams and D. L. Hawkings. Sound Generation by Turbulence and Surfaces in Arbitrary Motion. *Philosophical Transactions of the Royal Society of London. Series A, Mathematics and Physical Sciences* **264.1151** (May 1969), 321–342. DOI: 10.1098/rsta.1969.0031.
- [25] G. B. Folland. *Fourier Analysis and Its Applications*. Vol. 4. American Mathematical Society, 1992. ISBN: 978-0-8218-4790-9.
- [26] P. di Francescantonio. A New Boundary Integral Formulation for the Prediction of Sound Radiation. *Journal of Sound and Vibration* **202.4** (May 1997), 491–509. DOI: 10.1006/jsvi.1996.0843.
- [27] C. Frey, G. Ashcroft, and H.-P. Kersken. “Simulations of Unsteady Blade Row Interactions Using Linear and Non-Linear Frequency Domain Methods”. ASME Turbo Expo 2015: Turbine Technical Conference and Exposition (Montréal, Canada, June 15–19, 2015). GT2015-43453. DOI: 10.1115/GT2015-43453.
- [28] C. Frey and H.-P. Kersken. “On the Regularisation of Non-Reflecting Boundary Conditions near Acoustic Resonance”. VII European Congress on Computational

- Methods in Applied Sciences and Engineering (Crete Island, Greece, June 5–10, 2016).
- [29] C. Frey et al. “A Harmonic Balance Technique for Multistage Turbomachinery Applications”. ASME Turbo Expo 2014: Turbine Technical Conference and Exposition (Düsseldorf, Germany, June 16–20, 2014). GT2014-25230. DOI: 10.1115/GT2014-25230.
  - [30] C. Frey et al. Advanced Numerical Methods for the Prediction of Tonal Noise in Turbomachinery — Part II: Time-Linearized Methods. *Journal of Turbomachinery* **136.2** (Feb. 2014), 021003-1-021003-10. DOI: 10.1115/1.4024649.
  - [31] N. C. Gentilli. “Efficient Solution of Unsteady Nonlinear Flows Using a Multiple Zone Harmonic Balance Technique”. MA thesis. Durham, NC: Department of Mechanical Engineering and Materials Science, Duke University, Dec. 2010.
  - [32] G. A. Gerolymos, G. J. Michon, and J. Neubauer. Analysis and Application of Chorochronic Periodicity in Turbomachinery Rotor/Stator Interaction Computations. *Journal of Propulsion and Power* **18.6** (Nov. 2002), 1139–1152. DOI: 10.2514/2.6065.
  - [33] M. B. Giles. “Non-Reflecting Boundary Conditions for the Euler Equations”. *CFDL-TR-88-1*. Feb. 1988.
  - [34] M. B. Giles. Nonreflecting Boundary Conditions for Euler Equation Calculations. *AIAA Journal* **28.12** (Dec. 1990), 2050–2058. DOI: 10.2514/3.10521.
  - [35] M. B. Giles. “UNSFLO: A Numerical Method For The Calculation Of Unsteady Flow In Turbomachinery”. *GTL Report 205*. May 1991.
  - [36] T. Guédeney et al. Non-uniform time sampling for multiple-frequency harmonic balance computations. *Journal of Computational Physics* **236.1** (Mar. 2013), 317–345. DOI: <https://doi.org/10.1016/j.jcp.2012.11.010>.
  - [37] K. C. Hall and E. F. Crawley. Calculation of Unsteady Flows in Turbomachinery Using the Linearized Euler Equations. *AIAA Journal* **27.6** (June 1989), 777–787. DOI: 10.2514/3.10178.
  - [38] K. C. Hall, P. T. Jeffrey, and W. S. Clark. Computation of Unsteady Nonlinear Flows in Cascades Using a Harmonic Balance Technique. *AIAA Journal* **40.5** (May 2002), 879–886. DOI: 10.2514/2.1754.
  - [39] K. C. Hall and K. Ekici. Multistage Coupling for Unsteady Flows in Turbomachinery. *AIAA Journal* **43.3** (Mar. 2005), 624–632. DOI: 10.2514/1.8520.
  - [40] K. Hall, C. Lorence, and W. Clark. “Nonreflecting boundary conditions for linearized unsteady aerodynamic calculations”. 31<sup>st</sup> AIAA Aerospace Sciences Meeting (Reno, NV, Jan. 11–14, 1993). AIAA Paper 93-0882. DOI: 10.2514/6.1993-882.
  - [41] L. He. An Euler Solution for Unsteady Flows Around Oscillating Blades. *Journal of Turbomachinery* **112.4** (Oct. 1990), 714–722. DOI: 10.1115/1.2927714.
  - [42] C. Hirsch. *Numerical Computation of Internal and External Flows. The Fundamentals of Computational Fluid Dynamics*. 2nd ed. Vol. 1. Butterworth-Heinemann, June 2007. ISBN: 978-0-7506-6594-0. DOI: <https://doi.org/10.1016/B978-0-7506-6594-0.X5037-1>.
  - [43] R. Hixon et al. Application of a Nonlinear Computational Aeroacoustics Code to the Gust-Airfoil Problem. *AIAA Journal* **44.2** (Feb. 2006), 323–328. DOI: 10.2514/1.3478.

- [44] F. Q. Hu. On Absorbing Boundary Conditions for Linearized Euler Equations by a Perfectly Matched Layer. *Journal of Computational Physics* **129.1** (Nov. 1996), 201–219. DOI: 10.1006/jcph.1996.0244.
- [45] H. Huang and K. Ekici. An Efficient Harmonic Balance Method for Unsteady Flows in Cascades. *Aerospace Science and Technology* **29.1** (Aug. 2014), 144–154. DOI: <https://doi.org/10.1016/j.ast.2013.02.004>.
- [46] X. Huang and D. X. Wang. Time-Space Spectral Method for Rotor–Rotor/Stator–Stator Interactions. *Journal of Turbomachinery* **141.11** (Oct. 2019), 11006-1-111006-10. DOI: 10.1115/1.4044771.
- [47] H. H. Hubbard, ed. *Aeroacoustics of Flight Vehicles. Theory and Practice*. Vol. 1. Noise Sources. Acoustical Society of America, 1995. ISBN: 1-56396-404-X.
- [48] K. S. Huh. “Computational Aeroacoustics via Linearized Euler Equations in the Frequency Domain”. PhD thesis. Cambridge, MA: Department of Aeronautics and Astronautics, Massachusetts Institute of Technology, 1993.
- [49] M. Israeli and S. A. Orszag. Approximation of radiation boundary conditions. *Journal of Computational Physics* **41.1** (May 1981), 115–135. DOI: 10.1016/0021-9991(81)90082-6.
- [50] L. Junge et al. “On The Development of Harmonic Balance Methods for Multiple Fundamental Frequencies”. ASME Turbo Expo 2018: Turbomachinery Technical Conference and Exposition (Oslo, Norway, June 11–15, 2018). GT2018-75495. DOI: 10.1115/GT2018-75495.
- [51] H.-P. Kersken et al. “Nonreflecting Boundary Conditions for Aeroelastic Analysis in Time and Frequency Domain 3D RANS Solvers”. ASME Turbo Expo 2014: Turbine Technical Conference and Exposition (Düsseldorf, Germany, June 16–20, 2014). GT2014-25499. DOI: 10.1115/GT2014-25499.
- [52] V. A. Kotelnikov. “On the Carrying Capacity of the “Ether” and Wire in Telecommunications”. *Material for the first All-Union Conference on Questions of Communications (Russian)*, Izd. Red. Upr. Svyazi RKKA.
- [53] K. A. Kousen. “Eigenmode analysis of ducted flows with radially dependent axial and swirl components”. 1<sup>st</sup> AIAA/CEAS Aeroacoustics Conference (Munich, Germany, June 12–15, 1995). AIAA Paper 95-160.
- [54] K. A. Kousen. *Eigenmodes of Ducted Flows With Radially-Dependent Axial and Swirl Velocity Components*. Technical Report NASA/CR-1999-208881. Cleveland, OH: NASA, Mar. 1999.
- [55] K. A. Kousen. “Pressure modes in ducted flows with swirl”. 2<sup>nd</sup> AIAA/CEAS Aeroacoustics Conference (State College, PA, May 6–8, 1996). AIAA Paper 96-1679. DOI: 10.2514/6.1996-1679.
- [56] K. S. Kundert, G. B. Sorkin, and A. Sangiovanni-Vincentelli. Applying Harmonic Balance to Almost Periodic Circuits. *IEEE Transactions on Microwave Theory and Techniques* **36.2** (Feb. 1988), 366–378. DOI: 10.1109/22.3525.
- [57] K. S. Kundert, J. K. White, and A. Sangiovanni-Vincentelli. *Steady-State Methods for Simulating Analog and Microwave Circuits*. Vol. 94. The Kluwer international series in engineering and computer science. 101 Philip Drive, Assinippi Park, Norwell, MA 02061 USA: Kluwer Academic Publishers, 1990. ISBN: 978-0-7923-9069-5. DOI: 10.1007/978-1-4757-2081-5.

- [58] J. Kunisch and I. Wolff. “Determination of Sampling Points for Nearly DFT-Equivalent Almost-Periodic Fourier Transforms”. 23rd European Microwave Conference (Madrid, Spain, Sept. 6–19, 1993). DOI: 10.1109/EUMA.1993.336680.
- [59] A. LaBryer and P. J. Attar. High Dimensional Harmonic Balance Dealiasing Techniques for a Duffing Oscillator. *Journal of Sound and Vibration* **324**:3-5 (July 2009), 1016–1038. DOI: 10.1016/j.jsv.2009.03.005.
- [60] M. J. Lighthill. On Sound Generated Aerodynamically. I. General Theory. *Proceedings of the Royal Society of London. Series A, Mathematical and Physical Sciences* **211**:1107 (Mar. 1952), 564–587. DOI: 10.1098/rspa.1952.0060.
- [61] M. J. Lighthill. On Sound Generated Aerodynamically. II. Turbulence as a Source of Sound. *Proceedings of the Royal Society of London. Series A, Mathematical and Physical Sciences* **222**:1148 (Feb. 1954), 1–32. DOI: 10.1098/rspa.1954.0049.
- [62] D. Lindblad and N. Andersson. Convergence Acceleration of the Harmonic Balance Method using a Time-Level Preconditioner. *AIAA Journal* (in press).
- [63] D. Lindblad and N. Andersson. “Convergence Acceleration of the Harmonic Balance Method using a Time-Level Preconditioner”. 2020 AIAA Aerospace Sciences Meeting (Orlando, FL, Jan. 6–10, 2020). AIAA Paper 2020-0563. DOI: 10.2514/6.2020-0563.
- [64] D. Lindblad and N. Andersson. “Validating the Harmonic Balance Method for Turbomachinery Tonal Noise Predictions”. 55th AIAA Aerospace Sciences Meeting (Grapevine, TX, Jan. 9–13, 2017). AIAA Paper 2017-1171. DOI: 10.2514/6.2017-1171.
- [65] D. Lindblad et al. “A Nonreflecting Formulation for Turbomachinery Boundaries and Blade Row Interfaces”. 2019 AIAA Aerospace Sciences Meeting (San Diego, CA, Jan. 7–11, 2019). AIAA Paper 2019-1804. DOI: 10.2514/6.2019-1804.
- [66] D. Lindblad et al. “Aeroacoustic Analysis of a Counter Rotating Open Rotor based on the Harmonic Balance Method”. 2018 AIAA Aerospace Sciences Meeting (Kissimmee, FL, Jan. 8–12, 2018). AIAA Paper 2018-1004. DOI: 10.2514/6.2018-1004.
- [67] D. Lindblad et al. “Implementation of a Quasi-Three-Dimensional Nonreflecting Blade Row Interface for Steady and Unsteady Analysis of Axial Turbomachines”. 2018 AIAA Aviation and Aeronautics Forum and Exposition (Atlanta, GA, June 25–29, 2018). AIAA Paper 2018-4187. DOI: 10.2514/6.2018-4187.
- [68] D. Lindblad et al. Minimizing Aliasing in Multiple Frequency Harmonic Balance Computations. *Journal of Scientific Computing* (submitted).
- [69] D. P. Lockard. “A Comparison of Ffowcs Williams-Hawkings Solvers for Airframe Noise Predictions”. 8th AIAA/CEAS Aeroacoustics Conference (Breckenridge, CO, June 17–19, 2002). AIAA Paper 2002-2580. DOI: 10.2514/6.2002-2580.
- [70] A. L. P. Maldonado et al. “Sound Propagation in Lined Annular Ducts with Mean Swirling Flow”. 21<sup>st</sup> AIAA/CEAS Aeroacoustics Conference (Dallas, TX, June 22–26, 2015). AIAA Paper 2015-2522. DOI: 10.2514/6.2015-2522.
- [71] M. S. McMullen. “The Application of Nonlinear Frequency Domain Methods to the Euler and Navier-Stokes Equations”. PhD thesis. Stanford, CA: Department of Aeronautics and Astronautics, Stanford University, 2003.



- [72] M. S. McMullen, A. Jameson, and J. J. Alonso. “Acceleration of Convergence to a Periodic Steady State in Turbomachinery Flows”. 39th AIAA Aerospace Sciences Meeting and Exhibit (Reno, NV, Jan. 8–11, 2001). AIAA Paper 2001-0152. DOI: 10.2514/6.2001-152.
- [73] M. S. McMullen, A. Jameson, and J. J. Alonso. Demonstration of Nonlinear Frequency Domain Methods. *AIAA Journal* **44.7** (July 2006), 1428–1435. DOI: 10.2514/1.15127.
- [74] P. Moinier and M. B. Giles. Eigenmode Analysis for Turbomachinery Applications. *Journal of Propulsion and Power* **21.6** (Nov. 2005), 973–978. DOI: 10.2514/1.11000.
- [75] P. Moinier, M. B. Giles, and J. Coupland. Three-Dimensional Nonreflecting Boundary Conditions for Swirling Flow in Turbomachinery. *Journal of Propulsion and Power* **23.5** (Sept. 2007), 981–986. DOI: 10.2514/1.22117.
- [76] G. Montero Villar, D. Lindblad, and N. Andersson. “Effect of Airfoil Parametrization on the Optimization of Counter Rotating Open Rotors”. 2019 AIAA Aerospace Sciences Meeting (San Diego, CA, Jan. 7–11, 2019). AIAA Paper 2019-0698. DOI: 10.2514/6.2019-0698.
- [77] G. Montero Villar, D. Lindblad, and N. Andersson. “Multi-Objective Optimization of an Counter Rotating Open Rotor using Evolutionary Algorithms”. 2018 AIAA Aviation and Aeronautics Forum and Exposition (Atlanta, GA, June 25–29, 2018). AIAA Paper 2018-2929. DOI: 10.2514/6.2018-2929.
- [78] A. Najafi-Yazidi, G. A. Brès, and L. Mongeau. An Acoustic Analogy Formulation for Moving Sources in Uniformly Moving Media. *Proceedings of the Royal Society A, Mathematical, Physical and Engineering Sciences* **467**.2125 (Jan. 2011), 144–165. DOI: 10.1098/rspa.2010.0172.
- [79] R. Nijboer. “Eigenvalues and eigenfunctions of ducted swirling flows”. 7<sup>th</sup> AIAA/CEAS Aeroacoustics Conference and Exhibit (Maastricht, The Netherlands, May 28–30, 2001). AIAA Paper 2001-2178. DOI: 10.2514/6.2001-2178.
- [80] S. Nimmagadda et al. “Robust uniform time sampling approach for the harmonic balance method”. 46th AIAA Fluid Dynamics Conference (Washington, D.C. June 13–17, 2016). AIAA Paper 2016-3966. DOI: 10.2514/6.2016-3966.
- [81] M. Olausson. “Turbomachinery Aeroacoustic Calculations using Nonlinear Methods”. PhD thesis. Gothenburg, Sweden: Division of Fluid Dynamics, Department of Applied Mechanics, Chalmers University of Technology, 2011. ISBN: 978-91-7385-481-8.
- [82] I. C. A. Organization. *2019 Environmental Report*. Accessed online at [www.icao.int](http://www.icao.int) (2020-06-29). International Civil Aviation Organization, 2019.
- [83] S. A. Orzag. On the Elimination of Aliasing in Finite-Difference Schemes by Filtering High-Wavenumber Components. *Journal of the Atmospheric Sciences* **28** (Apr. 1971), 1074. DOI: 10.1175/1520-0469(1971)028<1074:OTE0AI>2.0.CO;2.
- [84] H. Posson and N. Peake. The acoustic analogy in an annular duct with swirling mean flow. *Journal of Fluid Mechanics* **726** (July 2013), 439–475. DOI: 10.1017/jfm.2013.210.
- [85] S. Rienstra and A. Hirschberg. *An Introduction to Acoustics*. Eindhoven University of Technology, Nov. 28, 2019.

- [86] P. J. C. Rodrigues. An Orthogonal Almost-Periodic Fourier Transform for Use in Nonlinear Circuit Simulation. *IEEE Microwave and Guided Wave Letters* **4.3** (Mar. 1994), 74–76. DOI: 10.1109/75.275585.
- [87] C. Rumsey et al. Ducted-Fan Engine Acoustic Predictions using a Navier-Stokes Code. *Journal of Sound and Vibration* **213.4** (June 1998), 643–664. DOI: 10.1006/jsvi.1998.1519.
- [88] A. P. Saxer and M. B. Giles. Quasi-Three-Dimensional Nonreflecting Boundary Conditions for Euler Equations Calculations. *Journal of Propulsion and Power* **9.2** (Mar. 1993), 263–271. DOI: 10.2514/3.23618.
- [89] D. Schlüss, C. Frey, and G. Ashcroft. “Consistent Non-Reflecting Boundary Conditions for both Steady and Unsteady Flow Simulations in Turbomachinery Applications”.
- [90] R. Schnell. “Investigation of the Tonal Acoustic Field of a Transonic Fanstage by Time-Domain CFD-Calculations With Arbitrary Blade Counts”. ASME Turbo Expo 2004: Power for Land, Sea, and Air (Vienna, Austria, June 14–17, 2004). GT2004-54216. DOI: 10.1115/GT2004-54216.
- [91] J. R. Scott. “Benchmark Solutions for Computational Aeroacoustics (CAA) Code Validation”. ASME 2004 International Mechanical Engineering Congress and Exposition (Anaheim, CA, Nov. 13–19, 2004). IMECE2004-59865. DOI: 10.1115/IMECE2004-59865.
- [92] J. R. Scott. “Single Airfoil Gust Response Problem”. *Fourth Computational Aeroacoustics (CAA) Workshop on Benchmark Problems*. Ed. by M. D. Dahl. NASA/CP-2004-212954. Brook Park, OH, 20-22 October 2003, pp. 45–58.
- [93] C. E. Shannon. Communication in the Presence of Noise. *Proceedings of the IRE* **37** (1949), 10–21.
- [94] A. Sharma and H. Chen. Prediction of aerodynamic tonal noise from open rotors. *Journal of Sound and Vibration* **332.16** (Aug. 2013), 3832–3845. DOI: 10.1016/j.jsv.2013.02.027.
- [95] A. Sharma et al. Numerical Prediction of Exhaust Fan-Tone Noise from High-Bypass Aircraft Engines. *AIAA Journal* **47.12** (Dec. 2009), 2866–2878. DOI: 10.2514/1.42208.
- [96] F. Sicot, G. Dufour, and N. Gourdain. A Time-Domain Harmonic Balance Method for Rotor/Stator Interactions. *Journal of Turbomachinery* **134.1** (Jan. 2012), 011001-1-011001–13. DOI: 10.1115/1.4003210.
- [97] A. Stuermer and J. Yin. “Low-Speed Aerodynamics and Aeroacoustics of CROR Propulsion Systems”. 15th AIAA/CEAS Aeroacoustics Conference (Miami, FL, May 11–13, 2009). AIAA Paper 2009-3134. DOI: 10.2514/6.2009-3134.
- [98] C. K. W. Tam. *Computational Aeroacoustics. A Wave Number Approach*. Vol. 33. Cambridge Aerospace Series. Cambridge University Press, 2012. ISBN: 9780521806787.
- [99] C. K. W. Tam and L. Auriault. The wave modes in ducted swirling flows. *Journal of Fluid Mechanics* **371** (Sept. 1998), 1–20. DOI: 10.1017/S0022112098002043.
- [100] J. P. Thomas et al. Compact Implementation Strategy for a Harmonic Balance Method Within Implicit Flow Solvers. *AIAA Journal* **51.6** (June 2013), 1374–1381. DOI: 10.2514/1.J051823.

- [101] J. M. Tyler and T. G. Sofrin. “Axial Flow Compressor Noise Studies”. *SAE Technical Paper*. 620532. 1962. DOI: 10.4271/620532.
- [102] C. Weckmüller et al. “Ffowcs Williams & Hawkings Formulation for the Convective Wave Equation and Permeable Data Surface”. 16th AIAA/CEAS Aeroacoustics Conference (Stockholm, Sweden, June 7–9, 2010). AIAA Paper 2010-3710. DOI: 10.2514/6.2010-3710.
- [103] E. van der Weide, A. K. Gopinath, and A. Jameson. “Turbomachinery Applications with the Time Spectral Method”. 35th AIAA Fluid Dynamics Conference and Exhibit (Toronto, ON, June 6–9, 2005). AIAA Paper 2005-4905. DOI: 10.2514/6.2005-4905.
- [104] E. T. Whittaker. On the Functions which are Represented by the Expansion of Interpolating Theory. *Proceedings of the Royal Society of Edinburgh* **35** (1915), 181–194.
- [105] N. A. Wukie, D. Lindblad, and N. Andersson. “noisyduck: an open-source Python tool for computing eigenmode decompositions of duct flows”. 25<sup>th</sup> AIAA/CEAS Aeroacoustics Conference (Delft, The Netherlands, May 20–23, 2019). AIAA Paper 2019-2418. DOI: 10.2514/6.2019-2418.
- [106] N. A. Wukie et al. “Nonreflecting boundary conditions for the Euler equations in a discontinuous Galerkin discretization”. 2019 AIAA Aerospace Sciences Meeting (San Diego, CA, Jan. 7–11, 2019). AIAA Paper 2019-2172. DOI: 10.2514/6.2019-2172.

# A Euler Equations in Cylindrical Coordinates

In this appendix, the different forms of the linearized Euler equations used in sections 3.2 and 3.3 will be derived. The derivation starts from the three dimensional, nonlinear, Euler equations for a calorically perfect, ideal gas. When formulated in terms of the primitive flow variables, and written in cylindrical coordinates, they read as follows

$$\frac{\partial q}{\partial t} + A \frac{\partial q}{\partial x} + B \frac{\partial q}{\partial r} + \frac{1}{r} C \frac{\partial q}{\partial \theta} - \frac{1}{r} h = 0 \quad (\text{A.1})$$

Here,

$$q = \begin{bmatrix} \rho \\ v_x \\ v_r \\ v_\theta \\ p \end{bmatrix} \quad A = \begin{bmatrix} v_x & \rho & 0 & 0 & 0 \\ 0 & v_x & 0 & 0 & 1/\rho \\ 0 & 0 & v_x & 0 & 0 \\ 0 & 0 & 0 & v_x & 0 \\ 0 & \gamma p & 0 & 0 & v_x \end{bmatrix} \quad B = \begin{bmatrix} v_r & 0 & \rho & 0 & 0 \\ 0 & v_r & 0 & 0 & 0 \\ 0 & 0 & v_r & 0 & 1/\rho \\ 0 & 0 & 0 & v_r & 0 \\ 0 & 0 & \gamma p & 0 & v_r \end{bmatrix} \quad (\text{A.2})$$

$$C = \begin{bmatrix} v_\theta & 0 & 0 & \rho & 0 \\ 0 & v_\theta & 0 & 0 & 0 \\ 0 & 0 & v_\theta & 0 & 0 \\ 0 & 0 & 0 & v_\theta & 1/\rho \\ 0 & 0 & 0 & \gamma p & v_\theta \end{bmatrix} \quad h = \begin{bmatrix} -\rho v_r \\ 0 \\ v_\theta^2 \\ -v_r v_\theta \\ -\gamma p v_r \end{bmatrix}$$

It should be noted that for a calorically perfect, ideal gas,  $\gamma p = \rho c^2$ , where  $c$  is the speed of sound and  $\gamma$  the ratio of specific heats.

Equation (A.1) will be linearized with respect a temporally + circumferentially averaged mean flow defined as follows

$$\bar{q}(x, r) = \frac{1}{2\pi} \int_0^{2\pi} \left( \frac{1}{T} \int_0^T q(x, r, \theta, t) dt \right) d\theta \quad (\text{A.3})$$

Here,  $T$  corresponds to the time period of the flow. It should also be noted that the order of integration in the above equation is arbitrary since the integration limits are constants.

The first step in the linearization of Eq. (A.1) is to make the following variable substitution

$$q(x, r, \theta, t) = \bar{q}(x, r) + q'(x, r, \theta, t) \quad (\text{A.4})$$

By substituting this equation into Eq. (A.1), a new set of equations that contain products between averaged variables, between averaged variables and perturbation variables, and solely between perturbation variables, is obtained. Note that rational terms on the other hand can be avoided by multiplying the momentum equations in Eq. (A.1) by  $\rho$  before the variable substitution is performed. All terms that contain products between perturbation variables will be neglected. This simplification is valid as long as the amplitude of the perturbations is small compared to the mean flow, and yields a new set of equations that are linear in  $q'$ . If this new set of equations are averaged again, Eq. (A.1) written in terms of  $\bar{q}$  will be obtained since  $\bar{q}' = 0$ . The linear equations obtained earlier may therefore be

simplified even further by combining all terms that correspond to the left-hand side of Eq. (A.1) written in terms of  $\bar{q}$ , and then eliminate them. By also taking advantage of the fact that  $\frac{\partial \bar{q}}{\partial t} = \frac{\partial \bar{q}}{\partial \theta} = 0$ , c.f. Eq. (A.4), the following linearization of Eq. (A.1) is obtained

$$\frac{\partial q'}{\partial t} + \bar{A} \frac{\partial q'}{\partial x} + \bar{B} \frac{\partial q'}{\partial r} + \frac{1}{r} \bar{C} \frac{\partial q'}{\partial \theta} + A' \frac{\partial \bar{q}}{\partial x} + B' \frac{\partial \bar{q}}{\partial r} - \frac{1}{r} \bar{H} q' = 0 \quad (\text{A.5})$$

Here,

$$\begin{aligned} \bar{A} &= \begin{bmatrix} \bar{v}_x & \bar{\rho} & 0 & 0 & 0 \\ 0 & \bar{v}_x & 0 & 0 & 1/\bar{\rho} \\ 0 & 0 & \bar{v}_x & 0 & 0 \\ 0 & 0 & 0 & \bar{v}_x & 0 \\ 0 & \gamma \bar{p} & 0 & 0 & \bar{v}_x \end{bmatrix} & \bar{B} &= \begin{bmatrix} \bar{v}_r & 0 & \bar{\rho} & 0 & 0 \\ 0 & \bar{v}_r & 0 & 0 & 0 \\ 0 & 0 & \bar{v}_r & 0 & 1/\bar{\rho} \\ 0 & 0 & 0 & \bar{v}_r & 0 \\ 0 & 0 & \gamma \bar{p} & 0 & \bar{v}_r \end{bmatrix} \\ \bar{C} &= \begin{bmatrix} \bar{v}_\theta & 0 & 0 & \bar{\rho} & 0 \\ 0 & \bar{v}_\theta & 0 & 0 & 0 \\ 0 & 0 & \bar{v}_\theta & 0 & 0 \\ 0 & 0 & 0 & \bar{v}_\theta & 1/\bar{\rho} \\ 0 & 0 & 0 & \gamma \bar{p} & \bar{v}_\theta \end{bmatrix} & \bar{H} &= \begin{bmatrix} -\bar{v}_r & 0 & -\bar{\rho} & 0 & 0 \\ 0 & 0 & 0 & 0 & 0 \\ \bar{v}_\theta^2/\bar{\rho} & 0 & 0 & 2\bar{v}_\theta & 0 \\ -\bar{v}_\theta \bar{v}_r/\bar{\rho} & 0 & -\bar{v}_\theta & -\bar{v}_r & 0 \\ 0 & 0 & -\gamma \bar{p} & 0 & -\gamma \bar{v}_r \end{bmatrix} \\ A' &= \begin{bmatrix} v'_x & \rho' & 0 & 0 & 0 \\ 0 & v'_x + \rho' \bar{v}_x/\bar{\rho} & 0 & 0 & 0 \\ 0 & 0 & v'_x + \rho' \bar{v}_x/\bar{\rho} & 0 & 0 \\ 0 & 0 & 0 & v'_x + \rho' \bar{v}_x/\bar{\rho} & 0 \\ 0 & \gamma p' & 0 & 0 & v'_x \end{bmatrix} \\ B' &= \begin{bmatrix} v'_r & 0 & \rho' & 0 & 0 \\ 0 & v'_r + \rho' \bar{v}_r/\bar{\rho} & 0 & 0 & 0 \\ 0 & 0 & v'_r + \rho' \bar{v}_r/\bar{\rho} & 0 & 0 \\ 0 & 0 & 0 & v'_r + \rho' \bar{v}_r/\bar{\rho} & 0 \\ 0 & 0 & \gamma p' & 0 & v'_r \end{bmatrix} \end{aligned} \quad (\text{A.6})$$

Note that the only difference between Eq. (A.5) and Eq. (A.1) is that the former equation neglects all higher order terms in  $q'$ . Equation (A.5) thus represents the most general form of the linearized Euler equations that can be obtained with respect to the mean flow defined in Eq. (A.3).

Equation (A.5) can also be written as follows

$$\frac{\partial q'}{\partial t} + \bar{A} \frac{\partial q'}{\partial x} + \bar{B} \frac{\partial q'}{\partial r} + \frac{1}{r} \bar{C} \frac{\partial q'}{\partial \theta} - \bar{E} q' = 0 \quad (\text{A.7})$$

Here, the matrix  $\overline{E}$  is defined as

$$\overline{E} = \begin{bmatrix} -\frac{\partial \bar{v}_x}{\partial x} - \frac{\partial \bar{v}_r}{\partial r} - \frac{\bar{v}_r}{r} & -\frac{\partial \bar{p}}{\partial x} & -\frac{\partial \bar{p}}{\partial r} - \frac{\bar{p}}{r} & 0 & 0 \\ -\frac{\bar{v}_x}{\bar{\rho}} \frac{\partial \bar{v}_x}{\partial x} - \frac{\bar{v}_r}{\bar{\rho}} \frac{\partial \bar{v}_x}{\partial r} & -\frac{\partial \bar{v}_x}{\partial x} & -\frac{\partial \bar{v}_x}{\partial r} & 0 & 0 \\ -\frac{\bar{v}_x}{\bar{\rho}} \frac{\partial \bar{v}_r}{\partial x} - \frac{\bar{v}_r}{\bar{\rho}} \frac{\partial \bar{v}_r}{\partial r} + \frac{\bar{v}_\theta^2}{\bar{\rho} r} & -\frac{\partial \bar{v}_r}{\partial x} & -\frac{\partial \bar{v}_r}{\partial r} & \frac{2\bar{v}_\theta}{r} & 0 \\ -\frac{\bar{v}_x}{\bar{\rho}} \frac{\partial \bar{v}_\theta}{\partial x} - \frac{\bar{v}_r}{\bar{\rho}} \frac{\partial \bar{v}_\theta}{\partial r} - \frac{\bar{v}_r \bar{v}_\theta}{\bar{\rho} r} & -\frac{\partial \bar{v}_\theta}{\partial x} & -\frac{\partial \bar{v}_\theta}{\partial r} - \frac{\bar{v}_\theta}{r} & -\frac{\bar{v}_r}{r} & 0 \\ 0 & -\frac{\partial \bar{p}}{\partial x} & -\frac{\partial \bar{p}}{\partial r} - \gamma \frac{\bar{p}}{r} & 0 & -\gamma \frac{\partial \bar{v}_x}{\partial x} - \gamma \frac{\partial \bar{v}_r}{\partial r} - \gamma \frac{\bar{v}_r}{r} \end{bmatrix} \quad (\text{A.8})$$

In contrast to Eq. (A.5), Eq. (A.7) only contains perturbation variables in the vector  $q'$ , and average quantities in the matrices. This makes it possible to solve Eq. (A.7) using the technique derived in section 3.3. If this would be done, the influence of axial variations in the mean flow and area of the duct on the propagation of modes could be accounted for. Although this is of great importance in real-world applications, it has not been attempted in this work.

In this work, it is instead assumed that the mean flow and cross-section of the duct do not depend on  $x$ . This implies that all partial derivatives of mean flow quantities with respect to  $x$  in Eq. (A.8) can be eliminated. The assumption of axial uniformity also implies that  $\bar{v}_r = 0$  and that the mean flow satisfies radial equilibrium. To prove this, note that the continuity equation for the mean flow satisfies the following equation under the stated assumptions

$$\frac{\partial \bar{\rho} \bar{v}_r}{\partial r} + \frac{\bar{\rho} \bar{v}_r}{r} = 0 \quad (\text{A.9})$$

The general solution to this ordinary differential equation is  $\bar{\rho} \bar{v}_r = C/r$ , for some constant  $C$ . The value of this constant may be determined by noting that the flow should be parallel to the duct walls (no mass flow across duct walls). For a duct with constant cross section, this implies that  $\bar{\rho} \bar{v}_r = 0$  at the hub (or shroud). We thus get the result that  $C = 0$ , meaning that  $\bar{\rho} \bar{v}_r = 0, \forall r$ . Given that  $\bar{\rho} > 0$ , it follows that  $\bar{v}_r = 0, \forall r$ . This result may now be used in the energy equation for the mean flow (last equation in Eq. (A.1)) to obtain the following

$$\frac{1}{\bar{\rho}} \frac{\partial \bar{p}}{\partial r} = \frac{\bar{v}_\theta^2}{r} \quad (\text{A.10})$$

This shows that the mean flow indeed satisfies radial equilibrium under the stated assumptions. It should also be noted that, under the stated assumptions, the above equation is the only condition that the mean flow needs to satisfy. This means that the density, axial/circumferential velocity components, and the pressure can be chosen arbitrarily as long as Eq. (A.10) is satisfied [79, 99].

The final form of the governing equations that has been used to compute duct-modes in section 3.3 is obtained by incorporating the simplifications allowed under the assumption of axial uniformity into Eq. (A.7)

$$\frac{\partial q'}{\partial t} + \overline{A} \frac{\partial q'}{\partial x} + \overline{B} \frac{\partial q'}{\partial r} + \frac{1}{r} \overline{C} \frac{\partial q'}{\partial \theta} - \overline{D} q' = 0 \quad (\text{A.11})$$

Here, the matrix  $\overline{D}$  is defined as

$$\overline{D} = \begin{bmatrix} 0 & 0 & -\frac{\partial \overline{p}}{\partial r} - \frac{\overline{p}}{r} & 0 & 0 \\ 0 & 0 & -\frac{\partial \overline{v}_x}{\partial r} & 0 & 0 \\ \frac{\overline{v}_\theta^2}{\overline{\rho} r} & 0 & 0 & \frac{2\overline{v}_\theta}{r} & 0 \\ 0 & 0 & -\frac{\partial \overline{v}_\theta}{\partial r} - \frac{\overline{v}_\theta}{r} & 0 & 0 \\ 0 & 0 & -\frac{\partial \overline{p}}{\partial r} - \gamma \frac{\overline{p}}{r} & 0 & 0 \end{bmatrix} \quad (\text{A.12})$$

Note that Eq. (A.10) can be used to rewrite  $\overline{D}$  and that  $\overline{v}_r = 0$  in  $\overline{B}$  when Eq. (A.11) is solved. It should also be noted that Eq. (A.11) is equivalent to the equations used by Tam et al. [99].

## A.1 Linearized Euler Equations for Quasi-Three Dimensional Flows

As shown in section 3.3, the radial derivative needs to be discretized in order to solve Eq. (A.11) numerically. The equation used to derive the nonreflecting boundary condition in section 3.2 does on the other hand not contain any radial derivatives, and can therefore be applied independently at each radial location along the boundary. If it is assumed that radial derivatives of both the mean flow and the perturbation variables can be neglected, it follows that the right-hand side of Eq. (A.10) is small. This holds if  $r$  is large compared to the mean flow quantities. By introducing this condition, together with the assumption of no radial variations, in Eq. (A.11), the following is obtained

$$\frac{\partial q'}{\partial t} + \overline{A} \frac{\partial q'}{\partial x} + \frac{1}{r} \overline{C} \frac{\partial q'}{\partial \theta} = 0 \quad (\text{A.13})$$

This is the equation used to derive the exact, nonlocal, nonreflecting boundary condition for a single Fourier mode in section 3.2. It is important to keep in mind that the assumptions used to derive the above equation are pretty strong, and therefore will not be satisfied for most turbomachines.

## A.2 Linearized Euler Equations for Planar Waves

The linearized Euler equations may be simplified even further by assuming that the flow perturbations in Eq. (A.13) do not vary with  $\theta$

$$\frac{\partial q'}{\partial t} + \overline{A} \frac{\partial q'}{\partial x} = 0 \quad (\text{A.14})$$

This equation is valid when the flow perturbations are invariant in all directions except the axial one. Equation (A.14) does in fact describe the propagation of 5 planar waves. To see this, we introduce the diagonalization of  $\overline{A}$  into Eq. (A.14)

$$\frac{\partial q'}{\partial t} + T_{1D} \Lambda T_{1D}^{-1} \frac{\partial q'}{\partial x} = 0 \quad (\text{A.15})$$

By multiplying the above equation from the left by  $T_{1D}^{-1}$ , and then use the fact that the mean flow does not depend on  $x$ , the following is obtained

$$\frac{\partial c'}{\partial t} + \Lambda \frac{\partial c'}{\partial x} = 0 \quad (\text{A.16})$$

This equation represents a set of uncoupled scalar advection equations. The solution variables in this equation are known as the characteristic variables, and they are defined as follows

$$c' = T_{1D}^{-1} q' \quad (\text{A.17})$$

The speeds with which each of these characteristic variables propagate are further given by the eigenvalues to  $\bar{A}$ . These eigenvalues, and the corresponding left and right eigenvectors, may be written as follows

$$\begin{aligned} T_{1D} &= \begin{bmatrix} \bar{\rho} & 0 & 0 & \bar{\rho} & \bar{\rho} \\ 0 & 0 & 0 & \bar{c} & -\bar{c} \\ 0 & \bar{c} & 0 & 0 & 0 \\ 0 & 0 & \bar{c} & 0 & 0 \\ 0 & 0 & 0 & \bar{\rho}\bar{c}^2 & \bar{\rho}\bar{c}^2 \end{bmatrix} & \Lambda &= \begin{bmatrix} \bar{v}_x & 0 & 0 & 0 & 0 \\ 0 & \bar{v}_x & 0 & 0 & 0 \\ 0 & 0 & \bar{v}_x & 0 & 0 \\ 0 & 0 & 0 & \bar{v}_x + \bar{c} & 0 \\ 0 & 0 & 0 & 0 & \bar{v}_x - \bar{c} \end{bmatrix} \\ T_{1D}^{-1} &= \begin{bmatrix} \frac{1}{\bar{\rho}} & 0 & 0 & 0 & -\frac{1}{\bar{\rho}\bar{c}^2} \\ 0 & 0 & \frac{1}{\bar{c}} & 0 & 0 \\ 0 & 0 & 0 & \frac{1}{\bar{c}} & 0 \\ 0 & \frac{1}{2\bar{c}} & 0 & 0 & \frac{1}{2\bar{\rho}\bar{c}^2} \\ 0 & -\frac{1}{2\bar{c}} & 0 & 0 & \frac{1}{2\bar{\rho}\bar{c}^2} \end{bmatrix} \end{aligned} \quad (\text{A.18})$$

From the structure of the right eigenvectors, it follows that the convected waves correspond to one entropy wave, one radial vorticity wave, and one circumferential vorticity wave. The waves propagating at the speed of sound further represent acoustic waves.



## B Validation of Exact, Nonlocal, Nonreflecting Boundary Condition

During this thesis work, the nonreflecting boundary condition presented in section 3.2 was implemented several times into the G3D::Flow code. The first implementation, presented in [67], was based on the Fourier-based blade-row interface presented in Paper B [66]. The long term goal of this work was however to implement the nonreflecting boundary condition for inflow/outflow boundaries as well. After reviewing the first implementation, it became apparent that it was not easily extended to inflow/outflow boundaries. To avoid duplicate code, it was therefore decided to re-implement the nonreflecting boundary condition from scratch. The new implementation was presented in [65].

The second implementation became much more generic than the first one but did not change anything with regard to how the boundary condition was imposed. For this reason, the numerical stability issue originally encountered with the first implementation [67], was also encountered with the second implementation [65]. A simple fix for this stability issue was proposed in [65], but this fix was not deemed useful for more advanced applications. It was therefore necessary to further improve the second implementation. The result of these improvements is the implementation strategy outlined in section 3.2.3. The main differences between this implementation strategy, and the second implementation strategy, are the following

1. Linear extrapolation of the interior solution to the boundary faces, rather than phase extrapolation of the interior solution to ghost cells, is used to impose the boundary condition
2. Under-relaxation, rather than waiting  $N$  iterations, is used to update  $\hat{q}_{n,k,c}^{\text{nrbc}}$
3. All flow perturbations that correspond to unresolved frequencies/azimuthal wavenumbers are treated with a nonreflecting boundary condition based on characteristic variables, as originally proposed by Wukie, Orkwis, Lindblad, and Andersson [106]
4. In addition to the *direct approach*, the *reformulation using characteristic variables*, originally proposed by Giles [34], has been implemented

The purpose of this Appendix is to investigate how these changes affect the accuracy and numerical stability of the implementation. To accomplish this, two test cases have been used.

### B.1 Two-Dimensional Wave Propagation

The first test case is based simulating two-dimensional wave propagation through the domain shown in Fig. B.1. This is done by using the nonreflecting boundary condition at the inlet (leftmost boundary), at the outlet (rightmost boundary), and at the blade row interface (in the middle of the domain), and then impose one of the waves defined in section 3.2.1 at either the inlet or the outlet. After this, the wave is allowed to propagate

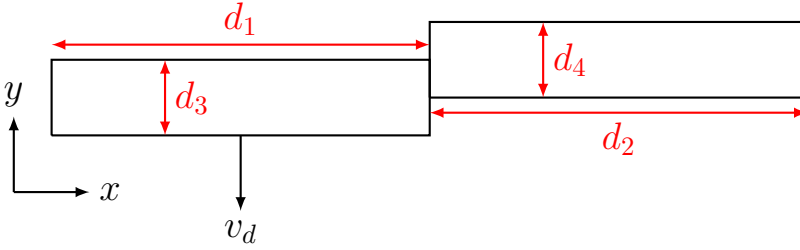


Figure B.1: *Schematic view of the computational domain used for the two dimensional wave propagation case ( $d_1 = d_2 = 5\text{m}$ ,  $d_3 = d_4 = 1\text{m}$ ).*

through the domain, cross the blade row interface, and finally impinge on the opposite boundary. Once the simulation has converged, the correctness of the implementation can be verified by comparing the numerical solution to the analytical solution given by Eq. (3.35).

At the inlet to the domain, the time+area averaged primitive flow variables were adjusted to meet a given total pressure, total temperature, and flow direction. At the outlet, the time+area averaged primitive flow variables were on the other hand adjusted to meet a given static pressure. More details on how the mean flow is imposed are provided in [65]. A periodic condition was finally imposed on the top/bottom boundaries in Fig. B.1.

A summary of all the waves that have been considered for the first test case is presented in Table B.1. Note that all values in this table are defined with respect to the absolute frame of reference. It should also be noted that if no value of  $v_d$  is specified in Table B.1, the simulation does not include the left (translating) subdomain in Fig. B.1. In these cases, the inlet is instead defined to be the left boundary of the right subdomain.

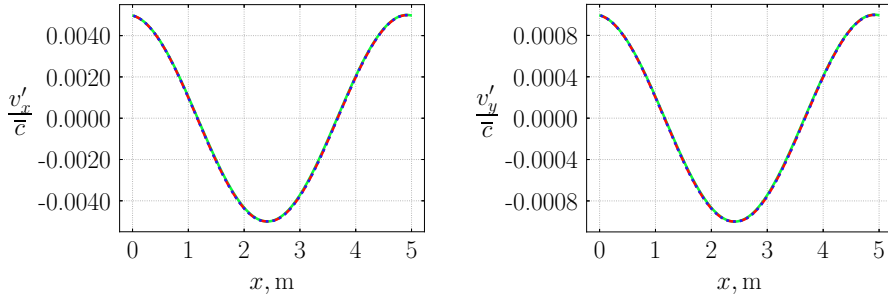
The simulations were performed by solving the Euler equations for a perfect, ideal gas, using the G3D::Flow code. In particular, the third-order accurate upwind scheme TOU-LD was used to estimate convective fluxes on cell faces, see section 2.3 for details. For all unsteady simulations, the time-domain Harmonic Balance method described in chapter 2 was used to discretize the time derivative.

The computational mesh was designed to give 30 points per wavelength for the wave in Table B.1 that has the highest axial wavenumber. For each wave, both the implementation of the *direct approach* and the *reformulation using characteristic variables* were tested, using an under relaxation factor of  $\sigma = 0.05$  to update  $\hat{q}_{n,k,c}^{\text{nrbc}}$ . The amplitude of each wave was set to ensure that the nonlinear Euler equations effectively behaved as linear. Once a simulation had converged, the solution was extracted on an axial line between the inlet and the outlet, and plotted against the corresponding analytical solution.

Results obtained for the steady vorticity wave are presented in Fig. B.2. From this figure, it can be seen that the agreement between the numerical solutions and the analytical solution is excellent for this case. This is expected, since the nonreflecting boundary condition is exact for two dimensional, linear wave propagation, and because numerical dissipation and dispersion errors will be small due to the low wavenumber of the wave.

Table B.1: Simulation settings used for the two dimensional wave propagation case.

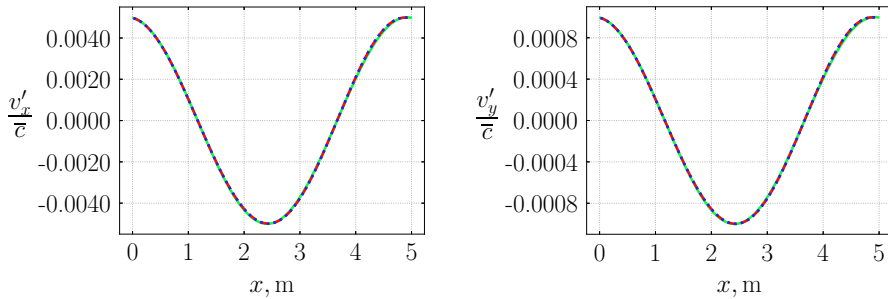
	$T_{0,\text{in}}$ K	$P_{0,\text{in}}$ Pa	$\mathbf{a}$	$p_{\text{out}}$ Pa	$\omega$ rad s <sup>-1</sup>	$k_y$ rad m <sup>-1</sup>	$k_{x,j}$ rad m <sup>-1</sup>	$v_d$ m s <sup>-1</sup>
Steady								
Vorticity Wave	104.73	47765.58	(5, 1)	40000	0	$2\pi$	-1.2566	-
Propagating								
Vorticity Wave	106.32	50356.95	(5, -3)	40000	-502.65	$2\pi$	-1.2566	-
Downstream Propagating								
Acoustic Wave								
+ Interface	106.32	50356.95	(5, -3)	40000	-1005.31	$-2\pi$	-1.0743	-80
Upstream Propagating								
Acoustic Wave	106.32	50356.95	(5, -3)	40000	-772.83	$-2\pi$	6.3070	-



(a) Axial component of velocity perturbation normalized by speed of sound. (b) Tangential component of velocity perturbation normalized by speed of sound.

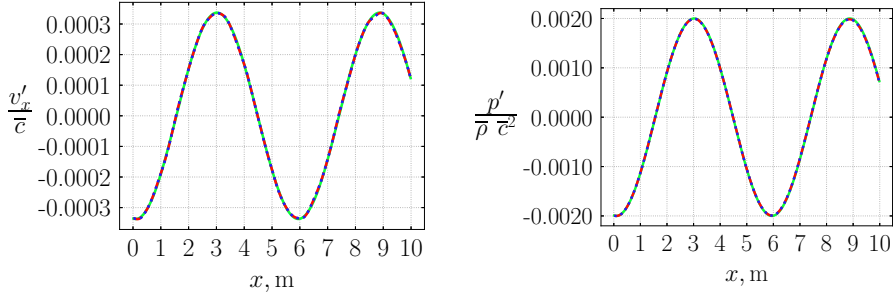
Figure B.2: Normalized velocity perturbations for the steady vorticity wave (— Analytical solution, --- Direct approach, ..... Reformulation using characteristic variables).

In Fig. B.3, the numerical solutions are compared to the analytical solution for the propagating vorticity wave. As can be seen from this figure, the agreement between the numerical solutions and the analytical solution is excellent for this case as well. Compared to the steady vorticity wave, the deviation between the numerical results and the analytical solution is however slightly larger for this case. This small difference is likely due to numerical dissipation and dispersion errors, which are larger for this case since the wavenumber of the wave no longer is perpendicular to the mean flow velocity vector.



(a) Axial component of velocity perturbation normalized by speed of sound. (b) Tangential component of velocity perturbation normalized by speed of sound.

Figure B.3: Normalized velocity perturbations for the propagating vorticity wave (— Analytical solution, --- Direct approach, ..... Reformulation using characteristic variables).

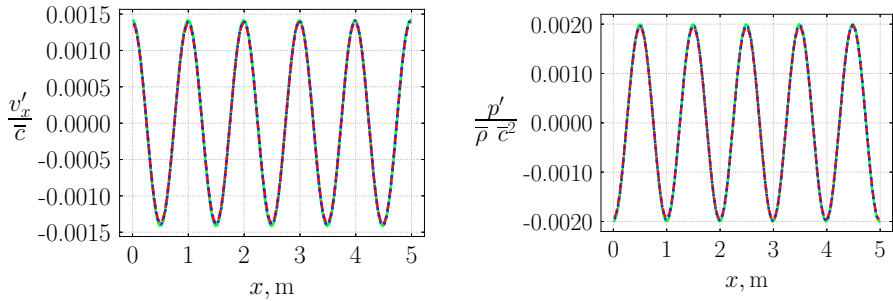


(a) Axial component of velocity perturbation normalized by speed of sound. (b) Pressure perturbation normalized by density and speed of sound.

Figure B.4: Normalized velocity and pressure perturbations for the downstream propagating acoustic wave when an interface is included at  $x = 5\text{m}$  (— Analytical solution, - - - Direct approach, ..... Reformulation using characteristic variables).

In Fig. B.4, the numerical results obtained for the downstream propagating acoustic wave are compared to the analytical solution. As can be seen from this figure, the numerical results agree very well with the analytical solution for this case as well. In particular, the blade row interface does not distort the wave in any visible way, as should be expected.

In Fig. B.5, the numerical results are finally compared to the analytical solution for the upstream propagating acoustic wave. Although the agreement in general is very good, the deviation between the numerical and analytical solution is more pronounced for this case compared to the other ones. This larger deviation is likely due to the short wavelength of this wave, which in turn gives larger dissipation and dispersion errors.



(a) Axial component of velocity perturbation normalized by speed of sound. (b) Pressure perturbation normalized by density and speed of sound.

Figure B.5: Normalized velocity and pressure perturbations for the upstream propagating acoustic wave (— Analytical solution, - - - Direct approach, ..... Reformulation using characteristic variables).

All simulations converged without problems for the first test case. In particular, there was no apparent difference in convergence rate between the *direct approach* and the *reformulation using characteristic variables*. This indicates that, if appropriate under relaxation is used, and all perturbations corresponding to unresolved Fourier coefficients are treated with a nonreflecting boundary condition based on characteristic variables, the *direct approach* can also yield a numerically stable implementation.

## B.2 Cascade-Gust Interaction Problem

The second test case is known as the "Cascade-Gust Interaction Problem", and was originally part of the Fourth Computational Aeroacoustics Workshop on Benchmark Problems hosted by NASA [17]. The purpose of this test case is to calculate the acoustic response of a linear cascade of outlet guide vanes (OGVs) that is subjected to a periodic velocity gust.

A schematic view of the computational domain used for the second test case is shown in Fig. B.6. As can be seen from this figure, the domain contains a single blade row, and extends one chord length upstream and downstream of the leading and trailing edge of the OGVs respectively.

According to the workshop description, the mean flow should satisfy the following condition at the inlet and outlet respectively [17]

$$\begin{aligned} T_{0,\text{in}} &= 288.333 \text{ K} \\ P_{0,\text{in}} &= 101325 \text{ Pa} \quad p_{\text{out}} = 0.92 P_{0,\text{in}} \\ \alpha_{\text{in}} &= 36^\circ \end{aligned} \tag{B.1}$$

In this work, these mean flow conditions are imposed on the time+area averaged primitive flow variables.

The workshop description also states that the following velocity gust, representing the wake of an upstream rotor, should be imposed at the inlet [17]

$$\mathbf{u}'_{\text{in}}(y, t) = \sum_{n=1}^3 \epsilon_n c_{0,\text{in}} \frac{\mathbf{a}}{\|\mathbf{a}\|_2} \cos(n(\omega t - k_{y,\text{g}} y)) \tag{B.2}$$

Here,  $\epsilon_n$  define the amplitude of the  $n^{\text{th}}$  frequency component,  $c_{0,\text{in}} = \sqrt{\gamma R T_{0,\text{in}}}$  is the ambient speed of sound,  $\mathbf{a}$  define the direction of the velocity perturbation,  $\omega$  is the fundamental frequency of the gust, and  $k_{y,\text{g}}$  is the azimuthal wavenumber of the gust. The amplitude of each frequency component should be selected as follows [17]

$$\epsilon_1 = 5 \cdot 10^{-3} \quad \epsilon_2 = 3 \cdot 10^{-3} \quad \epsilon_3 = 7 \cdot 10^{-4} \tag{B.3}$$

The frequency and azimuthal wavenumber should further be chosen as [17]

$$\omega = \frac{3\pi}{4} \frac{c_{0,\text{in}}}{c} \quad k_{y,\text{g}} = \frac{11\pi}{9c} \tag{B.4}$$

Here,  $c$  denotes the chord of the OGV. In this work, the direction of the velocity perturbation is finally computed as

$$\mathbf{a} = \begin{bmatrix} k_{y,g} \\ -k_{x,g} \end{bmatrix} \quad (\text{B.5})$$

Here,

$$k_{x,g} = \frac{\omega - k_{y,g} \bar{v}_{y,\text{in}}}{\bar{v}_{x,\text{in}}} \quad (\text{B.6})$$

is the axial wavenumber of the gust at the inlet.

It is important to point out that the value of  $\mathbf{a}$  obtained from Eq. (B.5) differed slightly from the value provided in the workshop description [17]. The reason for not choosing the value provided in the workshop description is that the description also states that the gust should not contain any density or pressure perturbations. According to the theory presented in section 3.2.1, this requirement can only be satisfied if the gust consists only of vorticity waves. Therefore, since the frequency and the azimuthal wavenumber is specified by the workshop description, and since the average velocity will be determined by the simulation,  $\mathbf{a}$  must be given by Eq. (B.5), that is, by the two dimensional equivalent of  $\hat{q}_3$  in Eq. (3.26).

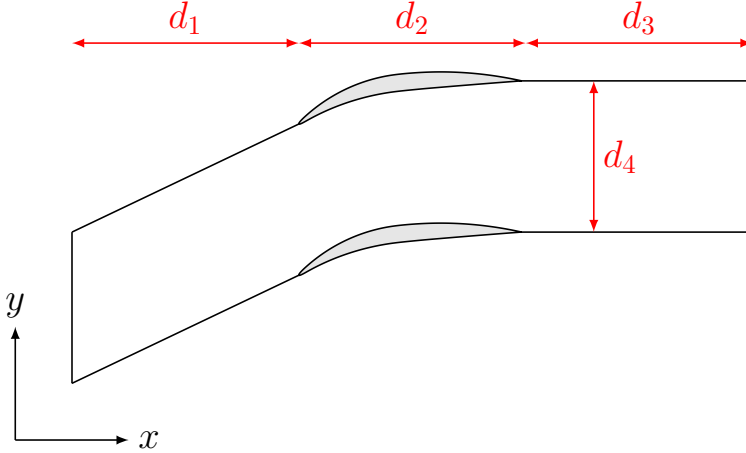


Figure B.6: *Schematic view of the computational domain used for the cascade-gust interaction problem ( $d_1 = d_2 = d_3 = c$ ,  $d_4 = 2/3c$ ).*

The flow was modeled by the Euler equations for a perfect, ideal gas for this test case as well. For spatial discretization, the third order upwind scheme denoted TOU in Table 2.1 was used. The time domain Harmonic Balance method was further used for temporal discretization. The number of harmonics used in the Harmonic Balance solver was set to  $N = 3$ . This represents the minimal number of harmonics necessary to resolve the velocity gust in Eq. (B.2), and was deemed sufficient since the amplitude of the gust is small in relation to the velocity of the mean flow.

Two simulations were performed for the second test case, one using the *direct approach*, and one using the *reformulation using characteristic variables*. In both these simulations, the nonreflecting boundary condition was employed at both the inlet and the outlet, using a under relaxation factor of  $\sigma = 0.05$  to update  $\hat{q}_{n,k,c}^{\text{nrbc}}$ . It should also be noted that the velocity gust defined in Eq. (B.2) was imposed by specifying the amplitude of  $\hat{q}_{l,p,o}$  in Eq. (3.43). The phase shifted periodic boundary condition described in section 3.1 was employed along the periodic boundaries in Fig. B.6. The OGV was further modeled as an inviscid wall, without explicitly enforcing of the Kutta condition at the trailing edge.

As shown in chapter 3, the interaction between two blade rows in relative motion generates spinning modes whose nodal diameters are given by the Tyler-Sofrin rule, Eq. (3.5). From this, it follows that the two dimensional problem considered here must consist of modes with the following azimuthal wavenumbers

$$k_y = nk_{y,g} + k \frac{2\pi}{d_4} \quad (\text{B.7})$$

Here,  $k_{y,g}$  denotes the azimuthal wavenumber of the gust and  $d_4$  is the spacing between the OGVs shown in Fig. B.6.

A multi-block mesh with a C-grid topology around the OGV was used for this test case, see Fig. B.7. This mesh was constructed to ensure that all cut-on acoustic waves were resolved with at least 30 points per wavelength in the azimuthal direction. For the particular case considered here, the highest azimuthal wavenumber for a cut-on acoustic wave turned out to be  $k_y \approx -7.33$ , corresponding to  $n = 3$  and  $k = -2$  in Eq. (B.7). The cut-on acoustic waves were in turn identified by checking the sign of  $\Lambda$  in Eq. (3.29). A similar approach to the one used here has previously been used by Coupland [9] to determine the mesh resolution. The resulting computational mesh consisted of approximately 75,000 cells.

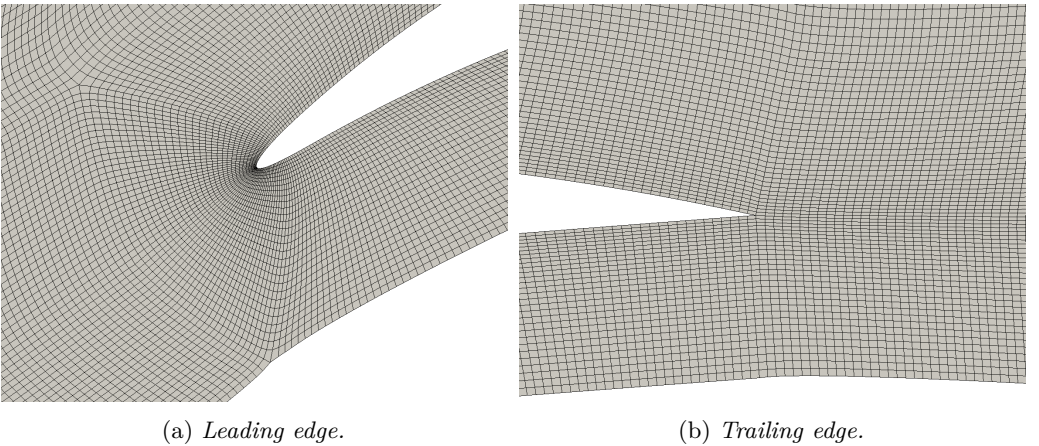


Figure B.7: Close up view of computational mesh used for the cascade-gust interaction problem.



Unfortunately, there exist no analytical solution for the cascade-gust interaction problem. Therefore, numerical results published by other authors have been used for validation instead. In particular, results from the HYDLIN code, published by Coupland [9], and results from the  $\text{Mu}^2\text{s}^2\text{T} - \text{L}$  code, published by Escribano et al. [19], were selected for validation. Both the HYDLIN and the  $\text{Mu}^2\text{s}^2\text{T} - \text{L}$  codes are frequency-domain, linearized Euler/Navier-Stokes solvers, that feature the same nonreflecting boundary condition as used in this work. This, together with the fact that both these codes are used extensively in industry [9, 19], makes them excellent candidates for validation.

In Fig. B.8a, the sound pressure level along the OGV surface computed with the *direct approach* and the *reformulation using characteristic variables* are compared to each other. From this figure, it can be seen that the two implementation approaches give identical results, as should be expected. In Fig. B.8b, the results obtained with the *direct approach* are further compared to results obtained by Coupland [9] with the HYDLIN code, and by Escribano et al. [19] with the  $\text{Mu}^2\text{s}^2\text{T} - \text{L}$  code. As can be seen from this figure, the agreement between all codes is good. In particular, none of the codes appears to stand out from the rest.

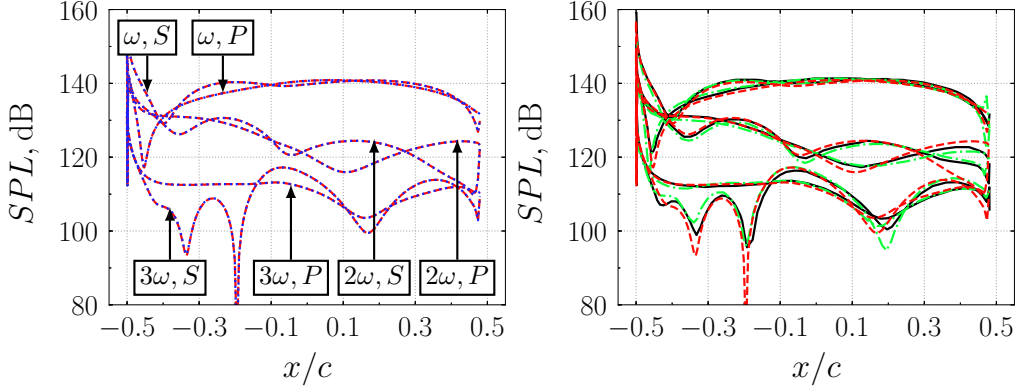
In Fig. B.9, the amplitude of some selected pressure modes that propagate at the fundamental frequency ( $\omega$ ) along the inlet and outlet ducts are shown. The first thing that can be noted from this figure is that all modes are cut-off, and therefore decay exponentially away from the OGVs. It can also be noted that all codes predict the same decay rate (slope), and give approximately the same absolute values.

In Fig. B.10, the amplitude of some selected pressure modes that propagate at twice the fundamental frequency ( $2\omega$ ) along the inlet and outlet ducts are shown. To begin with, it can be noted that one of these modes are cut-on, and therefore propagates without attenuation between the OGVs and the inlet/outlet. The small variations in amplitude seen close to the leading edge of the OGV can further be explained by the fact that the mean flow, on top of which the mode propagate, is non-uniform here. The agreement between all codes can be seen to be very good for the cut-on mode. In particular, there are no visible signs of reflections against either the inlet or the outlet. Results from both G3D::Flow and HYDLIN does however show sign of reflections for the cut-off mode (results from  $\text{Mu}^2\text{s}^2\text{T} - \text{L}$  are not available for this mode). For the G3D::Flow code, the cause of the reflection is thought to be poor convergence. This hypothesis is in turn based on experience with simpler test cases, which often required a large number of iterations to converge when a cut-off mode impinged on a boundary. The reason why the solver shows poor convergence for cut-off modes is however not known.

Finally, in Fig. B.11, the amplitude of some selected pressure modes that propagate at three times the fundamental frequency ( $3\omega$ ) along the inlet and outlet ducts are shown. These results very much resemble the results shown in Figs. B.9 and B.10, in the sense that cut-on modes do not reflect against the inlet/outlet, whereas cut-off modes do to some extent.

In summary, the results obtained with the G3D::Flow code on the second test case, both using the *direct approach*, and the *reformulation based on characteristic variables*, agree well with results published by other authors [9, 19]. In particular, none of the codes appear to produce results which stand out from the rest. Also, in cases when reflections were present in the G3D::Flow results, they were also present in results obtained with

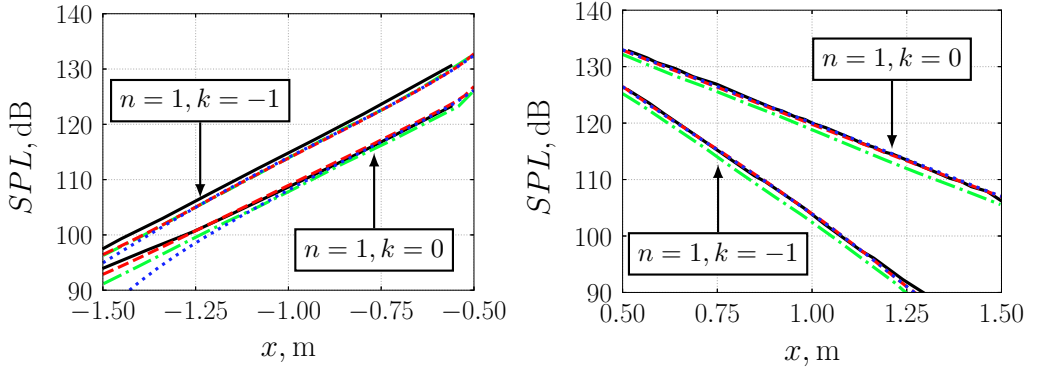
the other codes. This suggests that the cause of the reflection is not an implementation error, or a mathematical error in the formulation of the boundary condition, but rather a convergence issue. Indeed, the amplitude of a cut-off mode decays exponentially, and thereby reaches very small amplitudes close to the inlet/outlet. As a result of this, a small variation in the solution close to the boundary during the iteration process could lead to a relatively large change in the measured amplitude of a cut-off mode, which in turn could prevent the solver from converging to the correct solution.



(a) Comparison between implementations.

(b) Comparison between codes.

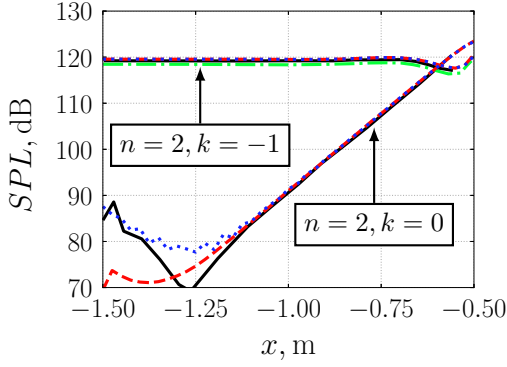
Figure B.8: Sound Pressure Level (SPL) at OGV surface, expressed in dB for each individual frequency (— HYDLIN [9], - - -  $Mu^2s^2T - L$  [19], - - -  $G3D::Flow$  (direct approach), .....  $G3D::Flow$  (reformulation using characteristic variables)).



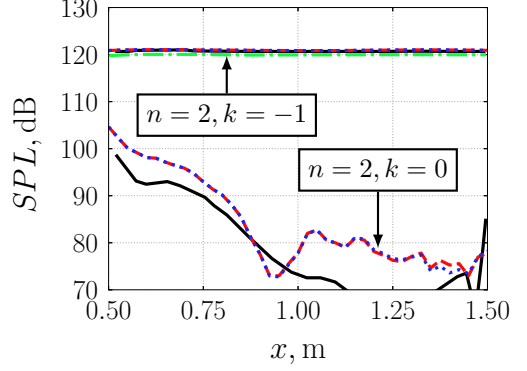
(a) Upstream.

(b) Downstream.

Figure B.9: Variation in amplitude of pressure modes spinning at the fundamental frequency (— HYDLIN [9], - - -  $Mu^2s^2T - L$  [19], - - -  $G3D::Flow$  (direct approach), .....  $G3D::Flow$  (reformulation using characteristic variables)).

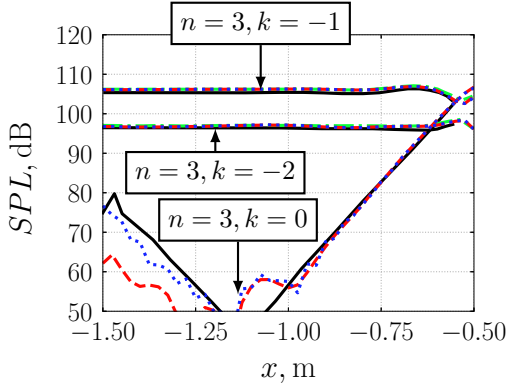


(a) Upstream.

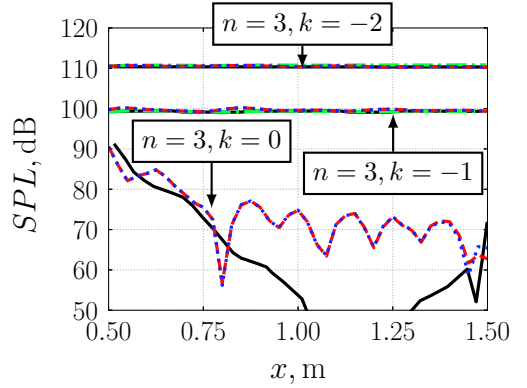


(b) Downstream.

Figure B.10: Variation in amplitude of pressure modes spinning at twice the fundamental frequency (— HYDLIN [9], -.-.-  $Mu^2 s^2 T - L$  [19], --- G3D::Flow (direct approach), ..... G3D::Flow (reformulation using characteristic variables)).



(a) Upstream.



(b) Downstream.

Figure B.11: Variation in amplitude of pressure modes spinning at three times the fundamental frequency (— HYDLIN [9], -.-.-  $Mu^2 s^2 T - L$  [19], --- G3D::Flow (direct approach), ..... G3D::Flow (reformulation using characteristic variables)).

## C Validation of `noisyduck`

In [105], `noisyduck` was validated for two test cases. In the first case, the mean flow was assumed to be radially uniform and have no swirl. This case is relevant since it has an analytical solution. In the second case, the mean flow was assumed to have a free vortex swirl and constant entropy. For this case, no analytical solution exists. Therefore, the results obtained with `noisyduck` were compared to results published by Nijboer [79].

Unfortunately, it was later discovered that the mean flow used for the second test case did not satisfy constant entropy due to a small error in the specified mean pressure. A new test case with a corrected mean pressure was therefore set up. The purpose of this appendix is to derive the correct equations that govern the mean flow for this case. In addition to this, the equations governing the mean flow for a free vortex swirl with constant density will be provided. Results obtained for these two cases will then be compared to results published in the literature. For completeness, the same results published in [105] for the uniform, axial flow, will also be provided.

### C.1 Uniform Axial Flow

In this section, the numerical results obtained with `noisyduck` will be compared to the analytical solution for a case with uniform, axial mean flow. To begin with, the analytical solution will be derived.

#### C.1.1 Analytical Solution

For a uniform axial flow without swirl, the linearized Euler equations (Eq. (3.63)) reduce to the following form

$$\begin{aligned}
 \left( \frac{\partial}{\partial t} + \bar{v}_x \frac{\partial}{\partial x} \right) \rho' + \bar{\rho} \left( \frac{\partial v'_x}{\partial x} + \frac{1}{r} \frac{\partial(rv'_r)}{\partial r} + \frac{1}{r} \frac{\partial v'_\theta}{\partial \theta} \right) &= 0 \\
 \left( \frac{\partial}{\partial t} + \bar{v}_x \frac{\partial}{\partial x} \right) v'_x + \frac{1}{\bar{\rho}} \frac{\partial p'}{\partial x} &= 0 \\
 \left( \frac{\partial}{\partial t} + \bar{v}_x \frac{\partial}{\partial x} \right) v'_r + \frac{1}{\bar{\rho}} \frac{\partial p'}{\partial r} &= 0 \\
 \left( \frac{\partial}{\partial t} + \bar{v}_x \frac{\partial}{\partial x} \right) v'_\theta + \frac{1}{\bar{\rho}r} \frac{\partial p'}{\partial \theta} &= 0 \\
 \left( \frac{\partial}{\partial t} + \bar{v}_x \frac{\partial}{\partial x} \right) p' + \gamma \bar{p} \left( \frac{\partial v'_x}{\partial x} + \frac{1}{r} \frac{\partial(rv'_r)}{\partial r} + \frac{1}{r} \frac{\partial v'_\theta}{\partial \theta} \right) &= 0
 \end{aligned} \tag{C.1}$$

By taking the material derivative of the pressure equation, and then rewrite all terms containing velocity fluctuations using the momentum equations above, we obtain a convected wave equation for the pressure fluctuation

$$\left( \frac{\partial}{\partial t} + \bar{v}_x \frac{\partial}{\partial x} \right)^2 p' - \bar{c}^2 \nabla^2 p' = 0 \tag{C.2}$$

Here,  $\bar{c}^2 = \frac{\gamma \bar{p}}{\rho}$  is the mean speed of sound, and

$$\nabla^2 = \left( \frac{\partial^2}{\partial x^2} + \frac{1}{r} \frac{\partial}{\partial r} + \frac{\partial^2}{\partial r^2} + \frac{1}{r^2} \frac{\partial^2}{\partial \theta^2} \right) \quad (\text{C.3})$$

is the Laplace operator in cylindrical coordinates.

We now proceed in accordance with chapter 3.3 and seek solutions to Eq. (C.2) on the following form

$$p'(x, r, \theta, t) = \hat{p}(r) e^{i(\omega t - k_x x - m \theta)} \quad (\text{C.4})$$

By substituting this ansatz into Eq. (C.2), we obtain

$$\frac{\partial^2 \hat{p}}{\partial r^2} + \frac{1}{r} \frac{\partial \hat{p}}{\partial r} + \left( \mu^2 - \frac{m^2}{r^2} \right) \hat{p} = 0 \quad (\text{C.5})$$

Here,

$$\mu^2 = \frac{(\omega - k_x \bar{v}_x)^2}{\bar{c}^2} - k_x^2 \quad (\text{C.6})$$

Equation (C.5) is known as Bessel's differential equation. The general solution to this equation reads as follows [85]

$$\hat{p}(r) = a J_m(\mu r) + Y_m(\mu r) \quad (\text{C.7})$$

Here,  $J_m(\mu r)$  and  $Y_m(\mu r)$  are Bessel functions of the first and second kind, respectively. These functions have an oscillatory behaviour in the radial direction. From Eq. (C.7), it follows that  $\mu$  determines the number of zero crossings of these functions. For this reason,  $\mu$  is often referred to as the radial wavenumber of the wave [85]. The radial wavenumber can be determined by imposing the boundary condition  $v'_r = 0$  at the duct walls. In terms of pressure, this boundary condition is equivalent to  $\frac{\partial p'}{\partial r} = 0$ , c.f. Eq. (C.1). By imposing the latter condition on Eq. (C.7), we obtain

$$\begin{bmatrix} J'_m(\mu r_o) & Y'_m(\mu r_o) \\ J'_m(\mu r_i) & Y'_m(\mu r_i) \end{bmatrix} \begin{bmatrix} a \\ b \end{bmatrix} = \begin{bmatrix} 0 \\ 0 \end{bmatrix} \quad (\text{C.8})$$

Here,  $r_i$  and  $r_o$  denote the inner and outer radius of the duct. Equation (C.8) has non-trivial solutions if the determinant of the left hand side is zero. By imposing this condition, an equation for  $\mu$  is obtained. This equation is solved numerically in `noisyduck` to obtain a set of permissible radial wavenumbers. After this, the axial wavenumbers are obtained by solving Eq. (C.6) for  $k_x$

$$k_x = \frac{-\bar{v}_x \omega \pm \sqrt{\frac{\omega^2}{\bar{c}^2} - \left(1 - \frac{\bar{v}_x^2}{\bar{c}^2}\right) \mu^2}}{1 - \frac{\bar{v}_x^2}{\bar{c}^2}} \quad (\text{C.9})$$

### C.1.2 Validation

The validation of **noisyduck** for uniform axial flow was performed by comparing the numerically computed axial wavenumbers to those obtained from the analytical solution for the following mean flow

$$M = \frac{\bar{v}_x}{\bar{c}} = 0.3, \quad \frac{\omega r_o}{\bar{c}} = 10, \quad \sigma = \frac{r_i}{r_o} = 0.25, \quad m = 2 \quad (\text{C.10})$$

These parameters are equivalent to those used to validate **noisyduck** in [105]. It is however important to note that in [105], the analytical solution was derived in non-dimensional form. The non-dimensional form of the solution can be obtained by scaling all dimensional properties by the mean density, mean speed of sound, and the outer radius of the duct. Alternatively, we can simply choose these reference values to be unity.

The non-dimensional (axial) wavenumbers computed with **noisyduck** are compared to the analytical solution for the uniform axial flow case in Fig. C.1. As can be seen from this figure, the numerical results obtained with **noisyduck** compare very well to the analytical solution. This good agreement should be expected, given the simplicity of the test case. In order to verify that **noisyduck** can handle more challenging cases, a free vortex swirl has also been considered. This case will be described next.

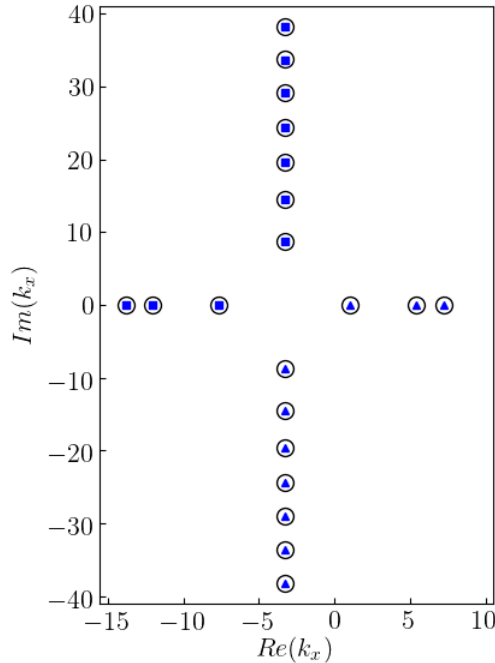


Figure C.1: Axial wavenumbers for the uniform axial flow case (■ numerical solution (upstream propagating), ▲ numerical solution (downstream propagating), ○ analytical solution).

## C.2 Free Vortex Swirl

A free vortex swirl implies that the mean circumferential velocity is described by the following function

$$\bar{v}_\theta(r) = \frac{\Gamma}{r} \quad (\text{C.11})$$

From this relation, functions describing the variation of density and pressure will be derived based on two different assumptions: constant density and constant entropy. As will be shown below, these two assumptions lead to different density and pressure distributions.

In the literature, both constant density and constant entropy flows have been used to compute duct modes for the free vortex swirl. Nijboer [79] considered both cases, Maldonado et al. [70] and Kousen [53, 55] considered a constant entropy flow, and Tam et al. [99] considered a constant density flow. Unfortunately, the choice of mean flow has also been a source of confusion. In particular, Tam et al. [99] compare their results to those of Kousen [53, 55], despite the fact that they consider different mean flows. Unfortunately, it also appears that different publications present different formulas for the mean flow, even though they claim to satisfy the same conditions. Whether this is due to a typo in the papers, or an unfortunate mistake in a calculation, is of course not known. Either way, this discrepancy poses a problem for code validation, since it becomes impossible to verify that the reference results are correct. Indeed, as noted earlier, the results presented on the free vortex swirl case in the original publication on **noisyduck** [105] turned out to be wrong. It is in light of these ambiguities that the open-source tool **noisyduck** came about. If someone is interested in comparing their results to **noisyduck**, they have access to the implementation and all test examples published in this thesis on GitHub. It is in fact recommended to compare results to the latest release of **noisyduck**, rather than results published in this thesis.

### C.2.1 Constant Density

If the mean density is constant, and the swirl distribution is given, the mean pressure can be directly obtained by integrating the radial equilibrium equation (Eq. (A.10)). For the free vortex swirl considered here, we obtain

$$\bar{p}(r_o) - \bar{p}(r) = \frac{\bar{\rho}\Gamma^2}{2} \left( \frac{1}{r^2} - \frac{1}{r_o^2} \right) \quad (\text{C.12})$$

Here,  $r$  is an arbitrary point inside the duct.

We now proceed by introducing the following non-dimensional quantities [70]

$$\bar{\rho}^* = \frac{\bar{\rho}}{\bar{\rho}_o}, \quad \bar{v}_i^* = \frac{\bar{v}_i}{\bar{c}_o}, \quad \bar{p}^* = \frac{\bar{p}}{\bar{\rho}_o \bar{c}_o^2}, \quad \Gamma^* = \frac{\Gamma}{r_o \bar{c}_o}, \quad r^* = \frac{r}{r_o} \quad (\text{C.13})$$

Here, subscript  $o$  denotes the value of the quantity at the outer duct wall. By introducing these non-dimensional quantities into Eq. (C.12), and use the relation  $\gamma \bar{p} = \bar{\rho} \bar{c}^2$ , we obtain

$$\bar{p}^* = \frac{1}{\gamma} + \frac{\bar{\rho}^* \Gamma^{*2}}{2} \left( 1 - \frac{1}{r^{*2}} \right) \quad (\text{C.14})$$



The non-dimensional free vortex swirl velocity may further be obtained as

$$\bar{v}_\theta^* = \frac{\Gamma^*}{r^*} \quad (\text{C.15})$$

It should be noted that the equations for pressure and circumferential velocity derived here are equivalent to those used by Tam et al. [99].

### C.2.2 Constant Entropy

The condition of constant entropy implies that, in addition to Eq. (3.64), the mean flow must satisfy

$$\frac{\partial \bar{p}}{\partial r} = \frac{\gamma \bar{p}}{\bar{\rho}} \frac{\partial \bar{\rho}}{\partial r} \quad (\text{C.16})$$

This relation is easily obtained from the Clausius-Gibbs equation, and represents a separable partial differential equation whose general solution is

$$\left( \frac{\bar{p}}{\bar{p}_o} \right) = \left( \frac{\bar{\rho}}{\bar{\rho}_o} \right)^\gamma \quad (\text{C.17})$$

We may now combine the above relation with the fact that  $\gamma \bar{p} = \bar{\rho} \bar{c}^2$  to obtain

$$\begin{aligned} \frac{\bar{\rho}}{\bar{\rho}_o} &= \left( \frac{\bar{c}}{\bar{c}_o} \right)^{\frac{2}{\gamma-1}} \\ \frac{\bar{p}}{\bar{p}_o} &= \left( \frac{\bar{c}}{\bar{c}_o} \right)^{\frac{2\gamma}{\gamma-1}} \end{aligned} \quad (\text{C.18})$$

The density and pressure distribution for a mean flow with constant entropy can thus be determined once the mean speed of sound is known.

In order to calculate the mean speed of sound, we start by differentiating it, and then rewrite the resulting expression using Eqs. (A.10) and (C.16)

$$\begin{aligned} \frac{\partial \bar{c}^2}{\partial r} &= \frac{\partial}{\partial r} \left( \frac{\gamma \bar{p}}{\bar{\rho}} \right) \\ &= \frac{\gamma}{\bar{\rho}} \frac{\partial \bar{p}}{\partial r} - \frac{\gamma \bar{p}}{\bar{\rho}^2} \frac{\partial \bar{\rho}}{\partial r} \\ &= \frac{\gamma - 1}{\bar{\rho}} \frac{\partial \bar{p}}{\partial r} \\ &= (\gamma - 1) \frac{\bar{v}_\theta^2}{r} \end{aligned} \quad (\text{C.19})$$

The radial variation of the mean speed of sound may now be obtained by substituting Eq. (C.11) into the above equation, and then integrate the resulting expression between  $r$  and  $r_o$

$$\bar{c}(r)^2 = \bar{c}(r_o)^2 + \frac{(\gamma - 1)\Gamma^2}{2} \left( \frac{1}{r_o^2} - \frac{1}{r^2} \right) \quad (\text{C.20})$$

By combining this expression with Eq. (C.18), we finally obtain the radial variation of the mean density and mean pressure as

$$\begin{aligned}\frac{\bar{\rho}}{\bar{\rho}_o} &= \left(1 + \frac{(\gamma-1)\Gamma^2}{2\bar{c}_o^2} \left(\frac{1}{r_o^2} - \frac{1}{r^2}\right)\right)^{\frac{1}{\gamma-1}} \\ \frac{\bar{p}}{\bar{p}_o} &= \left(1 + \frac{(\gamma-1)\Gamma^2}{2\bar{c}_o^2} \left(\frac{1}{r_o^2} - \frac{1}{r^2}\right)\right)^{\frac{\gamma}{\gamma-1}}\end{aligned}\tag{C.21}$$

These relations may also be made non-dimensional by introducing Eq. (C.13). This gives the following

$$\begin{aligned}\bar{\rho}^* &= \left(1 + \frac{(\gamma-1)\Gamma^{*2}}{2} \left(1 - \frac{1}{r^{*2}}\right)\right)^{\frac{1}{\gamma-1}} \\ \bar{p}^* &= \frac{1}{\gamma} \left(1 + \frac{(\gamma-1)\Gamma^{*2}}{2} \left(1 - \frac{1}{r^{*2}}\right)\right)^{\frac{\gamma}{\gamma-1}}\end{aligned}\tag{C.22}$$

These equations are similar, but not equivalent, to the ones presented by Maldonado et al. [70] and Kousen [54]. In both these publications, a division by  $\gamma$  is missing in the equation for the non-dimensional pressure. The above equations have been verified to satisfy radial equilibrium as well as constant entropy, both analytically and numerically. It is therefore believed that the equations presented in [70] and [54] contain a typo.

### C.2.3 Validation

The validation of **noisyduck** for the two free vortex swirl cases was performed for the following mean flow conditions

$$\gamma = 1.4, \quad \bar{v}_x^* = 0.3, \quad \bar{v}_r^* = 0, \quad \Gamma^* = 0.2, \quad \sigma = \frac{r_i}{r_o} = 0.4, \quad \frac{\omega r_o}{\bar{c}} = -10, \quad m = -2 \tag{C.23}$$

For the constant density case, the non-dimensional density was further chosen to be  $\bar{\rho}^* = 1$ .

The non-dimensional (axial) wavenumbers computed with **noisyduck** are compared to results published by Nijboer [79] and Tam et al. [99] for the constant density case in Fig. C.2a. In general, the agreement between the results shown in this figure is very good, although some differences can be seen. It is naturally impossible to determine the cause of this discrepancy. What can be said, however, is that the equations solved in **noisyduck** are equivalent to those considered by Tam et al. [99]. Tam et al. [99] does however compute the duct modes by solving an initial value problem, whereas a normal mode analysis is adopted here. A normal mode analysis is also used by Nijboer [79], but the spatial discretization of the radial derivative used in [79] differs from the method employed in **noisyduck**.

The non-dimensional wavenumbers computed with **noisyduck** are compared to results published by Nijboer [79] for the constant entropy case in Fig. C.2b. Similar to the constant density case, the agreement is good between the different results.

It should finally be noted that the sign of the axial wavenumbers computed with `noisyduck` were changed in order to stay consistent with the sign convention for the axial wavenumber used in this thesis. That is, in `noisyduck`, the axial wavenumber appears with a positive sign in the ansatz (Eq. (C.4)), whereas in this work, a negative sign is used. For this reason, results published in this thesis will be mirrored compared to those presented in [105].

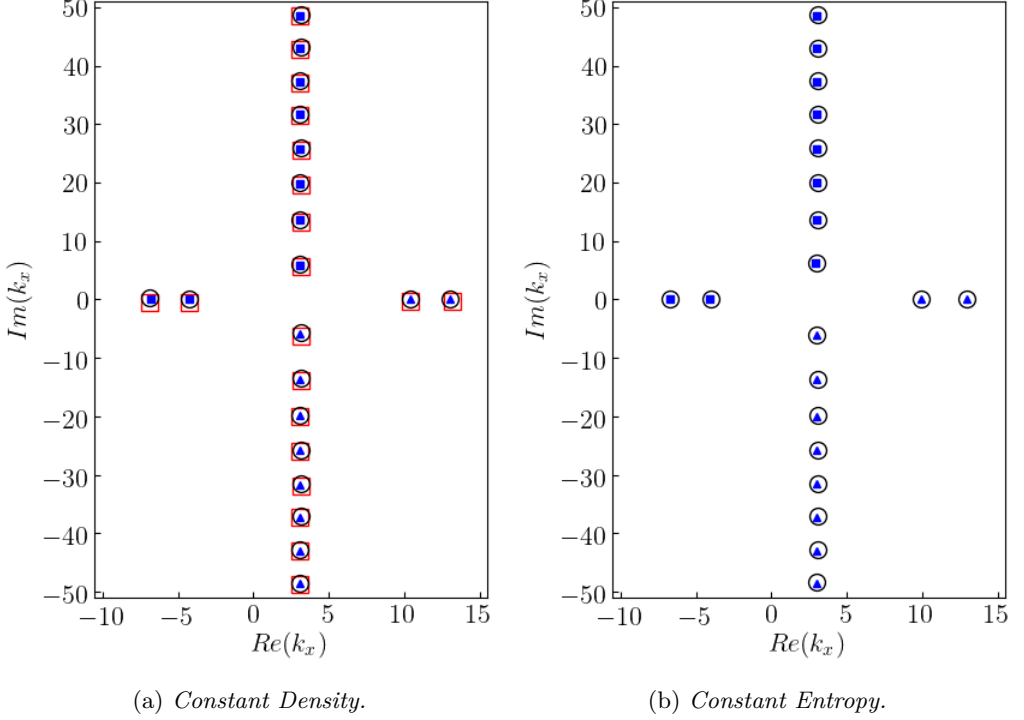


Figure C.2: Axial wavenumbers for the free vortex swirl cases ( ■ numerical solution (upstream propagating), ▲ numerical solution (downstream propagating), ○ Nijboer [79], □ Tam et al. [99]).

